Deep brain stimulation through engineered micro-coils

Tahereh (Tala) Masalehdan

Submitted in fulfilment of the requirements for the

Degree of MSc in Electronics and Electrical Engineering (Research)

James Watt School of Engineering

College of Science and Engineering

University of Glasgow

March 2024

Author's declaration

I hereby submit this thesis in fulfilment of the requirements for the degree of Master of Science in Electronics and Electrical Engineering (Research) at the James Watt School of Engineering, University of Glasgow. This document is submitted solely for the purpose of this qualification.

I certify that this thesis is my original work, except where otherwise acknowledged or referenced. All information sources and literature used are properly referenced throughout the thesis.

This research was funded by the EU BRAINSTORM Project Scholarship (GA n. 101099355).

Signature: Tahereh (Tala) Masalehdan

Date: 12.03.2024

Abstract

Neurostimulation techniques are crucial in advancing neuroscience research and addressing neurological disorders. Within this realm, magnetic neurostimulation stands out by offering numerous benefits compared to conventional methods like electrical stimulation. One of its key strengths is its enhanced orientational selectivity, which holds great potential as a noninvasive approach for deep brain neurostimulation (DBS), enabling precise targeting of specific brain circuits. The capability of magnetic neurostimulation to focus the magnetic field and penetrate deeply into the brain contributes to its effectiveness and therapeutic potential. However, attaining a high level of spatial resolution to precisely target specific sub-regions of the brain, particularly in the axial direction, poses a significant challenge. For instance, transcranial magnetic stimulation typically offers a spatial resolution in the range of ~ 0.5 – 1 line pairs per centimetre, which is unsuitable for DBS applications.

This work explored the feasibility of employing spiral micro-coils for magnetic neurostimulation, utilising both computational methods, employing the finite element method in COMSOL Multiphysics and Sim4Life software platforms, and experimental micro-coils fabrication studies. Simulations were run at a constant 100 mA current with frequencies from 1 to 3 kHz, followed by a broader sweep examining frequencies of 5 Hz to 100 kHz and currents of 1 A to 5 A in two different current input models. Furthermore, heat generation across the micro-coils for various applied frequencies and currents were modelled. In the fabrication of micro-coils, the process commenced with electroplating gold onto a polyimide substrate. Additionally, the potential of using copper as a more feasible and potentially cheaper substitute for gold in micro-coil construction was explored. The investigation of the laser parameters optimising for micro-coil fabrication involved testing three different laser power levels (2.5 W, 2.6 W, and 2.7 W) in conjunction with specific pulse settings and wavelengths.

The results revealed that the applied frequencies had a negligible effect on the coils' self-inductance, which is consistent with the predictions of the quasi-static approximation. Because the coil wire diameter was 10 times smaller than the minimum skin depth, there were no significant changes observed in magnetic flux density across different frequencies. Magnetic field strength calculations around the coils demonstrated a direct correlation between increasing current and B-field strength at all measured locations. Simulations predicted average B-field values ranging from 0.1 to 0.8 mT when using currents of 100 mA and regardless of current direction, ranged from 8.41 to 42.05 mT for currents between 1 and

5 A across all frequencies tested. However, the B-field strength above the coil surface exhibited a dependence on the direction of the current. When using the same current direction, the B-field ranged from 0.31 mT to 1.56 mT, conversely, applying the current in the opposite direction resulted in a stronger B-field ranging from 2.04 mT to 10.18 mT for currents of 1 A and 5 A. The simulations conducted in this study suggest that this magnetic neurostimulation approach has the potential to reach depths of up to 2 cm within brain tissue. Furthermore, it has been shown that regardless of the specific measurement location on the coil surface, temperature increased proportionately with increasing current, ranging from 30.42 °C to 165.38 °C for currents ranging from 1 A to 5 A across all tested frequencies.

Analysis of the electroplated gold layer revealed inconsistencies in thickness across the polyimide substrate. This variation in thickness hindered precise laser cutting during the micro-coil fabrication process. The analysis revealed that the lowest power setting (2.5 W) resulted in incomplete copper removal, verified through surface roughness measurements and visual inspection using optical and scanning electron microscopy (SEM) analyses. Higher laser power settings (2.6 W and 2.7 W) successfully achieved complete copper removal, creating clean separation between the coils. However, the highest power setting also caused minor burning of the wires. Results of electrical characteristics measurements revealed that impedance increased with frequency (in the range of 0 to 550 kHz) for all power levels. Inductance measurements showed minimal variation, remaining relatively constant at approximately 5 μH. The phase angles exhibited an increase with frequency for all coils and reached to 81.12° at 550 kHz, confirming their inductive behaviour. Power level influenced the overall resistance values, but the variations were minor. For instance, at 550 kHz, the difference in resistance between coils fabricated at 2.7 W and 2.5 W was only 1.18 Ω. The results indicate that the magnetic field (B-field) exhibited variability, ranging from 429.26 nT at the coil's centre to 1678.01 nT at 25 mm from the centre.

The aim the current study was to offer improved precision and selectivity and assess the depth and spread magnetic field's attenuation. The simulation results indicated that the magnetic neurostimulation technique being proposed could generate magnetic fields, enabling penetration into the brain model up to a depth of around 2 cm for neurostimulation. In summary, the optimal laser cutting power was identified as 2.6 W and the results demonstrate that the electrical properties of these micro-coils can be influenced by the laser power used during fabrication. Notably, the impedance values were significantly higher than the resistance across all frequencies, indicating that the micro-coils primarily behave as inductors.

Dissemination

Publications

C. Ge, **T. Masalehdan**, M. S. Baghini, V. D. Toro, H. Thomson, D. Gregurec, H. Heidari, 'Microfabrication Technology for High-resolution and Nano-invasive Magnetic Neuromodulation', Advanced Science, under review.

Conferences

1- T. Masalehdan, M. S. Baghini, C. Ge, A. Tanwear, R. Parvizi, H. Heidari 'Multifunctional Spiral Micro-Coils fabricating for Nanoinvasive Deep Brain Neurostimulation', Poster presentation: JWNC conference (1st Sep. 2023), Glasgow, UK.

2- T. Masalehdan, C. Ge, M. S. Baghini, H. wang, R. Parvizi, H. Heidari 'Nanoinvasive Deep Brain Stimulation Using Engineered Micro-Coils', Poster presentation: centre for neurotechnology conference (25th Mar. 2024), Glasgow, UK

Acknowledgement

I would like to express my deepest gratitude to my supervisors, Prof. Hadi Heidari and Dr. Roghaieh Parvizi, for their invaluable guidance, support, and encouragement throughout the entire journey of this thesis. Their expertise, patience, and unwavering belief in my abilities have been instrumental in shaping this work.

This study was made possible through funding from HORIZON-EIC-2022-PATHFINDEROPEN-01 (Grant Agreement No. 101099355), EU BRAINSTORM Project Scholarship 2022 and I am immensely grateful for their support. Their funding has provided the necessary resources and opportunities to conduct this research.

I extend my heartfelt appreciation to University of Glasgow for providing the resources and facilities necessary for the completion of this research. Special thanks are due to the staff of the James Watt School of Engineering (Electronics & Electrical Engineering) and James Watt Nanofabrication Centre whose assistance and cooperation were invaluable.

My gratitude extends to my family for their unyielding support, love, and understanding throughout this endeavour. Their encouragement and belief in me have been a constant source of strength and motivation.

I am also deeply grateful to my friends and colleagues from Microelectronics Lab (meLAB; year 2023-2024; https://www.melabresearch.com/team) for their encouragement, assistance, and understanding during challenging times. Their camaraderie and support have made this journey more enjoyable and meaningful.

Thank you all for being part of this journey and for contributing to the realisation of this thesis.

Table of Contents

List of figures

Abbreviations

2D	Two-dimensional
3D	Three-dimensional
AMF	Alternating magnetic field
AC	Alternating current
DC	Direct current
DBS	Deep brain stimulation
DIE	Domain integral equation
EM	Electromagnetic
FEM	Finite-element method
FDTD	Finite-difference domain
ht	Heat Transfer in Solids interface
MIDA	Multimodal Imaging-based Detailed Anatomical model
MOSFETs	Metal–oxide–semiconductor field-effect transistors
MNPs	Magnetic nanoparticles
mef	Magnetic and Electric Field interface
PCB	printed circuit board
RFs	Radio waves
rTMS	Repetitive transcranial magnetic stimulation
tES	Transcranial electrical stimulation
TMS	Transcranial magnetic stimulation
tRNS	Transcranial random electrical noise stimulation
tDCS	Transcranial constant electrical current stimulation
tACS	Transcranial alternating currents stimulation

List of Symbols

$\boldsymbol{A}$	Magnetic vector potential
A	Vector electrical potential
A	Amper
α	Thermal expansion coefficient
B	Magnetic field
Ca^{2+}	Calcium ions
C_p	Specific heat capacity
$\boldsymbol{D}$	Density of the electric flux
$\boldsymbol{D}$	Tensor of strain rate
D	Diameter
$\boldsymbol{E_c}$	Conservative electric field
E	Electrical field
$\boldsymbol{E_m}$	Magnetically induced electric field
ε	Electric permittivity
ε_0	Free space permittivity
E_Ω	Internal energy
$\varepsilon_0 \partial E/\partial t$	Displacement current
f	Frequency
$\boldsymbol{H}$	Magnetic field
H	Henrys
H	Thickness
Hz	Hertz
J	Current flow, Current density
J_e	Externally applied current
J_0	Current source
K^+	Potassium ions

K_Ω	Total kinetic energy
L	Inductance
Na^+	Sodium ions
$\boldsymbol{n}$	Vector of external normal to the boundary $\boldsymbol{\partial\Omega}$
μ	Magnetic permeability
μ_0	Free space permeability
Ω	A domain
Ω	Ohms
P_{str}	Internal stresses
P_{ext}	External forces
π (pi)	3.14
Q_{exch}	Net heat transfer rate
$\boldsymbol{q}$	Conduction heat flux
$\boldsymbol{q_r}$	Radiation heat flux
$\boldsymbol{Q}$	Additional heat sources
σ	Cauchy stress
σ	Electrical conductivity
σ_E	Conduction current
r	Vector position of the field
r'	Source points
ρ	Charge density/distribution
ρ	Density
S	Spacing
S	Second tensor of Piola-Kirchhoff stress
T	Temperature
T	Tesla
τ	Stress tensor
$\boldsymbol{u}_{trans}$	Translational motion velocity vector

V	Scalar magnetic
ω	Angular frequency
W	width
W	Watt
X_L	Inductive reactance

1 Introduction

1.1 Aims

This work had three clear aims:

1. Conduct literature review of state-of-the-art micro-coil design, optimised parameters.
2. Implement these finding to design coils in simulation study and explore a range of frequencies and input currents. The key aim is producing a coil which can generate around 10 mT at 2cm, which not exceed heat EFFECT.
3. Fabricate the coils simulated in previous chapter and measure performance (B-field + Impendence/ resistance).

1.2 Backgrounds

Globally, neuropsychiatric disorders are increasing, and the World Health Organization reports depression as a prominent contributor to global disability, impacting individuals' ability to live fulfilling lives [1]. Mental health conditions such as bipolar disorder, alcohol abuse disorders, depression, and schizophrenia are also among the top causes of disability [2]. Developed countries face a significant economic burden due to mental health issues, estimated at 3-4% of GDP [3, 4]. For a significant portion of patients with neuropsychiatric disorders, including 30% of those with major depression, medication falls short due to intolerable side effects or ineffectiveness [5].

Without key discoveries in neuroscience, the field of brain stimulation would not be where it is today [6-8]. While the foundation for neuroscience was laid by proposing the brain as the centre of intelligence in the 4th century BC, significant progress would not occur until the late 18th century, where the electrical nature of the nervous system was demonstrated by stimulating frog muscles and nerves using electricity [6-8]. The 19th century witnessed a surge in discoveries related to the functional organisation of the brain. Notably, brain regions have been identified crucial for speech and language, shedding light on the neural basis of aphasia [6-9]. By mapping the organisation of the motor cortex in monkeys in 1889, a way opened up for the development of the 'homunculus', a visual representation of the physical layout within the brain [10]. In the same year, the 'connectionist' theory has been proposed, suggesting that intricate communication between individual neurons is the foundation of brain function and paved the way for the modern understanding of the nervous system as a network of circuits, each responsible for specific brain functions [11]. This and several other researchers have revealed a remarkable organisation in the brain. This organisation involves

multiple, independent circuits connecting distinct areas of the thalamus, nigra, substantia, pallidum, striatum, and cortex. Each circuit plays a specific role in brain function [10-13]. Alongside progress in unravelling the brain's functional circuits, researchers have made equally significant strides in realising how individual neurons operate at the cellular level, particularly regarding memory formation and communication [14, 15].

Fuelled by these and other breakthroughs in neuroscience, researchers have been able to explore and develop various brain stimulation techniques. While the field continues to evolve, electroconvulsive therapy, as a gold standard treatment for depression, has been in use for over seven decades [15]. The development of most recent brain stimulation techniques has been fuelled by three key factors: advancements in technology, gaining a more profound comprehension of the brain circuits involved in neuropsychiatric disorders and treatments, and the need for alternatives to ineffective or poorly tolerated medications [16]. To address these limitations, a diverse array of brain stimulation techniques, both established and under investigation, offer the potential to modulate and influence brain activity. A range of neurological disorders such as Parkinson’s disease, essential tremor, epilepsy, and chronic pains, have been benefiting from the clinical application of brain stimulations [17-21]. Beyond neurological conditions, brain stimulation shows promise in treating obsessive-compulsive disorder and medication-resistant, severe depression [22, 23].

In general brain neurostimulation procedures fall into several categories: invasive, minimally invasive, and noninvasive techniques. For noninvasive brain stimulation, scientists have developed a range of techniques. Two prominent approaches are transcranial electrical (tES) and magnetic stimulation (TMS). tES offers a toolbox of methods. It can deliver a constant electrical current (tDCS) to adjust brain activity levels, use random electrical noise (tRNS) to stimulate, or employ alternating currents (tACS) to target specific brain rhythms [24, 25]. While noninvasive brain stimulation like tDCS and TMS offers potential, their impact on neurons remains complex and elusive to precise measurement. Furthermore, the limitations imposed by the scattering and absorption of electric signals within the brain hinder the ability to target specific regions and reach deeper brain structures [26, 27]. Deep brain stimulation (DBS) is a surgical approach for neurological disorders. It involves implanting tiny electrodes in specific brain areas. These electrodes deliver continuous or pulsed electrical stimulation, powered by an implanted battery, to directly modulate the activity of deep brain circuits [28]. While techniques like DBS offers precision in locality, their invasive nature remains a significant hurdle, with potential risks of infection and bleeding [28]. The specific approach to brain stimulation or neuromodulation is tailored

to the individual situation, considering the clinical condition, the specific brain region needing influence, and the intended effect. Future advancements in minimally invasive and targeted neuromodulation techniques are crucial for wider clinical applications. Fig. 1-1 showcases the category of various noninvasive brain stimulation methods including magnetic neurostimulators. Through the subsequent sections principles of neurostimulation, magnetic neurostimulation approaches, and fabrication technologies for magnetic neuromodulation are reviewed and concluded with a brief comment on future directions.

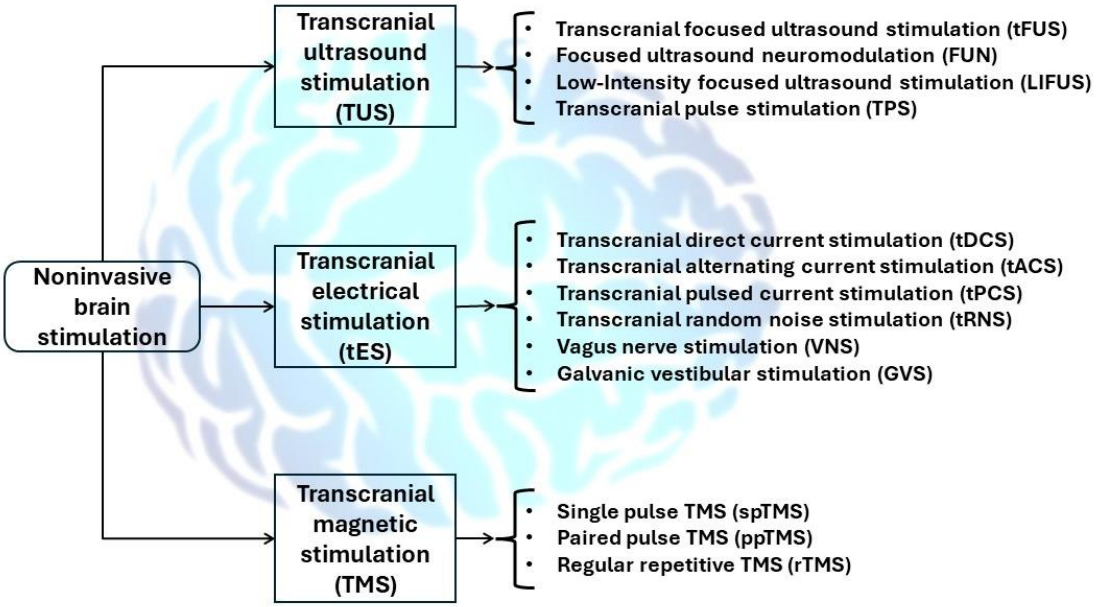

Fig. 1-1: Diagram of various noninvasive brain stimulation modes

1.3 Principles of neurostimulation

The human nervous system is characterised by its complex and highly organised cytoarchitecture, with distinct neural populations located in specific regions to ensure proper functionality [29]. Although it consists of intricate structures and communication pathways, three cell types are the building blocks of the nervous system: oligodendrocytes, astrocytes, and neurons, which originate in the central nervous system. Both glial progenitor cells and neuronal cells can give rise to all lineages of neural cells [30]. Information processing occurs through electrical changes in the conditions of neurons, leading to disturbances in their resting potential and the generation of voltage spikes, also known as action potentials [29]. These electric charges propagate through axons and are transmitted to other neurons via tree-

like structures called axon terminals [31]. When a neuron is electrically excited, it releases neurotransmitters, which are chemical signals conveyed to the dendrites of other neurons in their functional connections, known as synapses, forming the foundation of neuronal networks [32]. Glial cells, including oligodendrocytes, astrocytes, microglia, and ependymal cells, were traditionally believed to have supportive functions for neurons. However, recent studies have proposed that these cells play dynamic roles in the propagation of neuronal signals [29, 31, 32]. For example, oligodendrocytes wrap neurons in a fatty medium called myelin, which enhances the speed of electrical conduction within axons [29]. Temporal changes in the transduction of neuronal signals resulting from demyelination can limit the creation of new neural circuitry, also known as neuronal plasticity or neuroplasticity [33].

Additionally, astrocytes and oligodendrocytes produce growth factors that are essential for different stages of neuronal development, including survival, homeostasis, maturation, and differentiation [34]. These growth factors include brain-derived and glial cell-derived neurotrophic factor, neurotrophin-3, ciliary neurotrophic factor, and fibroblast growth factor-2. Furthermore, astrocytes are crucial in the function and formation of synapses by regulating the reuptake of neurotransmitters across the synapse [34].

Communication among different cells in the human body occurs through a complex interplay of chemical, mechanical, and electrical signals [35]. Chemical signals include proteins, lipids, and gases that are secreted by cells and can exert their effects locally or at distant locations within the body. Mechanical signals, on the other hand, refer to alterations in forces acting on the cell membrane [36-38]. These mechanical signals can influence cellular behaviour and responses. Electrical signals, which are characterised by alterations in the balance of negatively and positively charged ions across the outside and inside of the cell, play a vital role in cell signalling by transmitting signals across the cell membrane [39, 40]. Chemical signals, by their nature, can be relatively slow as they rely on the transfer of chemical ligands through fluids like blood. However, in many instances, there is a need for rapid and immediate responses. This is where electrical signals play a crucial role. Electrical signals have the ability to propagate quickly across cell membranes, allowing for swift transmission of messages from one side of the cell to another, or occasionally to neighbouring cells. The significance of electrical signals is particularly pronounced in neural and muscle cells compared to other cell types [41].

1.3.1 Stimulus frequency, duration, and strength

Neuronal firing naturally involves a complex interplay between chemical and electrical processes. However, to artificially stimulate this process, neurostimulation techniques deliver a precisely controlled stimulus with specific strength and duration [42, 43]. In the context of electrical stimulation, the rheobase refers to the lowest continuous current needed to trigger an action potential (firing) in a neuron. Conversely, the chronaxie describes the shortest pulse duration needed to elicit a firing at twice the strength of the rheobase [44]. The objective is to determine the optimal parameters for both strength and duration in the stimulation [44]. Adding to the existing understanding of strength and duration, studies have been emphasising on the critical role of a third parameter in neurostimulation: the frequency of stimulus application [44, 45]. It has been reported that stimulations using repetitive electrical stimulus can activate neurons at sub-threshold strengths, as seen in hippocampal neurons requiring a 15-20 $V.m^{-1}$ of a single pulse for 40 s [46, 47]. However, later research found that repetitive stimulation at 1–2 Hz can activate hippocampal neurons with a much lower field strength of just 0.14 $V.m^{-1}$ [48].

1.3.2 Unveiling the cellular mechanism: the action potential

Neurons, as excitable cells, have the remarkable ability to generate and respond to electrical signals. When not actively transmitting electrical signals, neurons maintain a relatively negative charge potential inside the cell compared to the outside (approximately -70 mV), known as the membrane resting potential [49]. This negative charge potential is crucial for the transmission of electrical signals. The control of electrical signals in neurons relies on the presence of ion gradients and ion channels. The concentration of positively charged potassium ions (K^+) is much higher inside the cell compared to the extracellular fluid. On the other hand, sodium ions (Na^+) are found in much lower concentrations inside the cell compared to the outside [50]. These concentration gradients are established and maintained by electrogenic transmembrane ATPase pumps, specifically the Na^+/K^+ ATPase enzyme found in the membranes of all animal cells. It is important to note that leak channels for K^+ are constantly open, allowing for the leakage of K^+ out of the cell. This efflux of K^+ ions contributes to the negative charge inside the cytosol. Additionally, the presence of intracellular protein anions also aids in maintaining the negative charge of the cytosol, further contributing to the overall negative resting potential of neurons [50-52]. Neurons undergo a series of four consecutive steps to generate an action potential: resting state, depolarisation, repolarisation, and hyperpolarisation as shown in Fig. 1-2 [51].

In response to various stimuli, including electrical signals, chemicals, physical pressure, temperature changes, or light, specific types of ion channels within the cell membrane become activated [53]. The resting potential of neurons typically hovers around -70 mV, representing a steady-state condition. To initiate a firing, the potential of the membrane gradually increases towards the threshold potential [51]. Depolarisation beyond the threshold potential triggers the opening of voltage-gated sodium channels, leading to a surge of sodium ions entering the cell. During this phase the interior of the cell becomes increasingly positive, reaching approximately +60 mV (the Na^+ electrochemical equilibrium potential) [54].

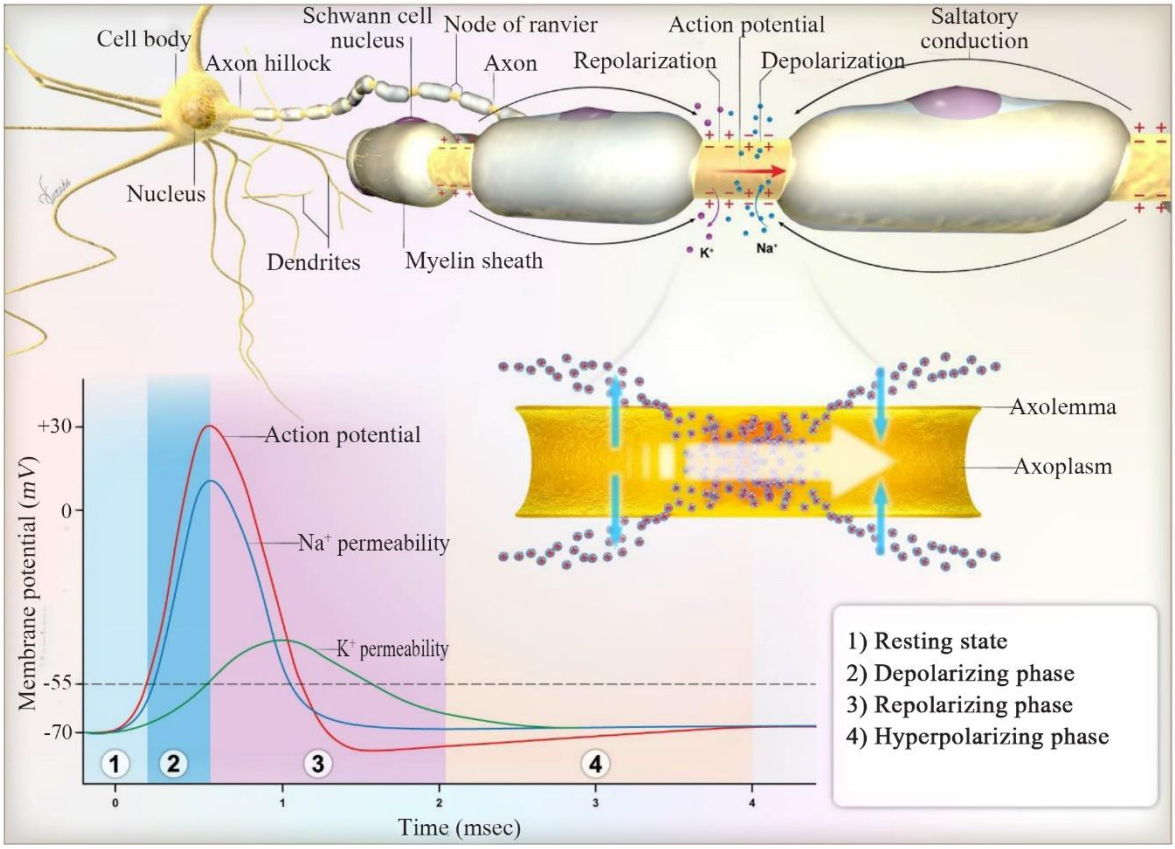

Fig. 1-2: Representation of the nerve cells electrical action potential [51]. This image was used under the Creative Commons License 4.0 permission

The depolarisation phase includes an overshoot, characterised by extreme positivity. Following the overshoot, the permeability of sodium rapidly decreases as the sodium channels close. This renders the cell unresponsive to further stimulation, entering an absolute refractory period. Repolarisation occurs when potassium channels, which are voltage-gated, open in the cell membrane upon reaching the overshoot potential [55]. This allows potassium ions to exit the cell, reducing its positivity. The primary objective of repolarisation is to bring the potential of a membrane back to its resting level. After repolarisation, the membrane of a neuron often undergoes hyperpolarisation, characterised by a more negative membrane

potential than its resting state, often falling below -70 mV [51]. Hyperpolarisation is a result of the prolonged opening of potassium channels, causing an efflux of potassium ions. Its purpose is to facilitate the recovery of the resting potential of the membrane. However, this hyperpolarised state is transient, and the membrane eventually returns to its resting potential, while just prior to this phase, sodium channels begin to reactivate [56]. A strong stimulus is required during this phase to initiate new action potentials, leading to the generation of a relative refractory period. During this period, three sodium ions and two potassium ions are pumped out of the cell by the Na^+/K^+ ATPase pumps. The cell prepares itself to respond to another triggering stimulus [57]. As a result, there is a brief increase in the action potential, albeit for a short duration. This temporary change in membrane potential is referred to as an electrical signal, serving as the means of electrical communication both within the cell membrane and between cells [51].

It has been shown that cells possess electrical properties such as conductance and resistance, which are determined by the structure of their cell membranes [58, 59]. These membranes exhibit a difference in electrical charge, with the exterior of the cell being electropositive and the interior electronegative. During periods of neural inactivity, the cell membrane maintains a resting potential. This resting potential is maintained through the distribution of K^+ and Na^+ ions across the potassium channels and neural fibre membranes, respectively [60]. However, when neural transmission occurs, rapid depolarisation and repolarisation take place, which are driven by action potentials—sudden changes in the resting potential. These ion fluxes and changes in membrane potential result in the generation of electrical activity. This electrical stimulation has a profound impact on cellular behaviour, influencing various cellular processes [60]. Furthermore, specific patterns of stimulation can induce muscle atrophy and promote muscle reinnervation, allowing for controlled cell and tissue regeneration [60]. It has been revealed that the electrical activity of neurons, including action potentials, can be modulated by external stimulus [61, 62]. This neuronal stimulation has been found to have several beneficial effects, such as activating growth processes, redistributing cytoplasmic materials, and promoting asymmetrical distribution of molecules on the cell surface [63]. Studies have demonstrated that electrical fields have a positive impact on mitochondrial function, cell adhesion, cell growth, and cell migration [60, 64]. Beyond electrical stimulation, magnetic stimulation also shows promise in promoting nerve regeneration in various areas, using diverse stimulation patterns and magnetic field settings [65].

1.3.3 Neuronal communication via different stimulations

Stimulating and recording neural activity can benefit from strengths of different stimuli, such as light, sound, and magnetic fields [66]. While optical imaging and stimulation techniques offer high temporal and spatial resolution by using tools like engineered opsins, infrared light, and indicators of voltage and calcium, their application remains limited to superficial brain structures (less than 1mm deep) due to tissue properties (i.e., scattering and absorbance) [67-70]. Despite employing a 3-photon excitation technique with a near-infrared 1,675-nm laser, researchers are still limited to only up to 1.5 mm deep to accessing brain structures [71].

Acoustic waves demonstrate a frequency-dependent ability to significantly enhance penetration depth within the brain [72]. It has been shown that a low-frequency (<0.65 MHz) and low-intensity (0.12 MPa) transcranial focused ultrasound can modulate activity in the somatosensory cortex of humans at depths of 3 cm [73]. While lower-frequency ultrasound waves can penetrate deeper into tissues without being significantly weakened, their resolution suffers. This is because resolution is linked to wavelength, and lower frequencies have longer wavelengths, resulting in larger areas of interaction (modulation volumes exceeding $1mm^3$) within the tissue [72].

Unlike other methods, magnetic fields have a unique advantage: they can penetrate deep within the body because the vast majority of tissues in a human body barely interact with magnetic fields [74, 75]. Low-frequency (below 1 kHz) and strong (over 1 T) magnetic fields can be used to painlessly influence brain activity through the skull by creating ionic currents within the brain [76]. However, the shape of the coil limits how precisely the generated fields by TMS can target brain areas. Because of this, TMS is mainly used to influence the outer layer of the brain (cortex) with an accuracy of about a centimetre [77].

Nanoscale transducers with capability to convert magnetic, acoustic, and optical stimuli into biological signals hold promise for enhanced non-invasive neural interfaces and could offer a deeper brain penetration for signals with improved temporal and spatial resolution compared to existing methods [53]. For instance, gold nanoparticles, and semiconductor quantum dots have unique abilities when exposed to light. They have the capability to convert light into heat, or voltage [78, 79]. In a steady magnetic field, magnetic nanoparticles (MNPs) can cluster in specific arrangements. Exposure to changing magnetic fields, enables them to convert the magnetic force into an electrical signal or even apply torque. Additionally, rapidly switching magnetic fields can cause them to heat up due to a

phenomenon called hysteresis [80-82]. By precisely controlling the surface characteristics, composition, and size of these MNPs, both their targeting moieties and magnetic moments can be tailored. This allows for the delivery of diverse chemical and mechanical signals to specific locations within cells with high temporal and spatial precision [83].

1.4 Magnetic neurostimulation approaches

While the idea of magnetically stimulating biological tissues, particularly the visual cortex of humans, dates back to 1896, it was not until 1910 that the first demonstration took place. This paved the way for a more groundbreaking discovery [84-86]. Inspired by electromagnetic induction principles of Faraday, researchers developed a method to stimulate neural tissue without direct contact, building upon the earlier work of mapping the canine motor cortex using direct electrical stimulation. Interestingly, this breakthrough arose during an investigation of how strong, alternating magnetic fields affected the heating of living animals [84-86]. In simpler terms, the method includes a flow of an electric current through coils to create a rapidly changing (time-varying) magnetic field. In turn it, creates an electrical field within the targeted tissue [87]. In neurostimulation applications, one of the most advantageous aspects of this induced electric field is it bypasses the need for direct physical contact with the targeted neurons. Therefore, neurostimulation devices based on magnetic fields are less susceptible to the challenges of biofouling, which can occur when biological materials accumulate on implanted devices [88, 89]. Magnetic stimulation relies on Faraday's fundamental electromagnetic induction principle [90-92]. In magnetic stimulation, the strength and direction of the changing magnetic field determine the strength and direction of the induced electrical field. This induced *E* field, which depends on both the scalar magnetic and vector electrical potentials, ultimately excites biological tissues by using a magnetic field, as described by Ampere's law [91]. This is explained in more details in section 2. When the biological tissue is stimulated, it allows an electric current to flow through. This current's density is related to the magnetic field within the tissue. The relationship between these elements depends on the tissue permeability, which is similar to that of air. Unlike some other stimulation methods, magnetic stimulation does not have a single magnetic field level as a threshold needed for neural activation. Instead, a combination of factors determines its effectiveness: the direction and strength of the magnetic field, the tissue's properties (represented by permeability), the size of the device, and the area being targeted. This interplay ultimately generates the electrical field that stimulates the neurons [90-92]. As aforementioned, there are three main categories of noninvasive brain

stimulation: electrical, ultrasound, and magnetic, which is shown in Fig. 1-1. The focus of this study is on magnetic stimulation and through the following subsections various kinds of magnetic stimulation approaches are reviewed.

1.4.1 Transcranial magnetic stimulation

TMS is a safe and painless procedure that uses a brief, high-intensity electrical current (thousands of ampers) to generate a powerful magnetic field (up to 2 T) pulsing through the brain for a very short time (100 microseconds). This noninvasive approach relies on Faraday's principle of electromagnetic induction to influence brain activity [93]. In this regard, a stimulating coil is placed on the scalp and the generated magnetic pulse from it has the capability to pass unimpeded through the bone of the skull and create an electric field within the brain [94]. The induced electrical field is strong enough to trigger nerve impulses (action potentials) and safely activate networks of the brain without causing pain. In the mid-1980s, the first TMS devices were developed and officially used in clinical settings [95, 96]. Fig. 1-3 illustrates the schematic of neuronal activation using TMS.

1.4.1.1 Mechanisms of TMS

A TMS machine consists of capacitors that store electrical energy and a coil with specific properties (resistance and inductance). When a time-varying current flows within the coil positioned near the scalp, it creates a changing, powerful magnetic field. This magnetic field can penetrate the skull and induce electrical currents (called eddy currents) within the brain tissue. These eddy currents can affect the electrical activity of nearby neurons, potentially resulting in the creation of action potentials (nerve impulses) and finally affecting mood or behaviour [96, 97]. Several factors, like the type and direction of the TMS coil, influence the geometry and strength of the generated electrical field in the brain. These changes in the electric field, in turn, affect which brain regions and nerve cells are stimulated by TMS. TMS utilises coils in various shapes, each offering specific advantages. Round coils deliver a broader and stronger magnetic field, making them powerful but less precise. In contrast, figure-of-eight coils are more focused, concentrating their strongest stimulation at the intersection of coils, ideal for targeting specific brain regions. Additionally, H-coils, with their complex design, allow for a slower decrease in magnetic field intensity as it travels deeper into the brain, making them suitable for stimulating deeper brain structures [77, 98, 99].

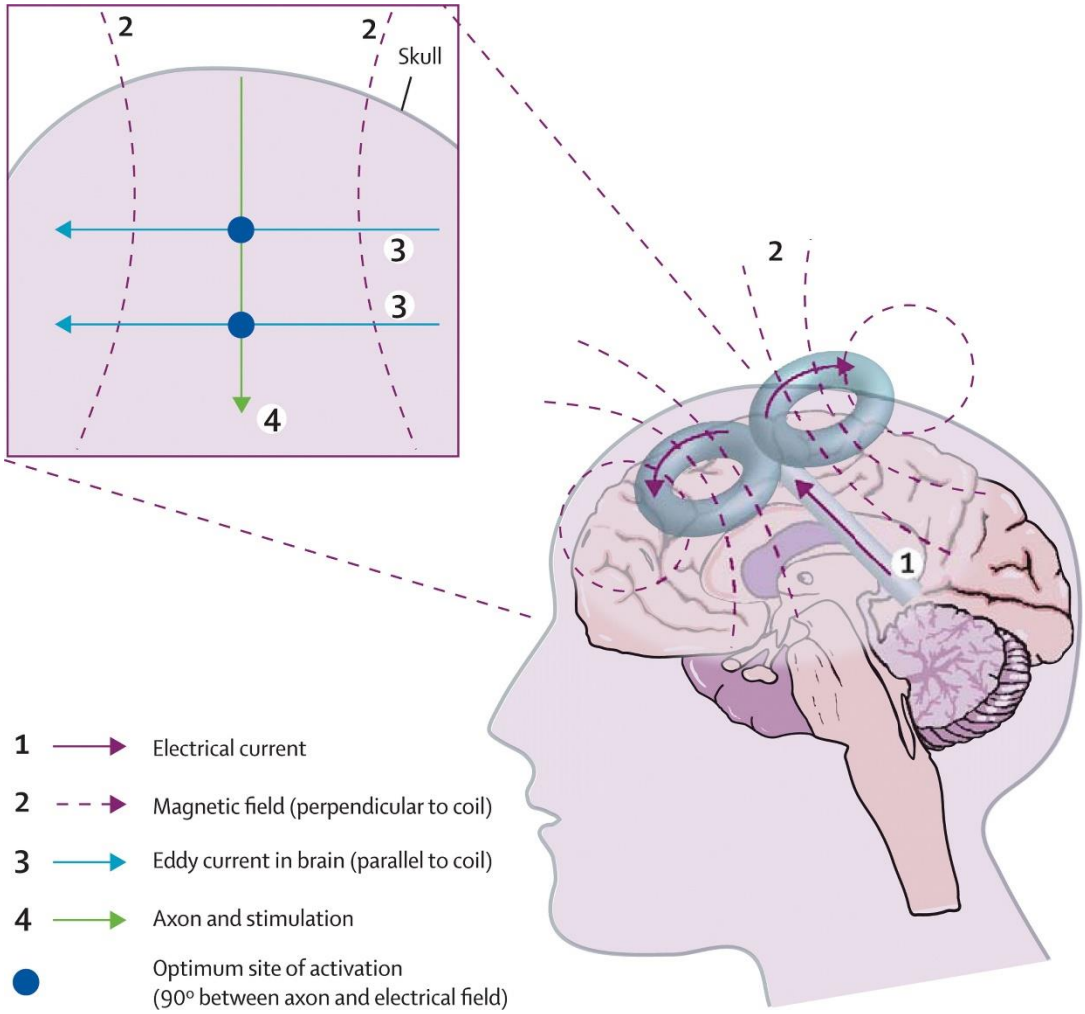

Fig. 1-3: Schematic representation of neuronal activation using transcranial magnetic stimulation. Adopted with permission from [96]. Copyright© 2008 Elsevier Ltd

Some coils incorporate an iron core within their windings. This core concentrates the magnetic field, making it stronger and allowing it to reach deeper into the brain tissue [100]. Furthermore, the stimulation strength of the pulse significantly affects how TMS works, where standard coils, like the circular and figure-of-eight ones, have a limited ability to reach deeper brain regions [101, 102].

The strength of the TMS induced electrical current weakens quickly the farther it travels from the stimulation point. However, increasing the stimulation intensity allows the induced field to reach deeper brain regions, potentially activating additional networks of nerve cells [103]. Today, a wide range of coils are available, each suited for specific purposes.

Not only do the shape and size of the coil influence which brain region is stimulated, the waveform of a pulse (either single-pulse or double-pulse) controls how the nerve cells within that region are affected [77, 98, 99, 104, 105]. When a single, short pulse of magnetic stimulation (monophasic pulse) was applied using a figure-of-eight coil positioned over the

motor cortex (i.e., a brain area controlling hand movements, specifically the hand knob), it primarily activated the corticospinal axons directly. This activation was measured by recording electrical signals traveling down the spinal cord (D-waves) [106]. However, when the same figure-of-eight coil was positioned differently in a posteroanterior orientation, it only generated a specific type of electrical signal called "I-waves." Interestingly, using an even different positioning (anteroposterior orientation) leads to even later I-waves [107-109]. The presence of I-waves indicates that the stimulation might be indirectly affecting pyramidal cells through horizontal fibres near the surface of a brain region involved in movement (i.e., precentral gyrus). This suggests that similar indirect stimulation might be possible when targeting areas outside the motor cortex, at least in the main outer layer of the brain (i.e., neocortex) [110].

1.4.1.2 Applications and developments of TMS

TMS has been used for identifying the compression of spinal cord in individuals with myelopathy. This technique measures how long it takes for electrical signals to travel from the brain to muscles in the arms and legs. Studies have shown that TMS is highly accurate in detecting this condition, with a 100% success rate in identifying patients with spinal cord compression and an 84.8% success rate in correctly identifying those without it [111].

Early versions of TMS used circular coils in diameter of around 110 mm to 130 mm with fewer windings (around 14). These coils stimulated a larger area of the brain cortex. To achieve more focused stimulation for therapeutic and brain mapping applications, researchers developed smaller double coils, like the figure-of-eight coil. These coils have a smaller individual diameter (around 75-87 mm) and more windings (around 9-10 each) [77, 98, 99]. While smaller coils offer better focus, they also heat up faster during repeated stimulation. To address this, researchers developed cooling systems using active or static liquids or even air [77, 98, 99]. Compared to single pulses, double pulses are generally believed to be more effective, especially when stimulating the motor cortex to generate electrical signals indicating muscle activity (i.e., motor evoked potentials) [112]. Double pulses are the most common type of electrical signal used for repetitive TMS (rTMS) because they require less energy compared to single pulses [113]. In double pulse stimulation, the second electrical pulse is believed to be more effective at generating electrical currents within the brain [109]. It is important to note that comparing research on double pulse stimulation can be confusing. This is because different magnetic stimulator

models from various manufacturers might deliver the two pulses in opposite directions. This does not affect the overall stimulation process, but it is crucial to be aware of when comparing results from different studies [112]. Compared to single pulses, double pulses create a more intricate pattern of nerve cell activation, affecting a broader range of cells. However, double pulses might be less effective for achieving long-lasting effects after rTMS because they do not consistently target the same group of cells. Therefore, single pulses might be a better choice for rTMS aiming for steady after-effects [114, 115]. Scientists are constantly improving TMS by developing new stimulation patterns that resemble the natural firing patterns of brain cells. As an example, stimulations based on a theta burst uses short bursts of high-frequency pulses at a specific delivery rhythm (theta frequency). This approach has been shown to be more efficient than traditional rTMS in provoking changes in cortical plasticity in a shorter period of time [116]. Studies have shown that using high frequencies to stimulate the brain can temporarily disrupt the function of the stimulated areas. This characteristic of rTMS allows it to be employed as an approach to reveal the function of different cortical areas either by inhibiting or stimulating specific areas [117, 118].

Application of rTMS in treating mental health conditions have reported to be successful, particularly in treating major depressive disorder. Numerous studies have shown that rTMS can be a valuable tool in managing this condition [119-122]. Research has shown the effectiveness of using TMS using respectively low- and high-frequency stimulations [123-126]. Fuelled by a strong foundation of research, TMS and rTMS has transitioned from the lab to the clinic, gaining approval for use in different countries. While currently used for specific conditions, ongoing research is actively investigating its potential to treat a wider range of disorders, including, post-traumatic stress, schizophrenia, obsessive-compulsive, substance abuse, and chronic pain [127-132].

1.4.1.3 Advantages and challenges of TMS

Unlike electrical stimulation, magnetic stimulation induces currents that flow mostly parallel to the coil surface within the brain. This unique feature allows TMS to target specific brain regions with various techniques and parameters, showing promise as a diagnostic and treatment tool [126, 133-135]. Despite its promise, TMS is still under investigation in some ways. The strength of the electrical current it creates can vary across the brain. Researchers are also working to understand exactly which cells of the nervous system are affected during

TMS application and how those cells respond, because the exact influences of TMS on neurons are not fully understood, including whether they are state-dependent, inhibitory, or excitatory [136]. A major drawback of TMS is its limited penetration to the brain. While it effectively targets the cortex of a brain, stimulating deeper structures (i.e., subcortical areas) is difficult. TMS pulses inevitably stimulate the cortex on the way to any subcortical target [137, 138].

Despite its well-established safety profile as a non-invasive treatment for brain stimulation, rTMS, carries a minimal risk of seizures. In very rare cases, about one in 30,000 treatments, seizures may occur during routine clinical use [139]. Another issue with using rTMS is the possibility of fainting, which can occur in rare cases during rTMS, especially in patients with low blood sugar, dehydration, or high anxiety [140]. When using stimulation within established safety parameters, the risk of side effects is generally low [141].

1.4.2 Magnetic stimulation using nanomaterials

Magnetic fields used in brain stimulation techniques like TMS act as an intermediate step. Ideally, these fields need to be converted into more specific and localised stimulations within the brain [53, 142]. Several techniques are being explored that utilise MNPs and magnetic fields for the purpose of magnetic signals conversion for various applications [53, 143-145]. MNPs can function as transducers, and be categorised in four main groups, including magnetomechanical, where the MNPs cause physical movement; magnetocatalic, where lead in generation of surface charges; magnetoelectric, where electricity is produced; and magnetothermal, where heat is generated [146].

The schematic representation of these effects is shown in Fig. 1-4. Fig. 1-4a shows the general principle involved in tissue stimulation. In general, it involves a wireless signal such as magnetic field that passes through tissue. This signal interacts with strategically placed nanomaterials within the brain. These nanomaterials convert the wireless signal into a more focused effect, like a heat, or electric field right next to a neuron. There are different ways to position these nanomaterials: (I) immobilised dispersed in the extracellular area, (II) attached directly to the outer membrane, (III) specifically linked to ion/protein channels, or (IV) even placed inside the cytoplasm [53]. Fig. 1-4b represents various responses that MNPs can have in response to different types of external stimuli. Accordingly, they can activate specific channels on brain cells such as spinning magnets (rotating field): can trigger mechanosensitive channels like Piezo1, which are sensitive to pressure changes.

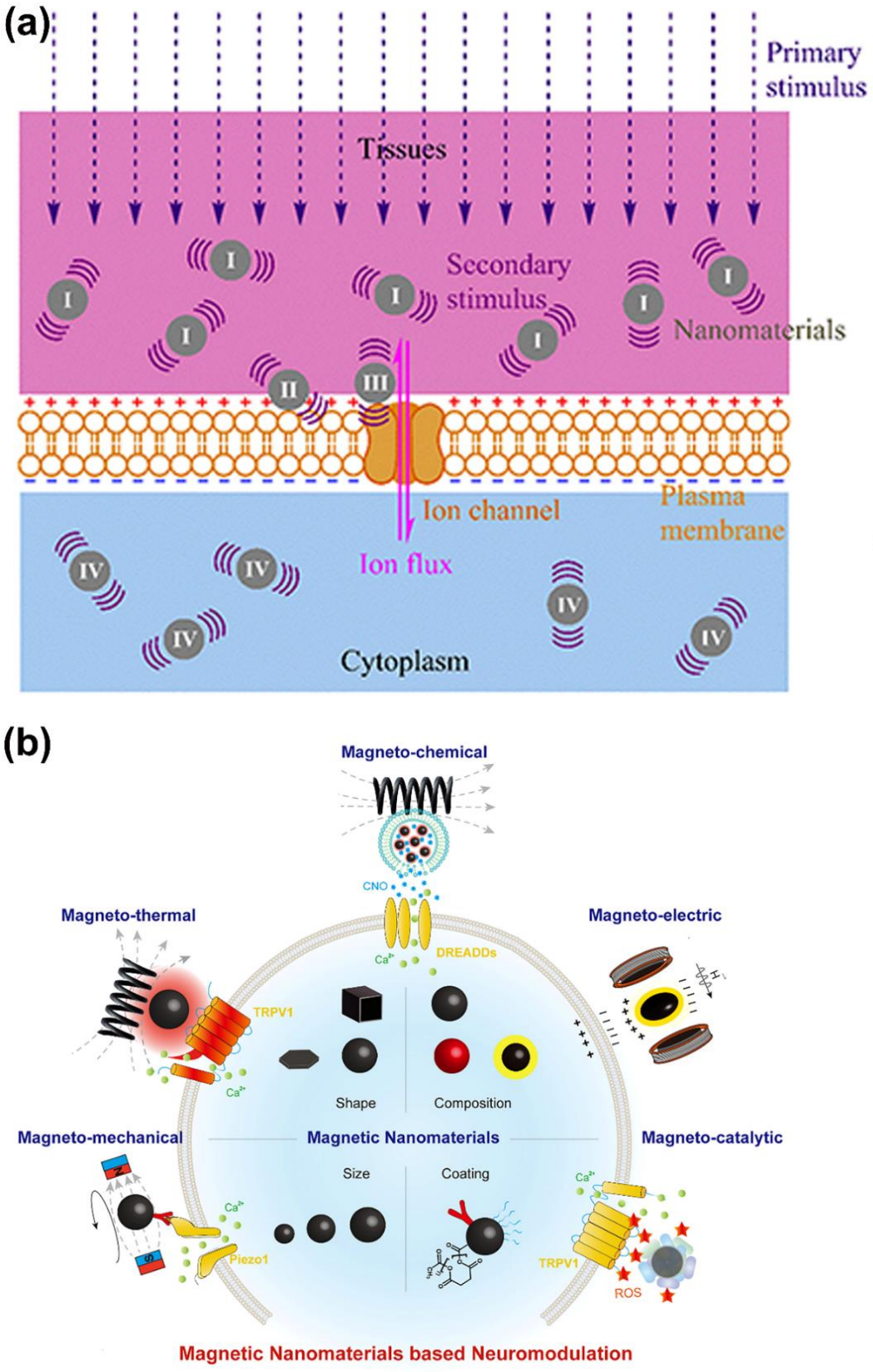

Fig. 1-4: Schematic representation of (a) the general principle involved in tissue stimulation. Used under the Creative Commons Attribution 4.0 License from [53]; (b) various responses of magnetic nanomaterials (MNPs) in response to different types of external stimuli. Adopted with permission [142] copyright© 2023 Wiley Periodicals LLC

Alternating magnetic field (AMF): Can generate heat that activates heat-sensitive channels like TRPV1. Additionally, under an AMF, MNPs can be used to deliver drugs that target designer receptors (DREADDs) on brain cells. Radio waves (RFs): Can create electrical effects within MNPs that directly influence brain cell activity. Additionally, under RFs, MNPs combined with a protein called ferritin can activate TRPV1 channels [142]. Additionally, MNPs can be engineered for ion-transporting proteins incorporation. These proteins, expressed transgenically in neurons, respond to stimuli generated by the MNPs, such as mechanical force, electricity, or heat [147]. Magnetic stimulation with nanomaterials is a more effective way to stimulate the brain without surgery. It can reach deeper brain regions and activate specific groups of brain cells involved in certain functions [27, 146, 148].

1.5 Fabrication technologies for magnetic neuromodulation

High-resolution neuromodulation, whether invasive, noninvasive, or minimally invasive, relies on precisely designed coils. Miniaturising these coils using different techniques is essential for achieving this precision. This section briefly explores various methods used in fabrication of coils for neurostimulations. One of these techniques is through-silicon vias. This method enables the creation of various coil geometries, including 3D solenoids, toroids, and 2D spiral coils [149-153]. Surface micromachining is another technique for creating high-precision coils such as spiral micro-coils [154]. This multi-step process involves selecting a substrate, depositing thin films for the coil and sacrificial layers, precise patterning using photolithography, and finally etching to define the final coil structure [155-157]. Lithography has also been used in micro-coils fabrication, enabling the creation of high-precision structures like high aspect ratio cylindrical micro-coils [158]. Processes such as screen printing, inkjet printing, electrohydrodynamic printing, and aerosol jet printing are utilised to create parts with precise control over their composition and architecture for a broad range of utilities at both the macro- and micro-scale [159-161]. Existing microfabrication techniques, including through-silicon vias, surface micromachining, lithography, and 3D printing, have established themselves in micro-coil production [159, 160]. This study, however, breaks new ground by presenting a novel approach that utilises electroplating and laser cutting for micro-coil fabrication.

2 Principles of simulations and employed physics

2.1.1 Physics and theory of electromagnetic

Cells with electrical excitability including muscle cells and neurons, can be triggered by employing an electric field over them [162]. In magnetic neurostimulations such as TMS, a time-dependent EM field is utilised to apply an electric field in the brain over neurons. Maxwell's equations, specifically Faraday's induction law and circuital law of Ampère's, dictate the behaviour of the EM field [163, 164].

$$\nabla \times \boldsymbol{E} = -\frac{\partial \boldsymbol{B}}{t} \quad \textbf{(2-1)}$$

$$\nabla \times \boldsymbol{B} = \mu_0(\boldsymbol{J} + \varepsilon_0 \frac{\partial E}{\partial t}) \quad \textbf{(2-2)}$$

In this context, $\boldsymbol{E}$, $\boldsymbol{B}$, $\boldsymbol{J}$, ε_0, μ_0 and ($\varepsilon_0 \partial E/\partial t$) represents the electric, and magnetic fields, the current density, the free space permittivity (8.854×10^{12} F/m) and permeability ($4\pi \times 10^{-7}$ H/m), and the displacement current, respectively. When handling sinusoidal signals, working in the frequency domain is considerably easier compared to the time domain [165].

$$\nabla \cdot \boldsymbol{D} = \rho \quad \textbf{(2-3)}$$

$$\nabla \times \boldsymbol{H} = \boldsymbol{J} + j\omega \boldsymbol{D} \quad \textbf{(2-4)}$$

$$\nabla \times \boldsymbol{E} = -j\omega \boldsymbol{B} \quad \textbf{(2-5)}$$

$$\nabla \cdot \boldsymbol{B} = 0 \quad \textbf{(2-6)}$$

Here $\boldsymbol{D}$, ρ, $\boldsymbol{H}$, and ω representing the density of the electric flux, the charge density/distribution, the magnetic field, and the angular frequency, respectively. ω is a real quantity equal to $2\pi f$, where f denotes the frequency. In these equations, all 3D complex vector fields are presented in bold, while all scalar quantities are non-bold [165, 166].

It has been shown that when modelling noninvasive magnetic stimulations, it is possible to roughly decouple these equations and is permissible to make several approximations, including the current in the coil is uniformly in phase across all sections of the coil, and the magnetic field within the relevant volume is synchronised with the current of the coil, there is no significant magnetisation observed in any tissue and the displacement currents can be considered negligible [165-168]. This EM state is commonly known as "quasi-static" state

[167, 168]. Studies indicate that the induced currents in body tissues during TMS result in a minimal magnetic field, even in cerebrospinal fluid, where the conductivity is approximately 2 S/m [169]. Given these approximations, magnetostatics from Eq. (2-2) could be applied to initially calculate the coil's magnetic field. Subsequently, in the tissue the generated electric field can be calculated employing this magnetic field using Eq. (2-1). The governing magnetostatics equations in a free space include Gauss's magnetic and static version of Maxwell–Ampère's laws [166, 170].

$$\nabla . \boldsymbol{B} = 0 \tag{2-7}$$

$$\nabla \times \boldsymbol{B} = \mu_0 \boldsymbol{J} \tag{2-8}$$

Considering Eq. (2-8), the absence of magnetic charges can be noticed from the magnetic form of Gauss's law. Furthermore, it can imply the solenoidal configuration of the magnetic flux density, meaning it is free of divergence [171]. This indicates that $\boldsymbol{B}$ can be expressed as the curl of an alternative vector field:

$$\boldsymbol{B} = \nabla \times \boldsymbol{A} \tag{2-9}$$

where $\boldsymbol{A}$ represents the magnetic vector potential [172]. Based on Helmholtz's theorem a vector field can be uniquely determined (till a constant) by its divergence and curl. Selecting the potential of magnetic vector divergence is not straightforward, and one of the various options is the Coulomb gauge [173].

$$\nabla \cdot \boldsymbol{A} = 0 \tag{2-10}$$

The electric potential provides a more streamlined expression for the equations governing steady and electrostatics currents. Similarly, $\boldsymbol{A}$ offers a more efficient means of formulating the equations. This provides a physical interpretation for $\boldsymbol{A}$, as its negative derivative of the time corresponds to the electric field $\boldsymbol{E_m}$ [165, 166, 170].

$$\boldsymbol{A}_{(r)} = \frac{\mu_0}{4\pi} \int_{\Omega} \frac{J_0(\acute{r})}{|r - \acute{r}|} d^3\acute{r} \tag{2-11}$$

where J_0, r, and r' represent respectively the current source, the vector position of the field, and source points. The primary magnetic and electric field physics utilised in COMSOL Multiphysics numerically solve Eqs. (2-11, 2-10, 2-9). The primary magnetic and electric field physics utilised in Sim4Life was derived using Biot-Savart law (Eq. (2-11)) and Eq.2-9 [174].

2.1.2 Theory for Heat Transfer in Solids

This section delves into the heat transfer equation used in COMSOL Multiphysics. Established using the thermodynamics first law (fundamental of energy conservation). According to the thermodynamics 1st law, changes in the internal energy (E_Ω) and total kinetic energy (K_Ω) within a domain (Ω) can be attributed solely to two factors: the mechanical power exerted by external forces (P_{ext}) and the net heat transfer rate (Q_{exch}) across the domain's boundaries [175]. Mechanical laws, either for fluids or solids, yield a key balance equation: the change in kinetic energy within a system equals the work done by internal stresses (P_{str}) plus the work done by P_{ext}. This highlights the importance of both momentum and mass considerations for a complete system description and describes how forces acting on macroscopic scales affect its overall movement, with changes in kinetic energy corresponding to measurable displacements, which is the domain addressed by physics interfaces such as single-phase flow and solid mechanics in COMSOL Multiphysics [175]. The heat balance equation arises from the combination of these facts, providing a powerful tool for analysing heat transfer phenomena. This equation bridges the gap between microscopic phenomena like atomic vibrations and the macroscopic experience of heat, using quantities like Q_{exch} and E_Ω [175]. The Q_{exch} considers heat transferred via thermal radiation, conduction (governed by Fourier's Law), and potentially other relevant heat sources depending on the specific system under consideration. The equation of heat balance in the spatial framework by considering all these elements can be expressed as:

$$\rho\frac{\partial E}{\partial t} + \rho\boldsymbol{u}\cdot\nabla E + \nabla\cdot(\boldsymbol{q}+\boldsymbol{q_r}) = \sigma:\boldsymbol{D} + \boldsymbol{Q} \tag{2-12}$$

Here, ρ, $\boldsymbol{u}$, $\boldsymbol{D}$, and σ represents the density, velocity vector, tensor of strain rate and Cauchy stress, respectively. The contraction is presented by operation ":" and here can be expressed as $a:b = \sum_n\sum_m a_{nm}b_{nm}$. Where $\boldsymbol{q}$, $\boldsymbol{q_r}$, and $\boldsymbol{Q}$ stands for the conduction heat flux, radiation heat flux, and additional heat sources. This statement expresses the local energy balance principle, where the temporal variation of internal energy is equated to the sum of conductive, convective, dissipative, and radiative heat fluxes, along with volumetric heat sources. In COMSOL Multiphysics, the heat transfer in the interface of solids is addressed by Eq. (2-12) that can be rewritten as Eq. (2-13) [175].

$$\rho C_p\left(\frac{\partial T}{\partial t} + \boldsymbol{u_{trans}}\cdot\nabla T\right) + \nabla\cdot(\boldsymbol{q}+\boldsymbol{q_r}) = -\alpha T:\frac{dS}{dt} + \boldsymbol{Q} \tag{2-13}$$

where C_p, T, $\boldsymbol{u}_{trans}$, α, and S stands for the specific heat capacity, absolute temperature,

translational motion velocity vector, thermal expansion coefficient, and second tensor of Piola-Kirchhoff stress. In a steady-state system, where temperature remains constant over time, terms involving time derivatives (rates of change) vanish from the equation. This is because these terms represent the dynamics of how temperature evolves, which isn't relevant when temperature is fixed [175, 176].

3 Micro-coils computational models

3.1 Backgrounds and Aims

The initial phase of this work involved simulation studies to design circular spiral micro-coils. First the behaviour of the coils at a low current (100mA) and frequency range (1-3 kHz) was investigated. This was done to compare the results obtained from two different simulation software packages, COMSOL and Sim4Life. The study utilised Sim4Life software, which boasts the capability of modelling a complete human head. This comparison aimed to identify any discrepancies in the outcomes when simulating on a head model (using Sim4Life) versus a free-air environment (using COMSOL). This evaluation was crucial to determine if using COMSOL with a simpler air model could be considered an acceptable alternative to Sim4Life for this specific application. Subsequently, further simulations were conducted using COMSOL Multiphysics with a wider range of currents (1-5A) and frequencies (5 Hz-100 kHz) to optimise the design and generate a set of results that could be compared with the experimental measurements from the fabricated coils.

The physiological effects of magnetic brain neurostimulation occur by generating an EM field within the body [177]. Therefore, the specific characteristics of this field play a crucial role in determining the resulting physiological response to magnetic neurostimulations [178]. Practically, the neurostimulation process can be characterised by two main factors (a) parameters that influence the distribution of the EM field spatially (i.e., the characteristics of the stimulating coil, such as its size, position, shape, and electrical properties), (b) parameters associated with the applied voltage or current waveform to the coil, which influence the temporal properties of the EM field, such as width, amplitude, frequency, and pulse shape [168, 179-183]. Ensuring control and proper recording of these neurostimulation parameters guarantees the EM brain neurostimulation reproducibility [168, 179-183]. Taking the factors mentioned above into consideration, choosing the optimal strategy for modelling electromagnetic fields hinges on two main aspects: numerical accuracy, which guarantees a solution that closely matches the true behaviour, and computational burden, referring to the amount of memory and time required for the calculation. Furthermore, the numerical method efficiency considers three key aspects: memory usage, total computation time, and how quickly that time increases as the problem gets bigger (scalability). This helps to choose methods that can handle problems of varying complexity without excessive resource demands. To consider these, the current research involved designing a spiral circular micro-

coil and incorporating it into a system with two such coils. The magnetic fields generated by these coils were analysed using electromagnetic (EM) modelling software, specifically Sim4Life and COMSOL Multiphysics. The simulations were conducted on a model of the human head, considering it a conductive medium, with micro-coils placed on the surface of the skull. Sim4Life's generated magnetic fields were analysed with a 100-mA current at 1-3 kHz frequencies. This choice of parameters stemmed from the limitations of the available experimental setups, as the available power supply could only generate a maximum current of 100 mA. This data was compared to magnetic fields produced in COMSOL Multiphysics under identical conditions. Subsequently, COMSOL Multiphysics software was employed to investigate the behaviour of the micro-coils across a broader range of currents (1A-5A) and frequencies (5 Hz-100 kHz). This exploration was driven by the study's objective of achieving a strong magnetic field within the low-frequency domain. Faraday's law of electromagnetic induction establishes a direct relationship between the strength of a magnetic field and the applied current. Therefore, higher currents were also examined. The effect of current direction on the B-field was also examined by altering the current input terminals in the designed coils.

In designing coils for magnetic neurostimulation, it is crucial to consider not only the B-field but also the heat generated within and around the coils [135]. This is essential for several reasons such as coil functionality, patient safety, comfort, and compliance [179, 180, 184]. Excessive heat can accelerate material degradation, shortening the coil's lifespan and can lead to skin burns or tissue damage [183-186]. Magnetic neurostimulation procedures necessitate adherence to strict safety guidelines regarding temperature limits within the targeted tissue and surrounding areas [187]. Uncomfortably warm sensations during magnetic neurostimulation treatment can lead to patient discomfort and potentially reduced compliance with the therapy. Maintaining comfortable temperatures enhances the treatment experience and encourages successful completion [183, 184, 186]. Therefore, evaluating, and optimising heat generation in coil designs is essential. To investigate heat generation in micro-coils and their surrounding environment during operation, heat transfer simulations were conducted in COMSOL Multiphysics across a range of currents (1A-5A) and frequencies (5 Hz-100 kHz).

3.2 Electromagnetic Modelling

3.2.1 COMSOL Multiphysics

In order to precisely predict the intensity and location of local magnetic- and electric-field gradients, micro-coils are modelled using COMSOL Multiphysics through the Magnetic and Electric Field (mef) interface. Simulations based on FEM are conducted to determine the gradients of the generated magnetic and electric fields within the micro-coils due to the current flows under various conditions. Maxwell's equations are solved in this physics interface, employing the magnetic vector and the scalar electric potentials as the dependent variables in the formulation. The Current Conservation feature and Ampère's Law are the primary node, incorporating equations for the magnetic vector and electric potentials. It also offers a platform for specifying constitutive relationships and characteristics associated with them like electrical conductivity, relative permittivity, and relative permeability [166, 188]. Boundary conditions for the magnetic and electric fields interface are implemented through a two-step process. This is necessary as only certain combinations of magnetic and electric boundary conditions hold physical relevance, while others may result in nonphysical models that contradict the principle of current conservation. (i) In the absence of surface currents, the conditions set by the physics interface are applied for magnetic boundary conditions as ($n_2 \times (\mathbf{H}_1 - \mathbf{H}_2) = 0$, $n_2 \times (\mathbf{A}_1 - \mathbf{A}_2) = 0$) and must be satisfied. As **A** is computed by the physics interface, the continuity of the tangential aspect of the magnetic potential is preserved, thereby automatically satisfying the first condition. Given the equivalence of the second condition to the natural boundary condition, it is inherently satisfied. (ii) Continuity represents the essential physics interface condition applicable to both internal and external interfaces between dissimilar media ($n_2 \cdot (\mathbf{J}_1 - \mathbf{J}_2) = 0$), which is automatically satisfied by default, meaning it holds true unless we actively introduce counteracting forces [166, 188, 189].

3.2.2 Sim4Life platform

A commercially available FDTD simulation platform called Sim4Life was utilised to conduct the simulations. This software integrates multiple physics solvers with sophisticated anatomical models of both animals and humans. It offers comprehensive capabilities, enabling simulation, modelling, analysis, and visualisation with great flexibility based on time domain solving of Maxwell's equations [166, 188, 189].

3.3 Methodology

3.3.1 COMSOL Simulations

The simulation was conducted within a 3D model in the air, where the simulation assumed a relative magnetic permeability of 1. The model incorporated two copper micro-coils, which allowed for the solution of the ruling equations and yielded precise results numerically within a reasonable computational time. The design drew inspiration from literature reviews [190] but faced several limitations. First, the wire diameter needed to stay within the micrometre range. Second, the spacing between the coils was restricted by the hardware used for fabrication (i.e., a laser cutting machine). Since the laser cutting machine's tip had a diameter of 50 microns, the minimum achievable spacing between coils was 60 microns. While the wire width needed to be larger than the spacing for functionality, excessively large dimensions for both elements would result in an overall micro-coil that exceeded size constraints.

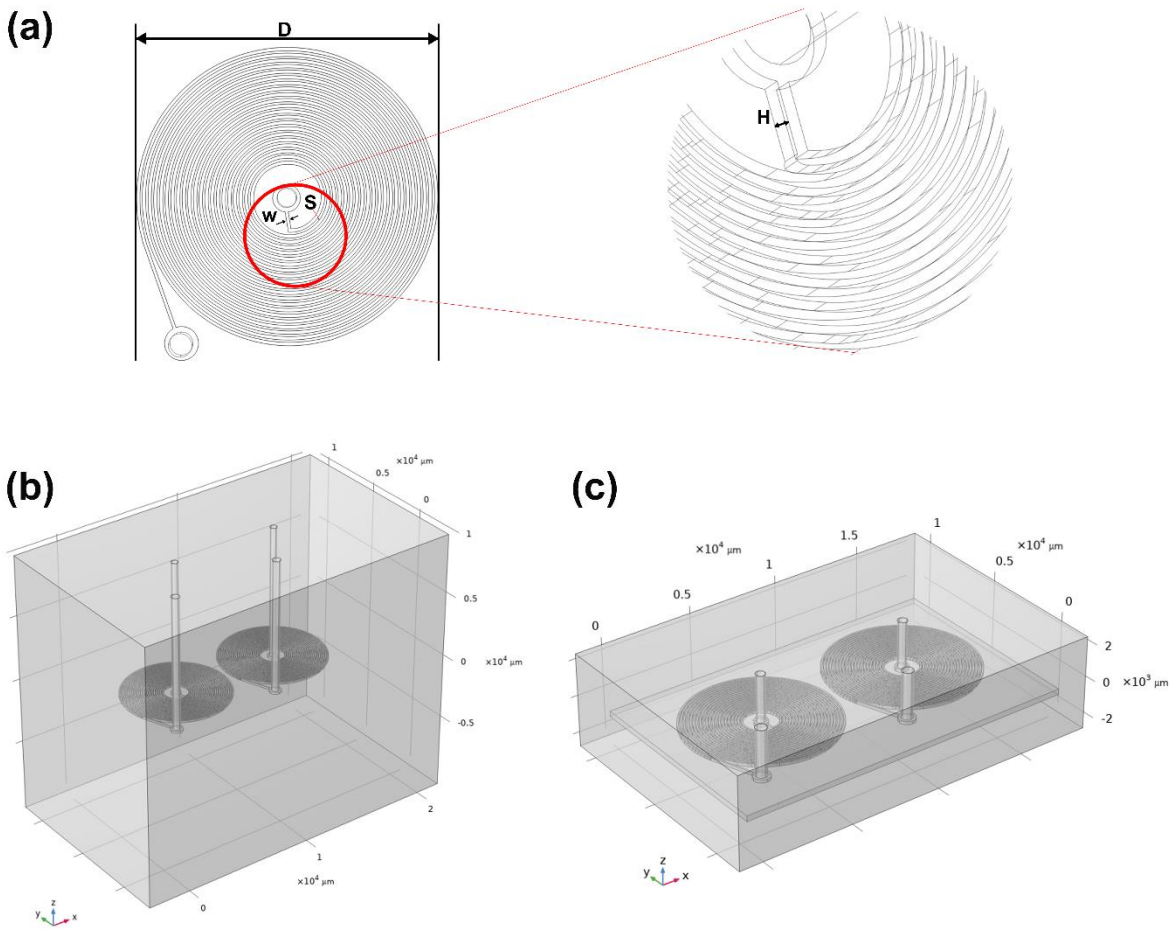

Fig. 3-1: (a) Geometric parameters of the coil used to generate magnetic fields. The COMSOL designs used in simulations to analyse the coil's behavior at (b) low current (100 mA) and low frequency (1-3 kHz) range, and (c) at higher current (1 A - 5 A) and wider frequency ranges (5 Hz - 100 kHz)

Fig. 3.1 shows (a) the detailed dimensions of the coil with 20 turns with diameter (*D*) of 7.8 mm, having a width (*W*) of 85 µm, spacing (*S*) of 70 µm, and thickness (*H*) of 150 µm responsible for generating magnetic fields, (b) the setup of a COMSOL simulation designed to analyse the coil's behaviour under the low current (100 mA) and low frequency ranges (1-3 kHz), and (c) the configuration of another COMSOL simulation intended to examine the coil's performance at higher current (1 A - 5 A) and a broader frequency ranges (5 Hz - 100 kHz). Each comprising two circular micro-coils, in the design (c) coils were positioned over a nonconductive FR-4 substrate with a copper coating that is etched in the form of a spiral. Details of the substrate is given in section 4.2.4. The FR-4 substrate measures 18 × 11 mm in a height of 300 µm. The environment and micro-coils were split-up employing the physics-controlled finer mesh from the Mesh node's settings and simulated. The generated magnetic fields and their associated spatial gradients generated by micro-coils, were simulated using COMSOL Multiphysics software, with a specific focus on the region above the coil's surface.

3.3.2 Sim4Life Simulations

In this study simulations were done employing the Magneto-Quasi Static module within the software suite (Sim4Life v.7.0.0.7995, ZMT, Zurich MedTech AG), which leverages a decoupling approach for the electric and magnetic field computations, thereby efficiently determining the electromagnetic solution. The magnetic field solution was derived using Biot-Savart law (Eq. (2-11)) and Eq.2-9 [174].

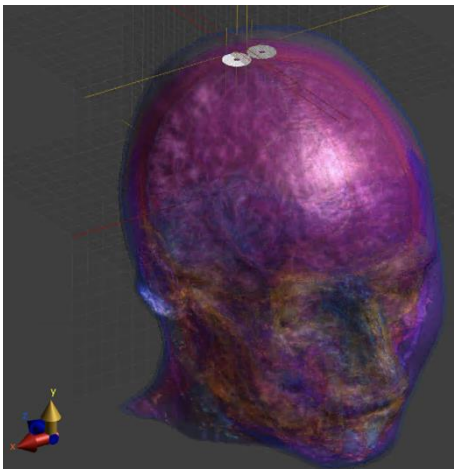

Fig. 3-2: The three-dimensional head model used in Sim4Life analyses

In this study, the head model used for the simulations was the 'MIDA (Multimodal Imaging-based Detailed Anatomical)' model, obtained from the software library. Fig. 3-2 illustrates a three-dimensional (3D) representation of the head model used in the study, positioned within the cartesian coordinate system. This model encompassed all layers of tissues present in the head. The head model had a mass density of 1000 kg/m^3, an electrical conductivity of 10^{-6} S/m, and a relative magnetic permeability of 1. These specific values are suitable for modelling the tissue of human brain in the low-frequency EM range, utilizing the Magneto Quasi-Static solver. The circular micro-coils coils, comprising a total of 21 turns in total design were positioned above the MIDA head model. During the design process, the coil configuration was formed in a spiral shape. Gold was utilised as the material for the coil, possessing an electrical conductivity of 45.6×10^6 S/m.

3.3.3 Heat transfer modelling

To precisely predict the intensity and location of local heat gradients, micro-coils are modelled using COMSOL Multiphysics through the Heat Transfer in Solids interface. Simulations based on FEM are conducted to model heat transfer in micro-coils resulted by radiation, convection, or conduction under various conditions. The simulation was conducted within the same 3D model which was used for the electromagnetic modelling. The design of micro-coils for this study is shown in Fig. 3-1c. Within solid regions, the heat diffusion equation coincides with the differential form of Fourier's law, which correlates the gradient of temperature with the flux of heat. Upon adding this specific physics interface, the Model Builder incorporates several fundamental constructs: a "Solid" domain, a default boundary condition named "Thermal Insulation" (representing zero heat flux), and initial temperature specifications (room temperature). The heat transfer simulations were conducted at various current (1 A - 5 A) and frequency (5 Hz - 100 kHz) ranges.

3.4 COMSOL and Sim4Life simulation results

Fig. 3-3 illustrates a sliced view of the generated magnetic fields on the vertex by the custom-designed micro-coils at 3kHz placed on the head model used in the Sim4Life software. When the frequency is varied in COMSOL with a constant current, the wavelength of the EM field correspondingly changes. According to Maxwell’s equations, the created electric field directly depends on the frequency of the B-field. Fig. 3-4 compares electric fields resulting

from the application of three distinct frequencies (1-3 kHz). As already mentioned, the primary magnetic and electric field physics utilised in COMSOL numerically solve Eqs. (2-11, 2-10, 2-9).

Data from Fig. 3-4 reveals, the frequencies utilised do not affect the self-inductance of the coils and were close to the quasi-static solution. The spatial distribution and direction of the magnetic field (B-field) are visualised using streamline surfaces in Fig. 3-5.

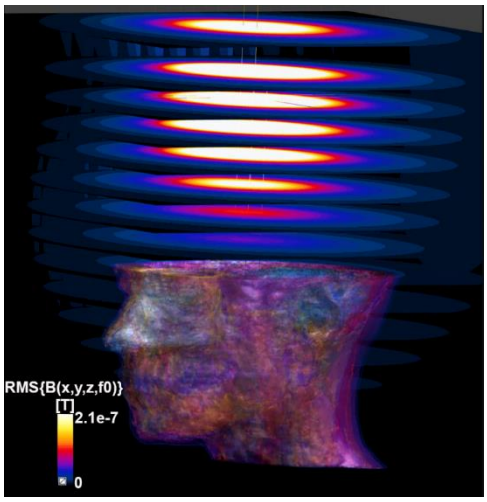

Fig. 3-3: The Sim4Life MIDA head model utilised in this study with a sliced view of the generated magnetic fields by the custom-designed micro-coils

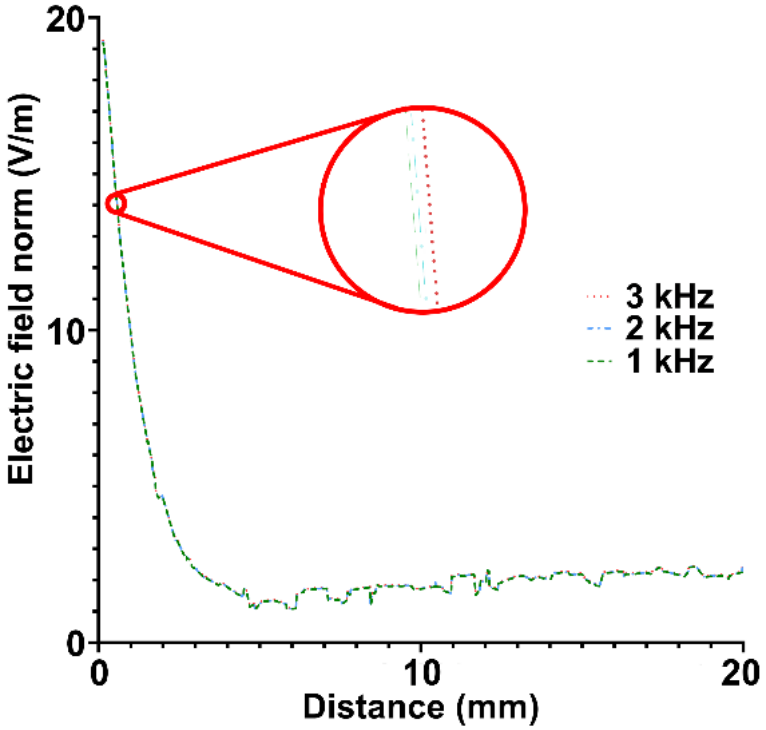

Fig. 3-4: The axial electric field (z-direction) at various radial positions around the coil's face obtained using COMSOL software for different applied frequencies. Due to symmetry around the coil axis, only half of the field profile is presented

The thickness of the coil wires in this research was set to be ten times smaller than the minimum skin depth and hence no discernible variation in the magnetic flux density was observed. Notably, the streamlines demonstrate a higher concentration near the centre of the coil, indicating a stronger B-field in that region.

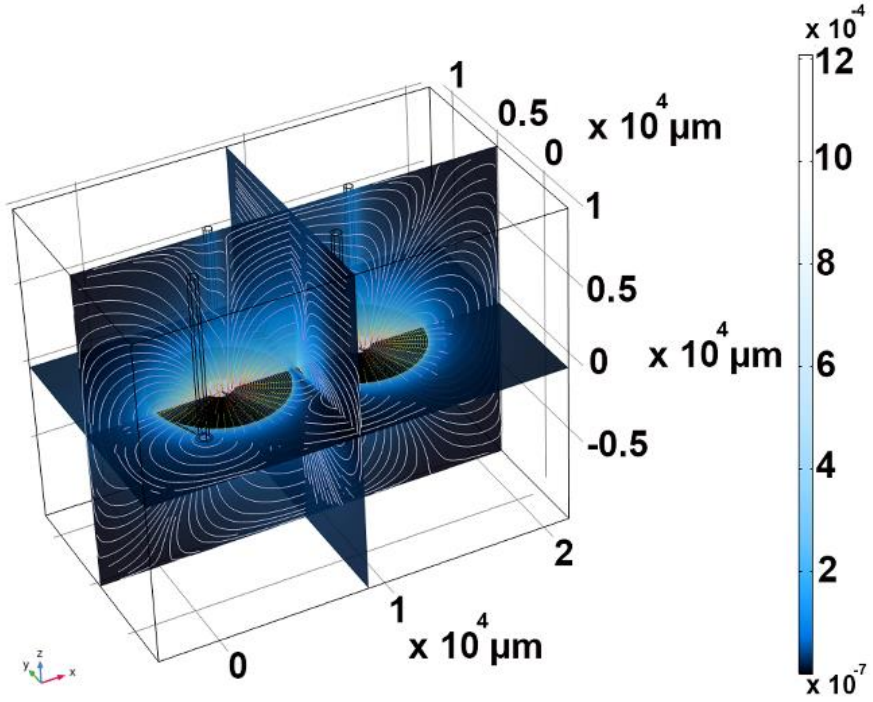

Fig. 3-5: Cut-plane streamline plot of magnetic flux density (B-field) for 3 kHz (scale-bar unit is militesla)

In other words, the B-field strength is most prominent at the centre of the coil and decreases as the distance from the centre increases as confirmed by data in Fig. 3-5. The axial (norm) flux density of the magnetic field was measured at different positions in the z direction across the face of the designed micro-coils for various applied frequencies, as shown in Fig. 3-6.

In Fig. 3-6a, the initial observation suggests that the results obtained from COMSOL do not show significant differences in response to the different frequencies employed. This is due to residual errors in the frequency domain iterative solver [191-194]. For more precise computation, direct solvers should be employed, and finer meshes can be used at the boundaries to accurately capture the skin depth effect.

The data obtained from Sim4Life simulations, as shown in Fig. 3-6b demonstrates a similar trend in terms of the obtained magnetic field. As the frequency of the alternating current (AC) increases, the B-field flux also increases, and there are no noticeable changes in the

field with different frequencies. This improvement in stability makes the design more suitable for neurostimulation purposes. The equation used to calculate the magnetic field when the frequency is swept with constant current is the Maxwell-Faraday (Eq. 2-1). The results indicate that by employing frequencies in the range of 1 to 3 kHz and a stimulating current of 100 mA, average magnetic field values ranging from 0.1 to 0.8 mT were achieved. Moreover, the simulations demonstrated that such magnetic neurostimulation enabled penetration into the brain tissue, reaching depths of up to 2 cm.

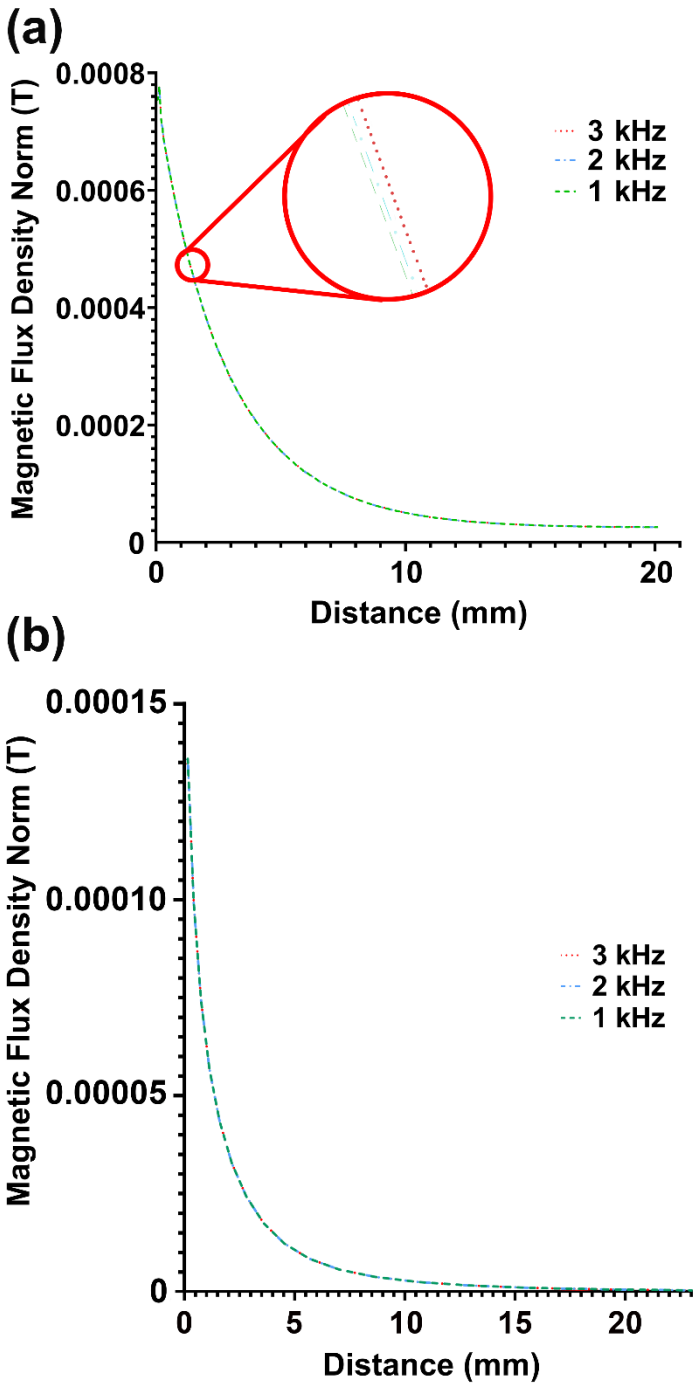

Fig. 3-6: The axial magnetic flux density (z-direction) at various radial positions around the coil's face obtained using (a) COMSOL and (b) Sim4Life software for different applied frequencies. Due to symmetry around the coil axis, only half of the field profile is presented

Fig. 3-6 reveals that B values in COMSOL are higher compared to those calculated using Sim4Life. This difference could be attributed to several factors, including (i) variations in micro-coils geometry, (ii) differences in boundary conditions, (iii) variations in mesh resolution, and/or (iv) the influence of the skin depth effect. In Sim4Life, the coil was modelled using a 2D boundary element, whereas in COMSOL, a 3D domain with finite thickness was employed. This distinction arises from the predominant use of boundary elements in the Sim4Life simulation, while COMSOL utilises finite volumes. The former models the EM field at the boundary of a domain, while the latter models the EM field throughout a domain.

Briefly, in Sim4Life, the coil is represented by a surface. The surface is segmented into a mesh of elements, and the EM field is solved at the nodes of these elements. The thickness and breadth of the coil were not explicitly modelled in Sim4Life, but they could be estimated from the dimensions of the surface. However, in COMSOL, the coil is represented by a volume. The volume is segmented into a mesh of elements, and the EM field is solved at the nodes of these elements. The thickness of the coil was explicitly modelled in COMSOL and specified as 150 μm. Furthermore, COMSOL models the skin depth through the volume mesh, while Sim4Life calculates the skin depth using the grid settings. At frequencies significantly below the skin depth, the current passes within the entire thickness of the conducting element. However, at higher frequencies, the magnetic field becomes concentrated near the surface. These differences in modelling the skin depth could explain the observed disparities in the magnetic field density between the two modelling platforms.

Building upon previous studies and aiming to gain deeper insights into the behaviour of micro-coils under higher currents and frequencies, COMSOL Multiphysics was employed for detailed simulations. Investigations were conducted across a broad frequency spectrum, spanning from 5 Hz to 100 kHz, and encompassed a diverse range of electric currents, varying between 1 A to 5 A. The B-field distribution spatially and its direction are visualised using streamline surfaces in Fig. 3-7. The effect of current direction on the B-field was also examined by setting up the electrodes A, C, and B, C as current inputs. As aforementioned, in this study, coil wires with dimensions ten times smaller than the minimum skin depth were used to effectively eliminate variations in B-fields due to current distribution within the conductor. Considering Fig. 3-7, the B-field is observed to be strongest near the centre of each coil like previous observations in Fig. 3-5, as visualised by the higher concentration of streamlines in these regions. The density of magnetic field lines provides a visual representation of the strength of the magnetic field in a specific region. This is because the

number of B-field lines per unit area passing through a surface perpendicular to the lines which depends on the B-field magnitude in that area [195].

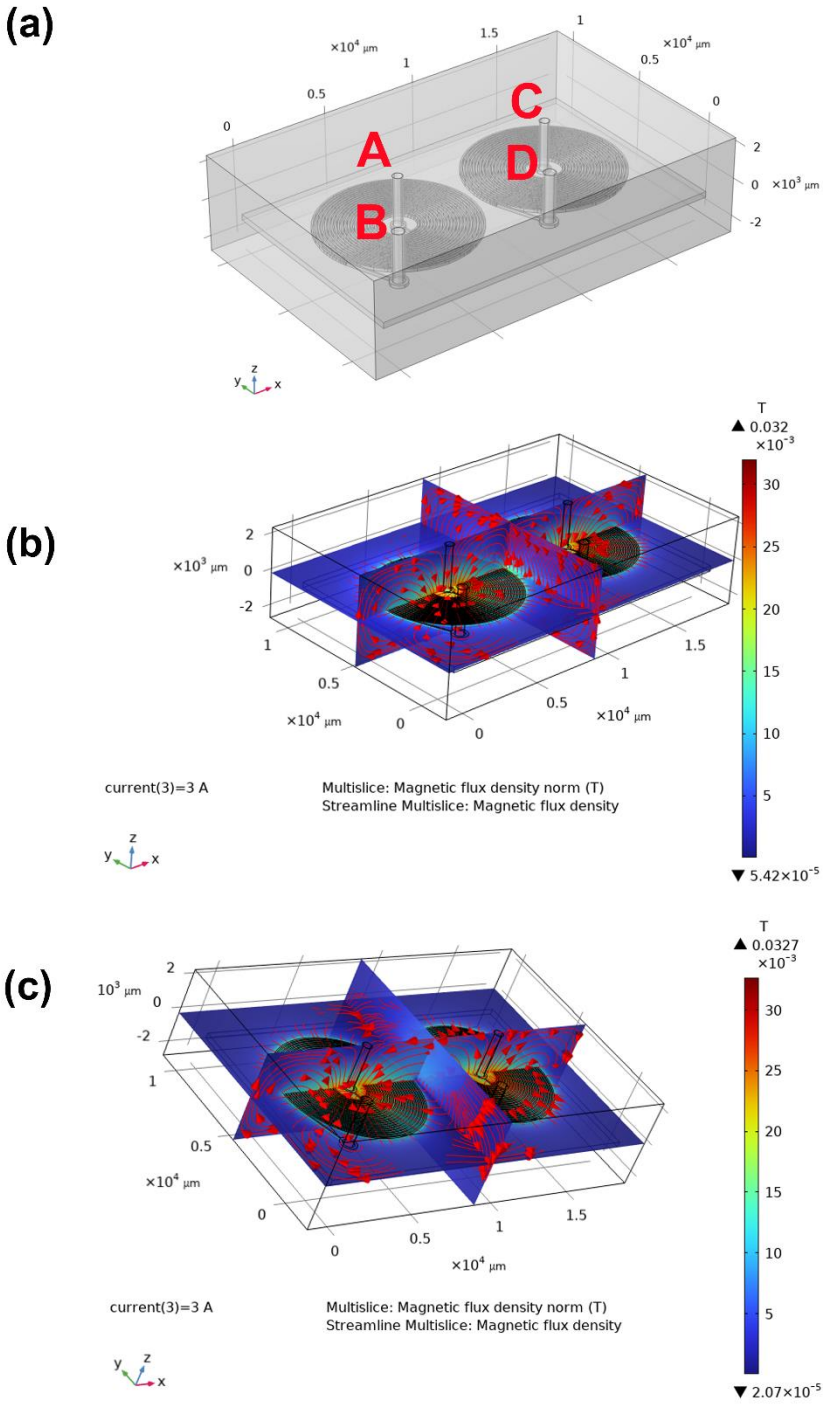

Fig. 3-7: (a) The design of the micro-coils employed in these simulations includes identification of current terminals and ground connections. A cut-plane streamline plot of the magnetic flux density (B-field) at 3 A and 10 kHz; in plot (b), terminals A and C are the current inputs, and in plot (c), terminals B and C are the current inputs. (scale bar unit: militesla)

Furthermore, comparing Fig. 3-7b and 3-7c highlights the impact of current direction on the B-field between coils. When terminals A and C were used as current inputs so called same

current inputs (Fig. 3-7b), the B-field between the coils reached its highest strength. Conversely, when terminals B and C were used as current inputs so called inverse current inputs (Fig. 3-7c), the B-field between the coils became the weakest. This confirms that the B-field strength is both highest at the coil centre and maximised between coils when currents flow in the same direction, decreasing with both distance from the centre and opposing current directions, as evidenced by the data in Fig. 3-7.

The strength (axial component) of the magnetic field density was measured at different locations around the designed micro-coils. These measurements were taken at various frequencies and are shown in Figs 3-8 and 3-9.

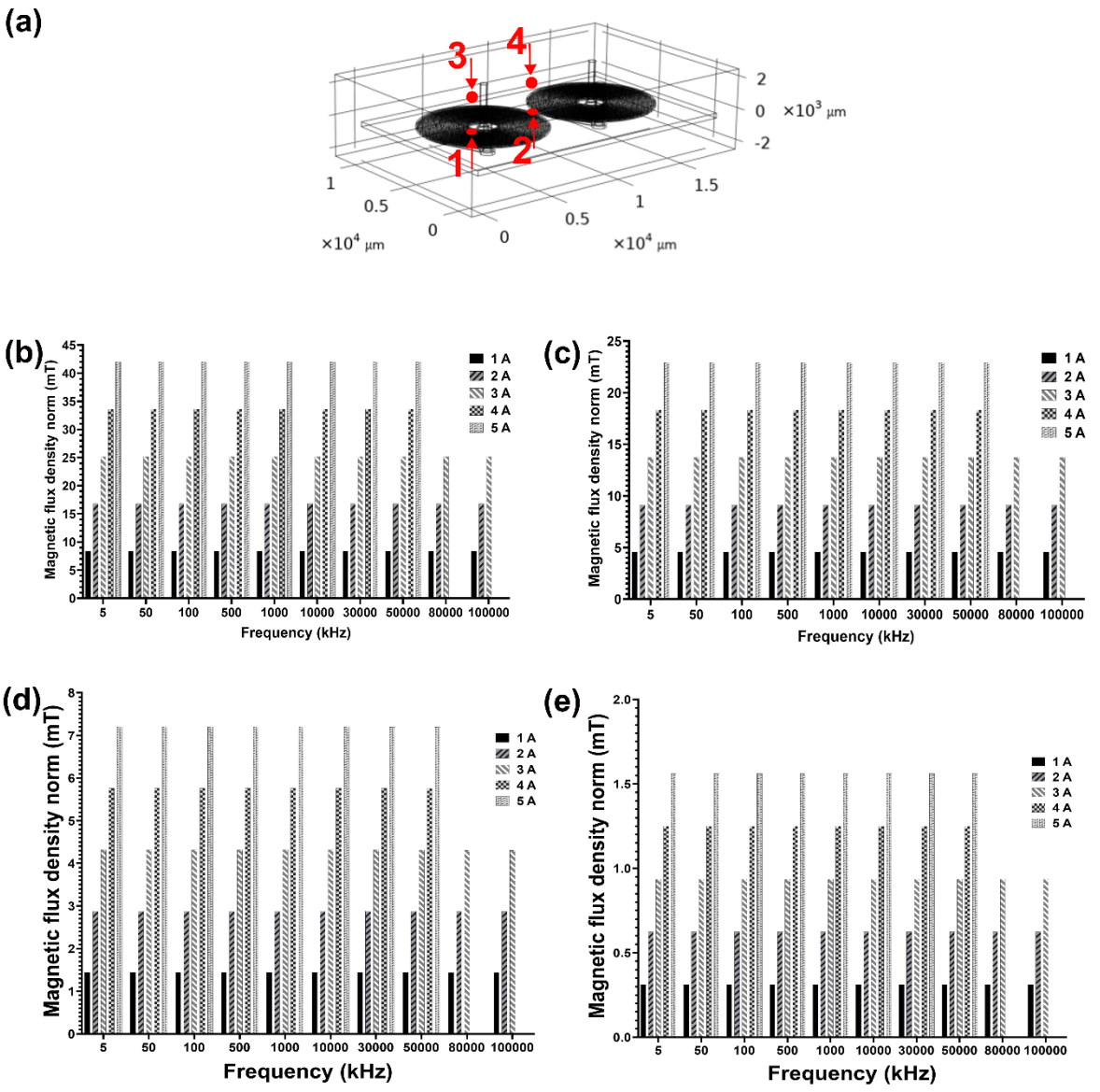

Fig. 3-8: The calculated axial (norm) component of the magnetic flux density across the face of the designed micro-coils in four different points shown in (b) the surface of the coils (x= 3014 µm, 3716 µm, z=0), (c) between to coils (x=8150 µm, y= 4138 µm, z= 0), (d) in 1.99 mm above the coil surface (x=3014 µm, y= 3716 µm, z= 1985 µm) and (e) in 1.99 mm above the coil between two coils (x= 8150 µm , y= 4138 µm , z= 1985 µm) for applied frequencies (5 Hz to 100 kHz) and currents (1-5A), where terminals A and C were used as current inputs

Specifically: (i) on the surface of the coils (z = 0) with two positions along the x-axis (x = 3014 µm and x = 8150 µm) with a fixed y-coordinate (y = 4138 µm) and (ii) 1.99 mm above the coil surface (z = 1985 µm) with two positions mirroring those on the surface, with the same x and y coordinates. Fig. 3-10 shows the strength (axial component) of the magnetic field density at a defined cut line at x= 3014 µm, y= 3716 µm. As shown in Figs. 3-8 to 3-10, increasing the applied current from 1A to 5A strengthens the magnetic flux density at all calculated positions around the coils. However, the magnetic flux density weakens with distance increments from the surface of coils.

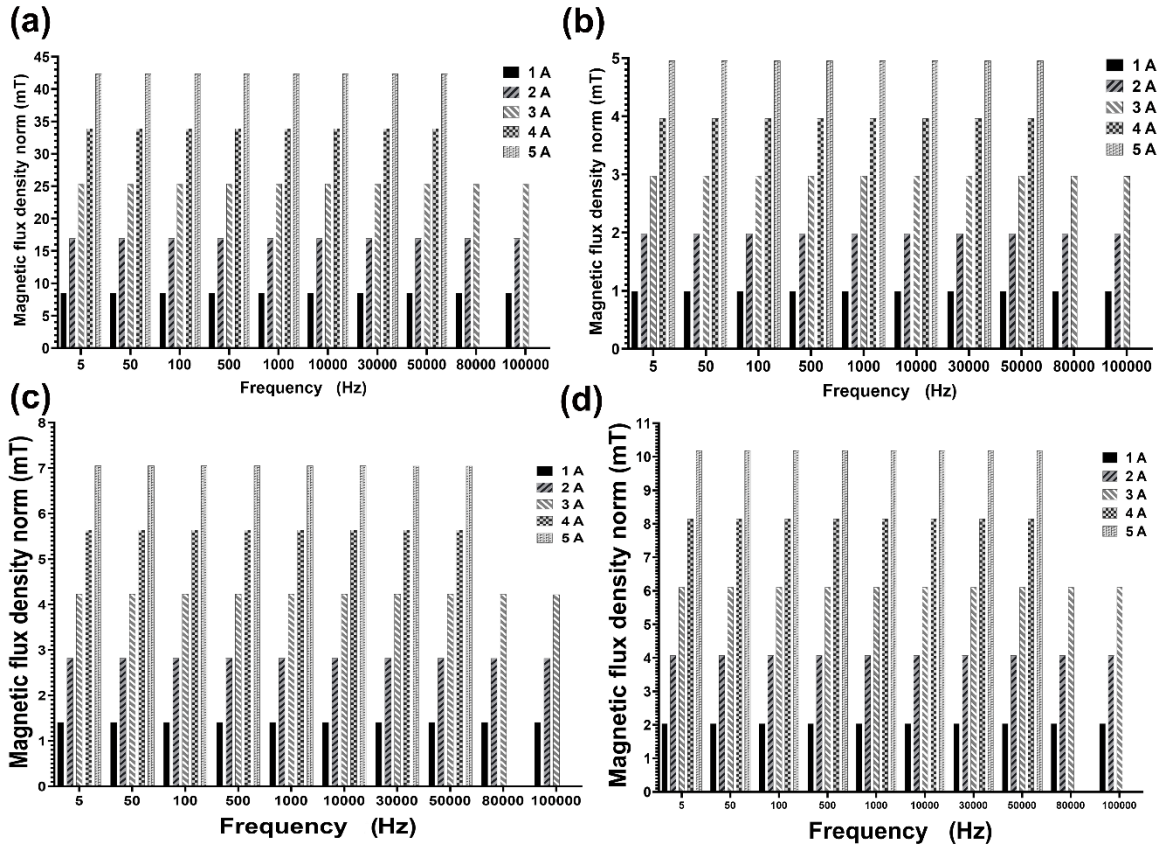

Fig. 3-9: The calculated axial (norm) component of the magnetic flux density across the face of the designed micro-coils in four different points shown in (a) the surface of the coils (x= 3014 µm, 3716 µm, z=0), (b) between to coils (x=8150 µm, y= 4138 µm, z= 0), (c) in 1.99 mm above the coil surface (x=3014 µm, y= 3716 µm, z= 1985 µm) and (d) in 1.99 mm above the coil between two coils (x= 8150 µm , y= 4138 µm , z= 1985 µm) for applied frequencies (5 Hz to 100 kHz) and currents (1-5A), where terminals B and C were used as current inputs

Data show that the B-field on the surface of the micro-coils at position (1) is the strongest for all employed current and frequency ranges. The calculated strength of the B-field ranged from 8.41 to 42.05 mT, for all currents and frequencies at position (1) on the coil surface for both the same and inverse current inputs. However, at the point (x = 8150 µm, y = 4138 µm, z = 0) the calculated strength of the magnetic field ranged from 4.58 mT at 1 A to 22.92 mT at 5 A, when using same current inputs, while it only ranged from 0.99 to 4.95 mT when

using reverse current inputs, for the same employed currents and frequencies. Simulations reveal how the strength of the magnetic flux density above the micro-coils changed with different current levels and depending on the current input directions. In position 3 (1.99 mm above the surface), both configurations (using same or inverse current inputs) showed the magnetic flux density ranging from 1.44 mT at 1 A to 7.20 mT at 5 A. However, in position 4, the strength varied significantly depending on the direction of current inputs. Using the same current input, the magnetic flux density increased slightly with current, ranging from 0.31 mT at 1 A to 1.56 mT at 5 A. Where, using the inverse current input, the strength was stronger, ranging from 2.04 mT at 1 A to 10.18 mT at 5 A.

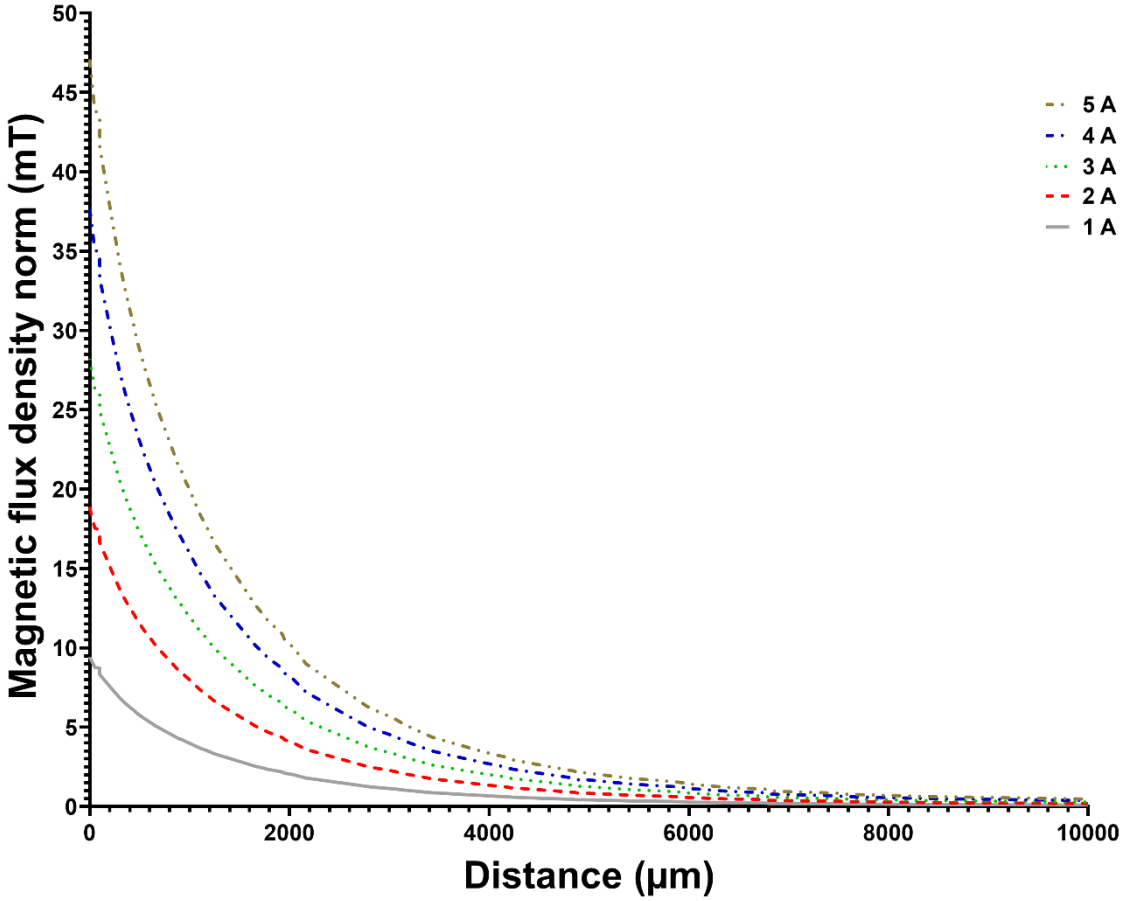

Fig. 3-10: The calculated axial (norm) component of the magnetic flux density across a defined cut line on z direction passing from point x= 3014 µm, y=3716 µm on the surface of the designed micro-coils with the same current inputs

The patterns observed in the B-field strength (shown in Figs. 3-8 to 3-10) is related to the B-field streamlines and flow of the magnetic fields illustrated in Fig. 3-7. As a result, regions with strong B-fields exhibit densely packed field lines, while regions with weak fields have widely spaced lines. The observation also indicates that the outcomes derived from COMSOL exhibit minimal variances in response to varying frequencies, primarily attributed

to residual errors within the frequency domain iterative solver [191-194]. To enhance computational accuracy, direct solvers are recommended, accompanied by the utilisation of finer meshes along the boundaries to effectively capture the skin depth effect. The data in Fig. 3-10 clearly demonstrates a significant decrease in the B-field with increasing distance from the micro-coil surface. At a distance of 1 cm, the B-field weakens from 0.467 mT to 0.093 mT as the current applied to the coil decreases from 5 A to 1 A. This trend continues at a distance of 2 cm, where the B-field further weakens to values ranging from 0.080 mT to 0.016 mT for the corresponding current range. Simulations at position 3 in Figs. 3-8 and 3-9 revealed a consistent trend in the B-field regardless of whether the current input was same or reverse. To verify this observation, a cut line analysis was conducted at the same position. Since the B-field exhibited the same behaviour for both current directions, only the results for same current inputs are presented to avoid redundancy. Fig. 3-11 shows the calculated heat generations in the x direction across the face of the designed micro-coils for various applied frequencies and currents, where the configuration with inverse current inputs was used.

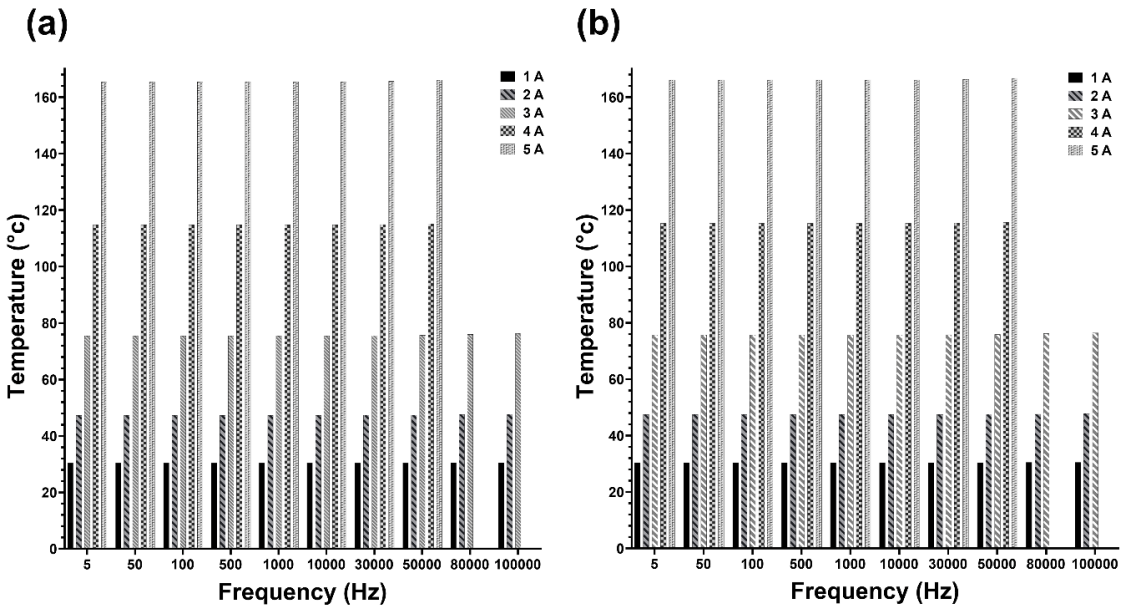

Fig. 3-11: Graphs present simulations of heat generation (a) across the surface of the micro-coils (at x=3014 µm, y=3716 µm, z=0) and (b) between the coils (at x=8150 µm, y=4138 µm, z=0) for various current and frequency combinations. These simulations assume terminals B and C are used for current input

Fig. 3-11 shows that the temperature across the entire surface of the coils increases as the applied current increases, regardless of the specific measurement location. This is because the calculated temperatures at both measured points (on the surface) exhibit the same range, varying from 30.42 °C to 165.38 °C for currents ranging from 1 A to 5 A across all tested

frequencies. For currents above 2A in this coil configuration it is not acceptable to be in contact with the skin.

3.5 Conclusion

This chapter investigated the magnetic fields induced by the micro-coils using two software platforms, COMSOL and Sim4Life. Initially, the simulations applied a constant current of 100 mA and varied the frequency from 1 to 3 kHz. The results have shown that changing the frequency in COMSOL altered the wavelength of the EM field, considering Maxwell's equations and the induced electric field exhibited a direct proportionality to the magnetic field frequency. Where, the applied frequencies had minimal impact on the coils' self-inductance, aligning closely with the quasi-static solution. Additionally, due to the thin coil wire design (10x smaller than the minimum skin depth), no significant variations in magnetic flux density were observed using different frequencies and the magnetic field was strongest at the coil's centre and gradually weakened with increasing distance. Measured axial magnetic flux density across the coil face showed minimal differences across frequencies, likely due to solver limitations. Similar trends were observed in the magnetic field compared to Sim4Life, where increasing the AC frequency resulted in a corresponding increase in the B-field flux and no significant variations in the field were observed across the employed frequencies. The COMSOL and Sim4Life simulations yielded average magnetic field values ranging from 0.1 to 0.8 mT, 0.5×10^{-3} to 0.14 mT, respectively when using 1 to 3 kHz frequencies and a 100 mA current, capable of penetrating brain tissue up to 2 cm deep. A comparison between COMSOL and Sim4Life simulations reveals higher B values in COMSOL. This discrepancy could be attributed to the employed micro-coils geometry, boundary conditions or skin depth effects in these two platforms.

To conduct a comprehensive investigation of micro-coil behaviour under higher currents and frequencies compared to previous studies, simulations were performed across a broad range of frequencies (5 Hz to 100 kHz) and currents (1 A to 5 A). The B-field, visualised through streamlines, confirms its strongest concentration at the centre of each coil, aligning with prior observations, reached its maximum when the same current direction was applied (confirmed by both visualisations and measurements) and became weakest when opposing current directions were used. Furthermore, the magnetic field strength calculations at various locations around the coils, demonstrated that the B-field strength was increased with increasing current (1 A to 5 A) at all measured positions. The strongest B-field on the surface

of the coil at position (1) (x = 3014 μm, y = 4138 μm, z = 0), ranged from 8.41 to 42.05 mT for all currents and frequencies, regardless of current direction. However, a significant dependence of B-field strength above the coil surface was revealed at position 4 on the current direction, where (i) using the same current input resulted in a weak increase with increasing current from 0.31 mT to 1.56 mT, (ii) using the inverse current input yielded a stronger B-field, increasing significantly with current from 2.04 mT to 10.18 mT by employing currents equal to 1 A and 5 A, respectively. Additionally, the simulations suggest that this magnetic neurostimulation approach can potentially reach depths of up to 2 cm. These simulations provide valuable insights into the influence of current and frequency on the B-field generated by micro-coils. The findings highlight the importance of both current magnitude and direction in optimising magnetic field strength for specific applications.

This chapter also emphasised the importance of considering heat generation alongside B-field strength when designing coils for magnetic neurostimulation applications. Excessive heat can negatively impact coil lifespan, patient safety, comfort, and compliance. Using COMSOL Multiphysics software to assess heat generation across the micro-coils for various applied frequencies and currents, it has been shown that regardless of the specific measurement location on the coil surface, temperature increased proportionately with increasing current (ranging from 30.42 °C to 165.38 °C for currents ranging from 1 A to 5 A across all tested frequencies).

In conclusion, these findings highlight the need for careful consideration of both B-field generation and heat dissipation in the design of micro-coils for safe and comfortable magnetic neurostimulation applications.

4 Micro-coils manufacturing

4.1 Backgrounds and Aims

As aforementioned, next-generation magnetic neurostimulation demands high spatial and temporal selectivity. Achieving this objective for nano-invasive methods requires optimising coils for neuromodulation with enhanced spatiotemporal resolution. Coils for this application can be fabricated using microfabrication techniques [196]. Therefore, miniaturisation of stimulating coils through microfabrication technologies is crucial for meeting these goals. While established microfabrication techniques like through-silicon vias, surface micromachining, lithography, direct writing, and 3D printing have been used for micro-coil fabrication [154, 197-201]. This study presents the novel implementation of electroplating and laser cutting for micro-coils fabrication.

Through the current work, three distinct substrates were explored for the fabrication of micro-coils. The first method involved a two-step process: a thick gold layer was deposited onto a polyimide substrate using physical vapor deposition and electroplating methods, followed by precise laser cutting to define the coil geometry. Alternatively, commercially available multilayer substrates (i.e., substrate type 1 consists of a polyimide substrate with a copper coating, topped with a polyimide film over the copper layer; substrate type 2 comprises an FR-4 substrate with a copper film) were directly laser-cut for rapid prototyping. The influence of electroplating current on the homogeneity of deposited films was investigated by conducting the process at two distinct current densities: 30 mA and 100 mA. To precisely cut through the deposited metal layers on the polymeric substrates and create the desired space between micro-coils, the laser cutting was conducted in different laser powers range from 2.5 W to 2.7 W. The uniformity of the electroplated film across the polymeric substrate and the depth of the laser cuts through the metal layer were analysed with a stylus profilometer to ensure complete removal. The quality of the laser-cut micro-coils was further scrutinised using both optical and scanning electron microscopes. An LCR meter was employed to measure electrical properties, including the impedance, inductance, phase angle, and resistivity of the fabricated micro-coils. To fully characterise the fabricated micro-coils, their magnetic properties evaluations will be conducted using a Tunnel Magnetoresistance (TMR) sensor, followed by comparison of the obtained results with previously generated simulation data. This study pioneers the use of laser cutting for micro-coils fabrication, revealing how carefully chosen parameters influence the resulting coils'

characteristics, and paving the way for future optimisation based on specific application requirements.

4.2 Methods and materials

4.2.1 Printed circuit board design

To precisely position each coil and enable individual control over them when multiple micro-coils were assembled for experimental studies a custom printed circuit board (PCB) was designed in Altium Designer (v.24) for circular micro-coils.

4.2.2 Circuit design

A circuit was designed in LTspice® (v. 24.0.9) to handle both AC and DC currents, leveraging metal–oxide–semiconductor field-effect transistors (MOSFETs) with a current mirror configuration. The system employs a current mirror circuit composed of scaled-up (10x) MOSFETs to deliver controlled current to the coils. The power supply provides the necessary energy for this operation. Additionally, individual coil control is facilitated by incorporating switches into the design.

4.2.3 Micro-coils manufacturing

Two distinct approaches were employed to fabricate the designed micro-coils. Initially, a multistep cleanroom fabrication method was utilised to produce a gold coated flexible substrate. This step aimed to achieve a gold film onto the surface of polyimide substrates using electroplating method. A multistep process was employed, encompassing (i) a seed layer deposition, and (ii) electroplating. The initial step involved depositing a thin layer of Ni-Cr and gold onto the polyimide surface to enhance adhesion and facilitate subsequent thick film gold deposition. The core step involved immersing the substrate with the seed layer in an electrolyte solution containing gold ions. By applying an electric current, gold ions were attracted and reduced onto the surface, forming the desired film.

Additionally, a laser cutting machine was employed to fabricate micro-coils using the gold coated substrate and two more commercially available substrates. Details of each method is given briefly through this section.

4.2.3.1 Electron-beam evaporation

To deposit the seed layer, an electron-beam evaporator (Plassys, MEB550S) was used. Briefly, electron beam evaporation utilises a focused beam of high-energy electrons to directly heat and vaporise the source material. Heated filaments emit electrons (thermionic emission) that, when accelerated, gain enough energy to vaporise various materials. This vapor then travels across the vacuum and deposits onto a substrate, creating a thin film [202]. The thickness of the deposited film is continuously monitored *in-situ* using a quartz crystal. This technique has a deposition rate of 0.1 - 100 µm/min with capability to keep substrate temperatures low [202, 203]. This technique measures changes in the crystal's resonant frequency, which are directly related to the mass and, consequently, the thickness of the deposited material [204].

In the case of the present study, the source materials were Ni-Cr and gold. The deposition process took place in a highly controlled environment within the chamber. Powerful pumps created a high vacuum of 10^{-5} Torr or lower, minimising the presence of gas molecules that could interfere with the film deposition. Prior to seed layer deposition, a 75 µm thick polyimide film (Kapton, USA) was cut in the dimension of 2 cm x 2 cm and cleaned with acetone (Sigma-Aldrich) to remove surface contaminants, followed by air drying using pressurised air. Finally, the cleaned substrate was attached to a 4-inch silicon wafer using polyimide tape for the subsequent seed layer deposition process. The first step involved depositing a 20 µm thick Ni-Cr layer. Subsequently, a 70 nm layer of Au-Au was deposited on top. Fig. 4-1 shows a schematic diagram of the evaporation process.

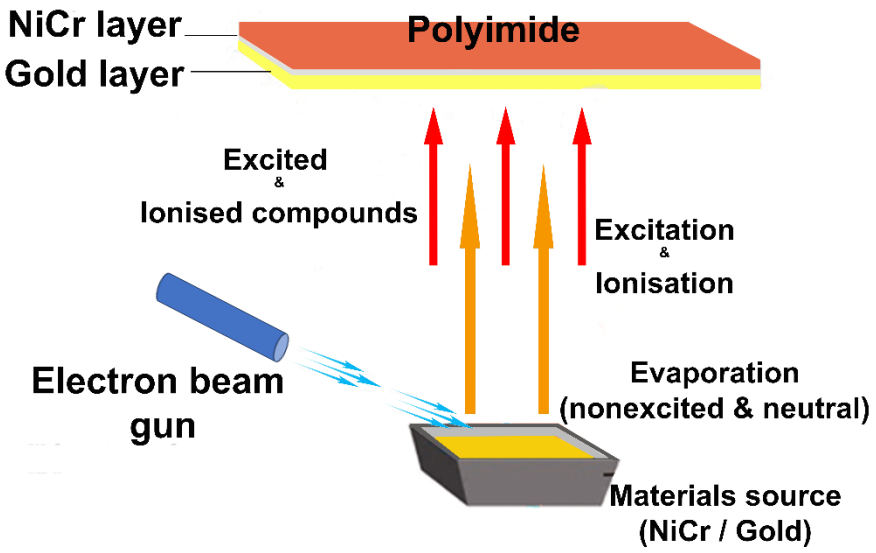

Fig. 4-1: The schematic illustration of the employed electron-beam evaporation to deposit NiCr and gold seed layers

4.2.3.2 Electroplating

Electroplating various objects with different metals requires immersing them in a metal salt solution, using a metal with a strong electrical potential [205]. During this process, an electric current, drives chemical reactions at the surface of a metallic object immersed in the salt solution. At the cathode (negative electrode), metal ions from the solution gain electrons and are deposited onto the object's surface. This reduction process can involve either the removal of oxygen or the addition of hydrogen, depending on the specific electrolyte and operating conditions [205].

In this study, a 24k Gold Plating Solution (8 g/l, Gold Solutions Plating, Kent, UK) served as the source of metal ions. The polyimide substrate with seed layers functioned as the cathode, while platinum was employed as the anode. The electroplating was carried out in a beaker with continuous mechanical agitation (100 rpm; IKA® RW 20, USA) to ensure uniform mixing and mass transfer of ions. Additionally, the entire setup was placed in an ultrasonic bath (Haake, 003-2702, Germany), utilising sound waves to further promote agitation and improve the quality of the deposited metal layer. To optimise the electroplating process and understand the influence of key parameters, experiments were conducted at a controlled temperature of 50°C. Different combinations of time intervals (2 hours) and current densities of 30 to 100 mA were explored while maintaining a constant voltage of 2 V. This systematic approach allows for analysing the individual and combined effects of these factors on the resulting electroplated layer. The schematic of the electroplating process is shown in Fig. 4-2.

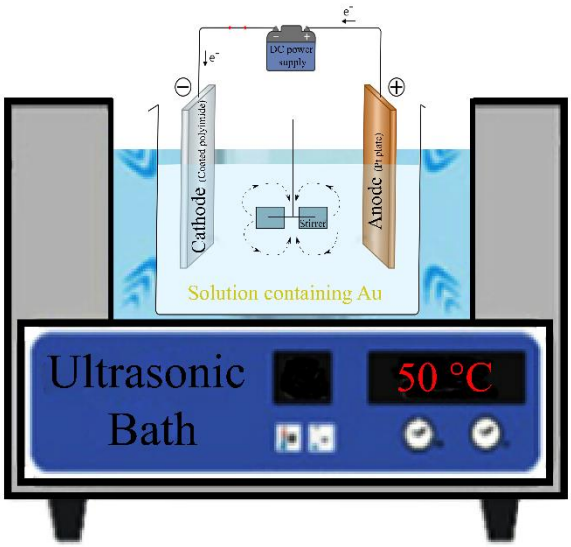

Fig. 4-2: The schematic illustration of the electroplating setup to deposit a gold film on a polyimide substrate

As part of the post-processing steps, the electroplated samples were subjected to thermal annealing within a nitrogen environment at 200°C for 1 hour using a laboratory oven (Carbolite-Gero PF, UK). Subsequently, the temperature was gradually reduced to 50°C to control the cooling rate and mitigate potential thermal strain, minimise thermal stresses and promote structural stability.

4.2.4 Laser cutting machine

Laser cutting enables the fabrication of micro-coils with high precision via a tightly focused laser beam, which selectively removes material layer-by-layer, resulting in microstructures. The small beam diameter (< 1μm) ensures superior resolution compared to conventional machining techniques [206-210]. The precise control offered by the laser minimises cutting edge gaps between micro-coil components. Laser-based fabrication relies on photothermal ablation, where the focused laser beam induces localised heating and vaporisation of the target material. The generated vapor and particulates are effectively removed through an exhaust system, mitigating potential contamination and environmental concerns. Furthermore, the non-contact nature of this process eliminates mechanical stress transmission, preserving the integrity of delicate microstructures [206-209]. The schematic of a laser cutting machine is shown in Fig. 4-3. Micro-coils were fabricated from electroplated substrates as well as two commercially sourced substrates (FPCway HQ, China). Substrate type 1 consists of a polyimide substrate with a copper coating, topped with a polyimide film over the copper layer. Substrate type 2 comprises an FR-4 substrate with a copper film. Additional details of substrates can be found in Fig. 4-4.

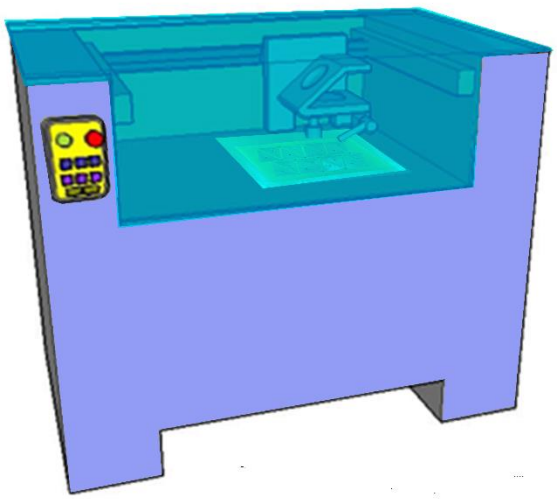

Fig. 4-3: The schematic of a laser cutting process employed to fabricate micro-coils

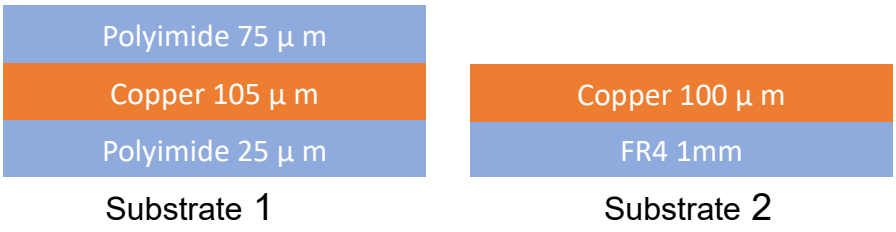

Fig. 4-4: Details of employed substrates for micro-coils fabrication; substrate 1: A polyimide base with a deposited copper layer, further protected by a polyimide film. Substrate 2: An FR-4 substrate incorporating a copper film

The coils were manufactured utilising an LPKF ProtoLaser R4 (LPKF Laser & Electronics, SD-25G, Germany) which operated at a laser wavelength of 515 nm, a pulse frequency of 25 kHz, a pulse length of 1.5 ps, a repetition of 18, and a power range of 2.5-2.7 W.

4.2.5 Characterisation methods

This section details the characterisation and analysis techniques used for both the prepared substrates and micro-coils.

To determine the thickness and surface roughness of the fabricated micro-coils and their corresponding substrates, a DektakXT Stylus Profilometer (Bruker, CN10092728, UK) was employed. The instrument operates in contact mode, scanning laterally with the stylus that measures minute deflections for precise profile reconstruction. This instrument utilises a fine stylus tip with a radius of 2 µm and can detect vertical height variations as small as 0.01 nm, offering highly accurate measurements.

To study complete detachment (hatching) of micro-coils from the substrate by the laser machine. The topography of the fabricated micro-coils was examined using an optical microscope (Nikon Eclipse LV150, Japan) equipped with a Nikon Fi_2 camera and NIS Elements 4.5 software. Furthermore, to gain deeper insights into the laser cutting process quality, a scanning electron microscopy (SEM) analysis (FEI Nova NanoSem 630, USA) was conducted. Apart from the standard secondary electron detectors, this SEM boasts a HELIX detector, optimal for low-vacuum imaging of insulating samples, and a high contrast low voltage detector, a high-contrast backscatter detector capable of generating high-resolution backscattered images.

To characterise the electrical properties of the fabricated micro-coils, an LCR meter (Keysight, E4980AL, UK) was employed. Measurements of inductance, resistance, phase

angle, and capacitance were conducted across a frequency range spanning 10 kHz to 100 kHz.

4.3 Results and discussions

This section presents the results of experimental works. It begins by detailing the PCB and circuit designs. Next, the section covers the fabrication and optimisation of micro-coils, along with their performance evaluation, including discussions and correlations between the computational and experimental data. Finally, the section concludes with the best-achieved optimisation results.

4.3.1 PCB and circuit designs

To precisely position and individually control multiple circular micro-coils in experiments, a custom PCB was designed. Fig. 4-5 shows this PCB populated with micro-coils.

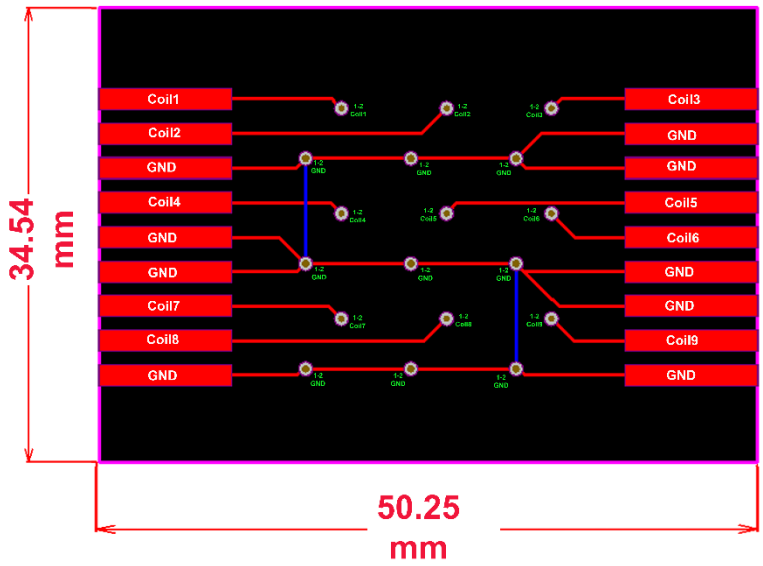

Fig. 4-5: The designed PCB for circular micro-coils

Fig. 4-6 presents the circuit design for a set of two micro-coils, operating with both AC and DC currents. Each coil features a programmable stimulation site controlled by a dedicated switch. To achieve a higher coil current, the design incorporates a current mirror circuit using MOSFETs (scaled-up 10x).

Fig. 4-7 illustrates the proposed circuit in operation, with graphs demonstrating individual

current control for each of the two micro-coils. Separate switches allow independent control of each coil.

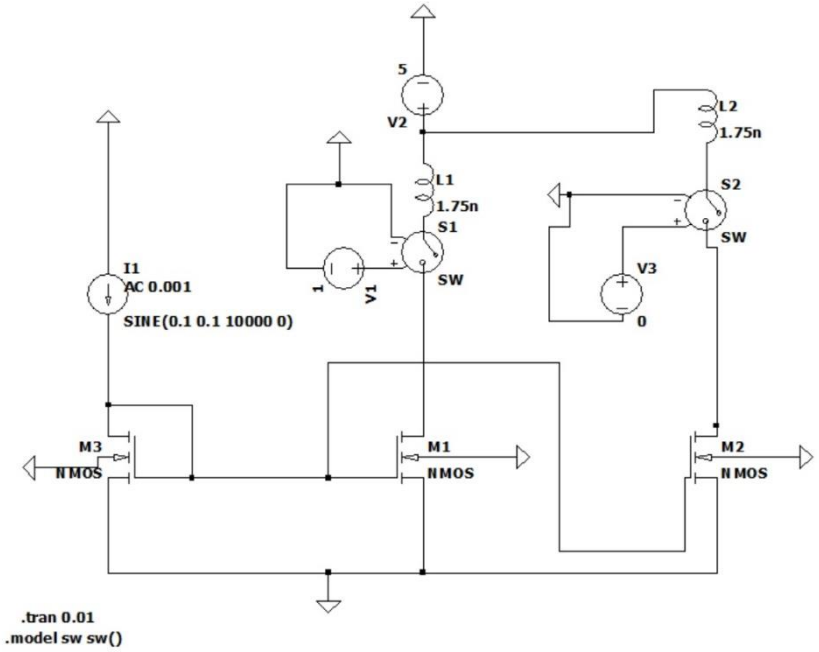

Fig. 4-6: Layout of the proposed circuit design with two micro-coils for neurostimulation

By employing MOSFETs (10x) within a custom-designed current mirror, the system efficiently boosts the input current, where both setups achieve a 10-fold current boost, amplifying the 100 mA input to 1 A in the target micro-coil.

4.3.2 Characterisations of fabricated micro-coils

The micro-coils fabrication was started with gold electroplating on a 2 cm x 2 cm polyimide substrate. To start with, the substrate received a 20 µm layer of Ni-Cr, followed by a 70 nm layer of Au-Au as seed layers. Finally, it underwent electroplating with 24k gold solution at a controlled 50°C for two consecutive 2-hour intervals.

During this process, the current density ranged from 30 to 100 mA while maintaining a constant voltage of 2 V. The thin initial seed layer was not strong enough to reliably hold the thicker subsequent electroplated layer. To ensure proper adhesion and prevent peeling, the substrate underwent a thermal annealing process in a nitrogen environment at 200°C for 1 hour. Annealing the substrate at the optimal temperature improves its adhesion, as verified using the standardized (JIS H8504) tape test [211, 212]. Fig. 4-8 shows the prepared

substrates.

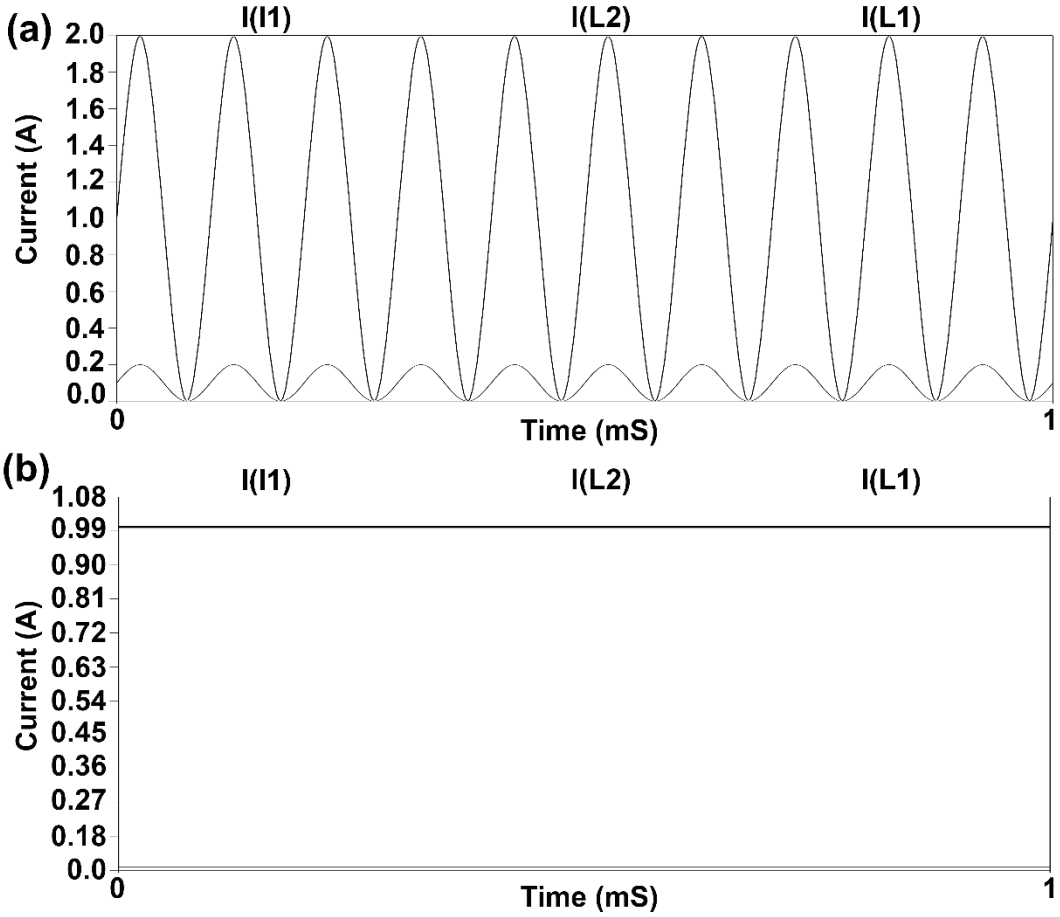

Fig. 4-7: The proposed circuit in operation, both (a) AC and (b) DC setups achieved a 10-fold current boost, amplifying the 100 mA input to 1 A in the target micro-coil

Figure 4-8 reveals the impact of current density on electroplating quality. Initially, after depositing seed layers, the substrate had a smooth, reflective surface. However, applying a low current density (30 mA) led to an uneven coating (indicated by the oval in Fig. 4-8b). This non-uniformity, with areas of detachment or extreme roughness, might be attributed to the formation of a film of the native oxide during the early stages of electroplating [213]. Higher current densities (100 mA) produced uniform electroplated films (Fig. 4-8c), which remained consistent after annealing. Seeking a thicker film, the process was repeated with identical parameters after the first annealing. The repeated 100 mA process (Fig. 4-8d) delivered a thick, uniform layer. After optimising the electroplating conditions, the prepared substrate was laser-cut to create micro-coils on its gold-plated polyimide surface, as shown in Fig. 4-9. However, two challenges were encountered with the electroplated substrates after analysing the electroplated substrate using Dektak surface profilometer as shown in Fig. 4-10.

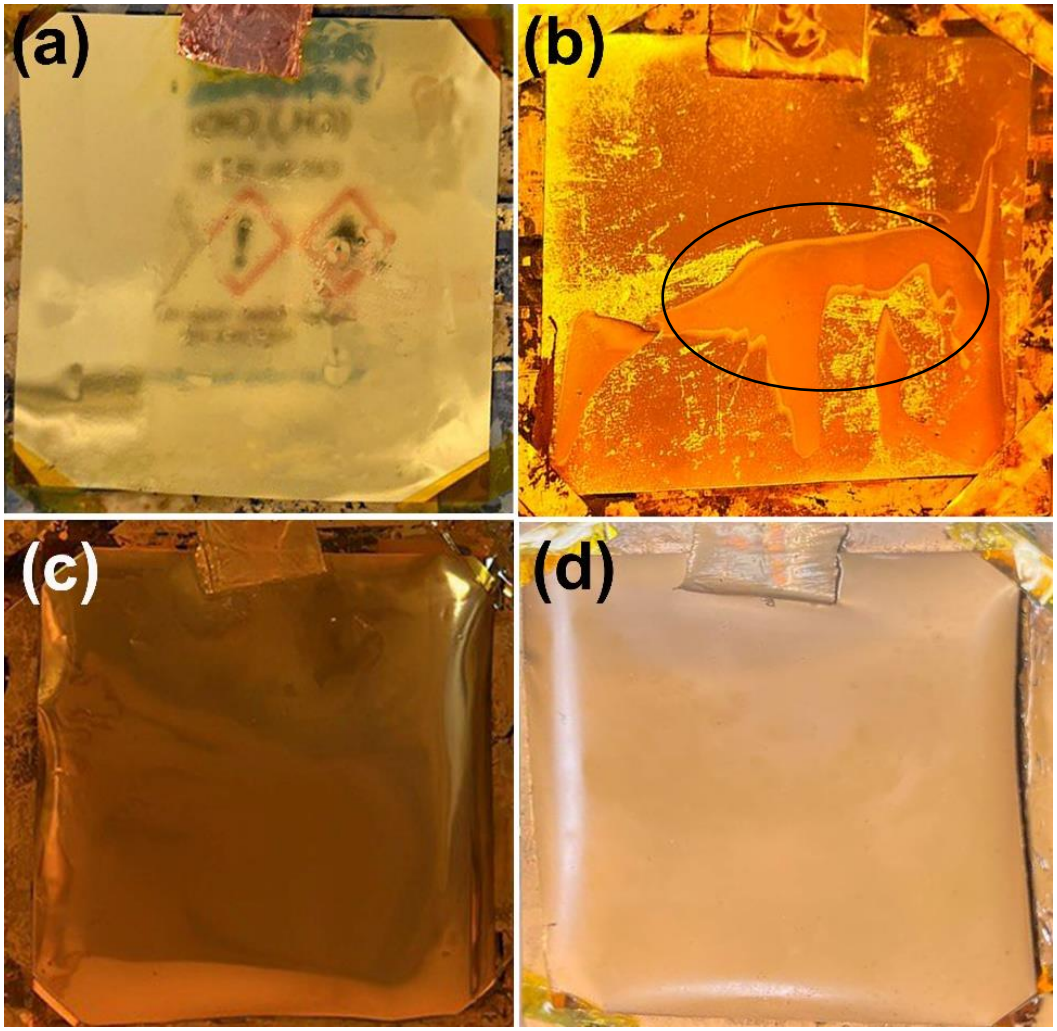

Fig. 4-8: Polyimide substrates prepared through various electroplating and annealing steps; (a) after deposition of seed layers (Ni-Cr and Au-Au), (b) electroplated at 30 mA for 2 hours, (c) electroplated at 100 mA for 2 hours and annealed at 200°C for 1 hour, (d) second electroplating on the substrate (c) at 100 mA for 2 hours and annealed at 200°C for 1 hour

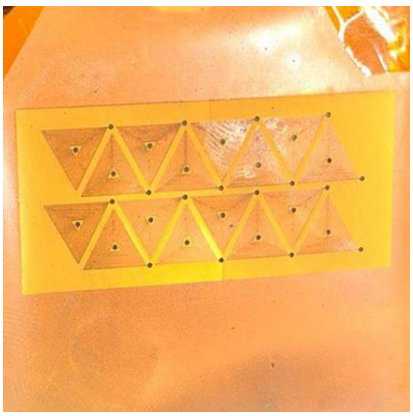

Fig. 4-9: A set of laser-cut micro-coils onto the electroplated polyimide substrate using an LPKF laser machine

Firstly, the electroplated layer was found to be less than 100 μm in thickness, which did not meet the minimum requirement for this study. This could be addressed using longer

electroplating process. Secondly, there was a considerable variation in the thickness of the electroplated layer across the substrate, with a maximum difference of approximately 20 µm between coated layers.

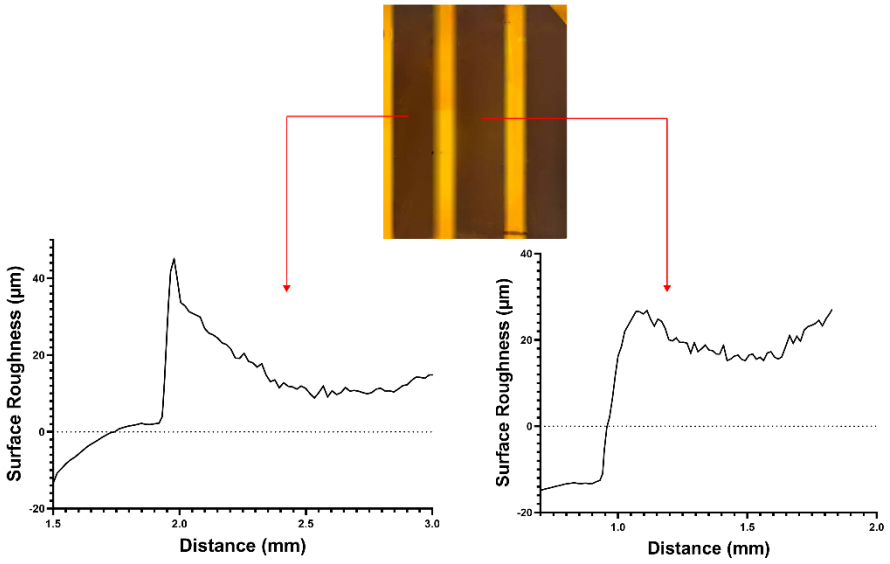

Fig. 4-10: Graphs of surface roughness measurements across the electroplated substrate

It has been reported that the B-field strength of a coil does depend on the current flowing through it and the number of turns in the coil [195]. The conductivity of the wire material has a minor effect on the current than results from a given voltage applied across the coil. This is because the main limitation to the current flow is the resistance of the wire, which is determined by its length, cross-sectional area, and resistivity [214]. While conductivity plays a role in determining resistivity, it is not the only factor, and its influence on the current is usually minor compared to the other factors (e.g., cross-section area, length etc) [214, 215].

This research investigated the use of copper instead of gold for the conductive layer due to two main considerations (i) similar electrical properties; at room temperature (20 °C), both copper and gold exhibit almost similar electrical conductivity and resistivity, where copper possesses slightly better conductivity (5.96×10^7 S/m) and lower resistivity (1.68×10^{-8} Ω·m) compared to gold (4.10×10^7 S/m and 2.44×10^{-8} Ω·m, respectively) [216]. (ii) Manufacturing limitations; the electroplated gold layer on the polyimide substrate displayed inconsistent thickness as shown in Fig. 4-10, hindering precise laser cutting of these layers. Therefore, the study employed two commercially available substrates; (i) Substrate type 1, consists of a polyimide substrate coated with copper and topped with a polyimide film. (ii)Substrate type 2, which comprises an FR-4 substrate with a copper film.

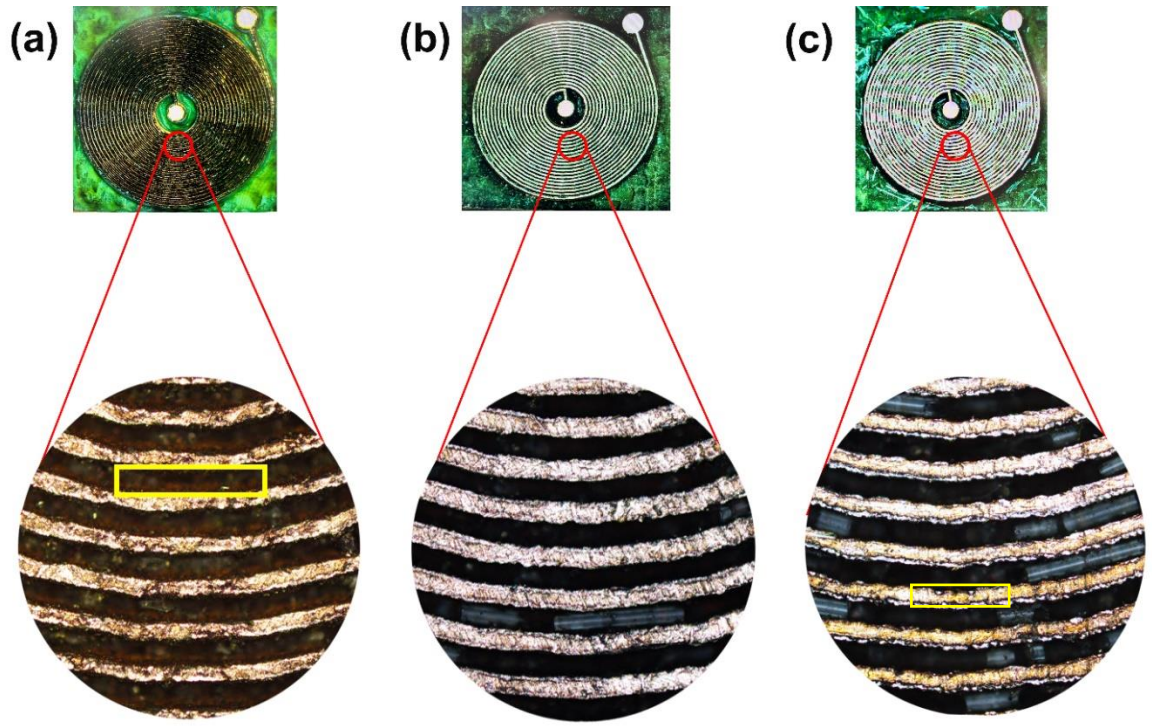

Fig. 4-11: Optical images of fabricated micro-coils using LPKF laser machine on FR-4 substrates at different powers of (a) 2.5 W, (b) 2.6 W, and (c) 2.7 W. (magnification 10X)

Laser parameter optimisation was conducted for fabricating micro-coils on substrate types 1 and 2 using an LPFK laser machine. Three power levels between 2.5 and 2.7 were employed, each paired with a unique pulse setting and a wavelength (section 3.2.4). Visual representations of the resulting micro-coils from each parameter combination are depicted in Fig. 4-11. Fig. 4-11 reveals that lower laser powers (2.5 W) resulted in incomplete copper cutting from the substrate, leaving visible copper traces (marked by boxes) between the micro-coil wires. Conversely, using the higher power settings (2.6 and 2.7 W) achieved complete copper removal from the upper surface of the substrate, eliminating any residual copper and creating clear separation between the coils.

However, the highest power (2.7 W) caused unwanted burning of the wires (marked by a box). Analysis of substrate 1 yielded identical trends as observed in substrate 2, justifying the exclusion of redundant data for clarity and conciseness. To assess the precision of laser cuts under different employed power settings surface roughness measurements were conducted, as shown in Fig. 4-12.

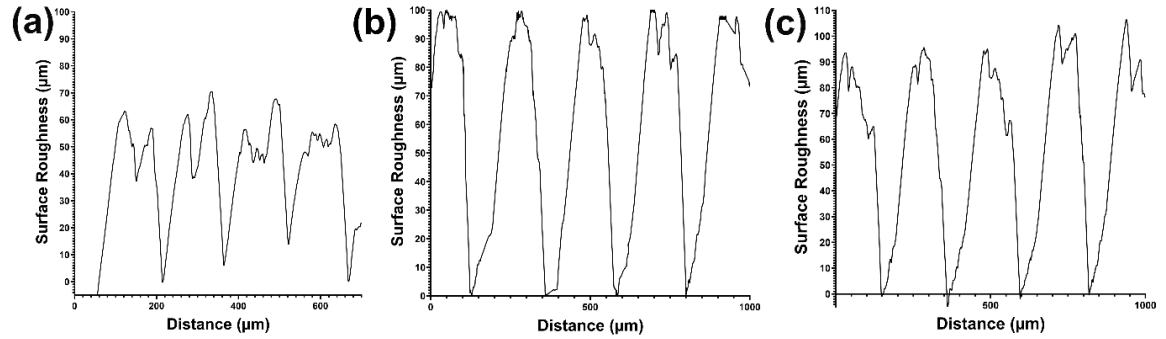

Fig. 4-12: Graphs of surface roughness measurements in micro-coils fabricated at different laser powers of (a) 2.5 W, (b) 2.6 W, and (c) 2.7 W

Fig. 4-12 quantitatively validates the visual observations in Fig. 4-11. It confirms that higher laser power settings (2.6 and 2.7 W) completely remove the copper layer from the substrate's surface. The measured depth matches the known thickness of the copper on the FR-4 substrate, indicating clean separation between the micro-coils with no residual copper remaining. To further investigate and better visualise the quality of the laser cut process using different employed powers SEM analyses were conducted and shown in Fig. 4-13.

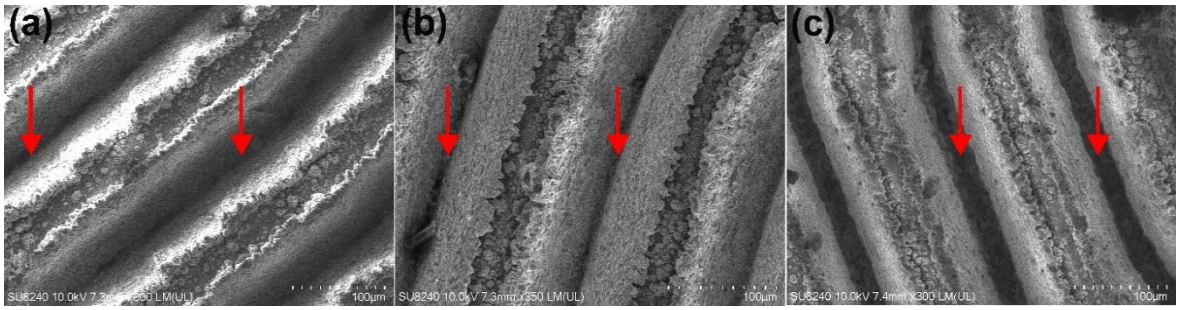

Fig. 4-13: Scanning electron microscope images of fabricated micro-coils at different laser powers (a) 2.5 W, (b) 2.6 W and (c) 2.7 W

Fig. 4-13 demonstrates that the lower laser power (2.5 W) was insufficient to fully cut through the copper and forms areas with narrow spacing between coils (indicated by arrows). Conversely, employing the higher power settings (2.6 W and 2.7 W) successfully removed all copper from the substrate's upper surface, leaving no residue and creating distinct gaps between the coils. Considering Fig. 4-13c, it is clear that wider spaces between the coil wires were created using 2.7 W. These findings align with the observations made in optical microscopy images and roughness measurements.

The electrical characteristics of the fabricated micro-coils were characterised by measuring their impedance, inductance, phase angle, and resistance using an LCR meter across a frequency range of 0 to 550 kHz at 1 V and is shown in Fig. 4-14.

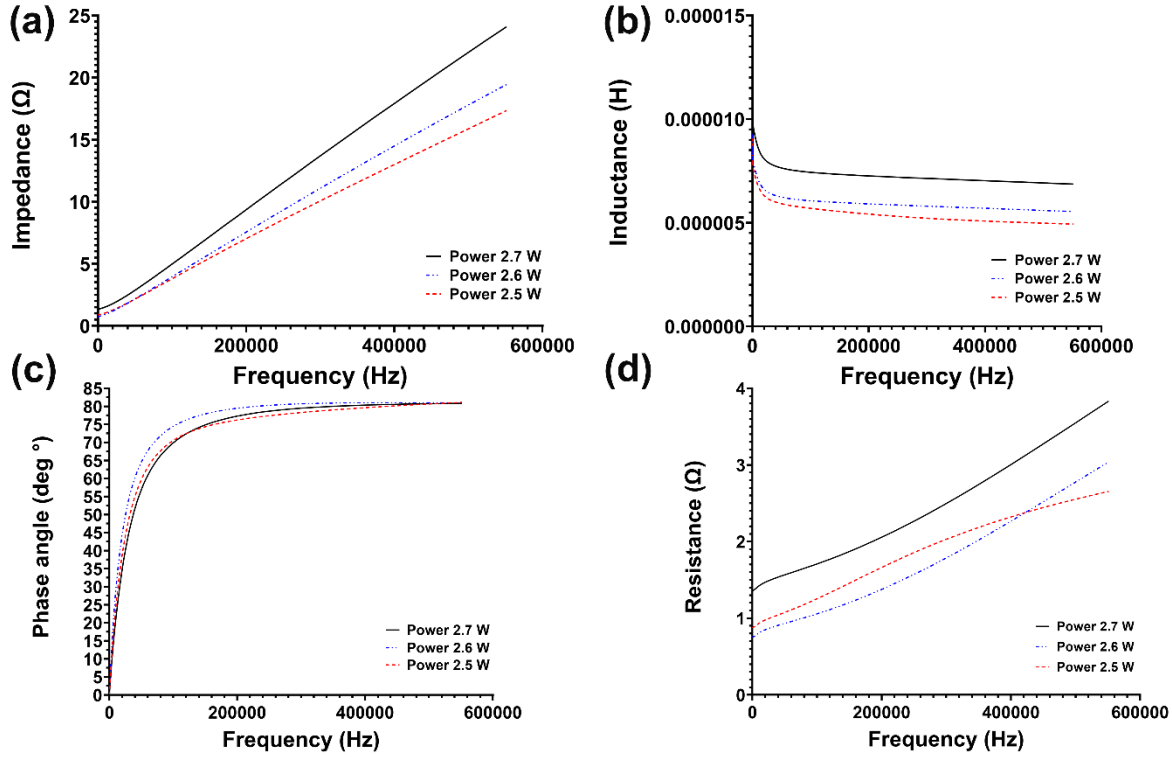

Fig. 4-14: The measured electrical properties of the fabricated micro-coils using three different laser powers (2.5 W, 2.6 W, and 2.7 W); (a) impedance, (b) inductance, 9c) phase angle, and (d) resistance, across a frequency range of 0 to 550 kHz at 1 V

In Fig. 4-14a, graphs show the impedance of micro-coils fabricated using different laser powers increases with increasing frequency for all three laser powers. The rate of increase is slightly different for each power, with the coils fabricated using 2.7 W having the highest impedance at all frequencies. Briefly, the impedance of the micro-coils starts at around 1.36 Ω, 0.76 Ω, and 0.90 Ω at 20 Hz and increases to around 24.10 Ω, 19.44 Ω, and 17.34 Ω at 550 kHz for coils fabricated using 2.7 W, 2.6 W, and 2.5 W, respectively. This behaviour aligns with the inherent characteristic of inductive components like coils, which oppose changes in current flow and their opposition increases with increasing frequency [217-219].

For all three laser powers, the inductance decreases as the frequency increases as shown in Fig. 4-14b. This is because the reactance of the inductor increases with frequency, causing the inductor to oppose the flow of alternating current more effectively at higher frequencies

[217-219]. This is a well-established phenomenon observed in inductors and is described by the inductive reactance equation for a coil:

$$X_L = 2\pi f L \quad \text{4-1)}$$

where, X_L represents the inductive reactance in ohms, π (pi) denotes a mathematical constant approximately equal to 3.14, f signifies the frequency in hertz (Hz), and L represents the inductance in henrys (H) [220]. The inductance appears to be relatively constant across the frequency range, remaining around 5 μH. This suggests that the ability of the micro-coils to store energy in a magnetic field is not significantly affected by the frequency of the applied voltage.

Graphs in Fig. 4-14c show that the phase angles of all three micro-coils increase with increasing frequency. This is a typical characteristic of inductive materials, such as coils [221, 222]. As the frequency of the applied voltage increases, the inductive reactance of the coil increases, which causes the phase angle to increase [222, 223]. The graph confirms that the phase angle of all three micro-coils increases with increasing frequency. While the trend is consistent, the phase angle exhibits minor differences based on the laser power used for fabrications. To be more quantitative, at 550 kHz, the micro-coils manufactured with a laser power of 2.7 W have a phase angle of 80.85°, while the micro-coils manufactured with a laser power of 2.5 W have a phase angle of 81.12°. This is a difference of 0.27° and that the laser power used to fabricate the micro-coils can slightly affect their phase angle. However, the overall trend of the phase angle response is similar for all three laser powers.

As shown in Fig. 4-14d, the resistance increases slightly with increasing frequency for all three powers. The resistance of the micro-coils manufactured with a laser power of 2.7 W is the highest, ranging from 1.36 Ω at 20 Hz to 3.83 Ω at 550 kHz. The resistance of the micro-coils manufactured with a laser power of 2.5 W is in the middle, ranging from 0.89 Ω at 20 Hz to 2.65 Ω at 550 kHz. The resistance of the micro-coils manufactured with a laser power of 2.6 W is the lowest, ranging from 0.76 Ω at 20 Hz to 3.04 Ω at 550 kHz. It is important to note that the difference in resistance between the micro-coils fabricated with different laser powers is relatively small. For example, at 550 kHz, the difference in resistance between the micro-coils fabricated with a laser power of 2.5 W and 2.7 W is only 1.18 Ω.

Overall, the graphs show that the electrical properties of the micro-coils can be controlled by the laser power used to fabricate them. This information is important for the design and development of micro-coils in this study. In summary it can be concluded from the Fig. 4-

14, the impedance of the micro-coils is much larger than their resistance at all frequencies. This indicates that the inductive reactance is much larger than the resistance, and the micro-coils behave predominantly as inductors. Furthermore, the phase angle of the micro-coils is close to 90 degrees at high frequencies, which is another indication that the micro-coils behave predominantly as inductors.

The minimal differences observed in the measured electrical properties between the micro-coils fabricated using different laser powers is likely due to differences in their physical properties. These differences can be attributed to several factors, including (i) variations in geometry; higher laser power led to wider spaces between the micro-coil wires, resulting in a larger cross-sectional area for current flow as it has been shown in Figs. (4-11, 12 &13). This can increase the inductance and consequently, the impedance. (ii) changes in material properties; the laser cutting process can alter the electrical conductivity of the material due to localized heating [224]. Higher laser powers might lead to more significant changes in conductivity, which can also affect the electrical resistivity [224]. The increase in resistance with increasing frequency is likely due to the skin effect. The skin effect is a phenomenon that occurs in conductors at high frequencies. [225, 226]. This can increase the effective resistance of the conductor [227, 228].

It is important to note that the observed differences in electrical characteristics are relatively small across the range of laser powers investigated. Future studies could explore the specific mechanisms by which laser power affects the material properties of micro-coils, leading to these observed changes.

Fig. 4-15 represents the influence of varying frequencies (10 Hz, 10 kHz, and 100 kHz) on the magnetic field strength (B-field density) within manufactured micro-coils. All measurements were conducted with a constant current of 100 mA. The x-axis of the graph represents the radial distance outward from the centre of the coil.

The data underlines a relationship between the B-field and both the applied frequency and the distance from the coil's centre. Overall, at the frequency of 10 Hz the strongest B-field range was observed. The B-field values ranged from a minimum of 429.26 nT at the centre of the coil to a maximum of 1678.01 nT at a distance of 25 mm from the centre. Interestingly, the peak B-field was not located directly at the centre and the highest B-field was 2169.71 nT at 15 mm. Compared to 10 Hz, at 10 kHz a weaker B-field was observed. The range observed is between 296.58 nT and 655.60 nT. Similar to 10 Hz, the peak B-field of 1303.39 nT occurred at 15 mm from the centre, not directly in the middle. The frequency of 100 kHz

produced the weakest B-field among the three. The B-field values ranged from 803.89 nT to 515.11 nT. Notably, the peak B-field of 1084.86 nT was observed at 10 mm from the centre. Increasing the frequency (from 10 Hz to 100 kHz) leads to a general decrease in the overall B-field strength at a constant current. The location of the peak B-field does not necessarily coincide with the centre of the coil and shifted based on the applied frequency.

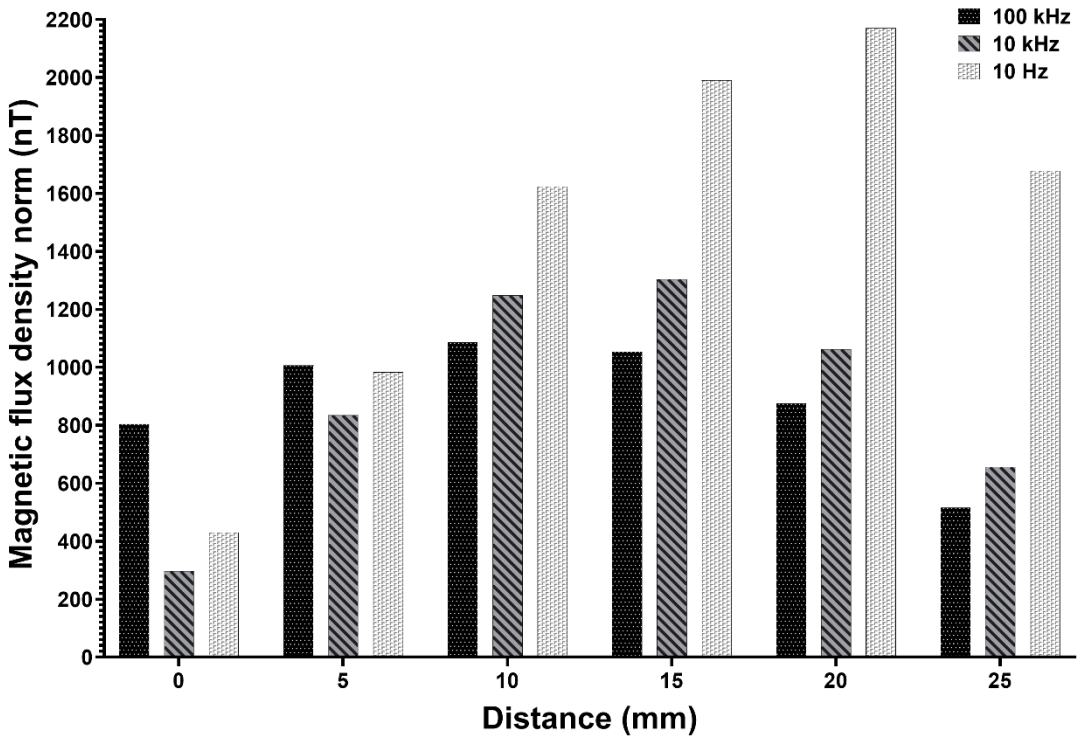

Fig. 4-15: A comparison of the measured magnetic field strength changes across frequencies from 10 Hz to 100 kHz, all measured with a constant current of 100 mA

In this case, the peak B-field tends to move closer to the centre as the frequency increases. Fig. 4-14 demonstrated how the inductive reactance of the coil increases as the frequency rises. Higher reactance, as shown in Fig. 4-14, signifies greater opposition to current flow at higher frequencies. This translates to a decrease in the current flowing through the coil (according to Ohm's Law: V = IR) [164]. Consequently, Fig. 4-15 illustrates a corresponding reduction in the magnetic field strength of the coil as the frequency increases. This aligns with the well-established principle that a weaker current in a coil leads to a weaker magnetic field being generated [90-92]. While simulations predicted the highest B-field to be on the coil's surface, the experimental results in Fig. 4-15 show a different distribution. However, at higher frequency the trend aligns with simulation data. This discrepancy could be attributed to some factors such as sensor sensitivity, environmental interference, 1/f noise, and electromechanical noise. The B-field sensor used in the experiment might not be

sensitive enough to accurately capture the strongest field at the coil's surface. A higher-sensitivity sensor could potentially yield results closer to the simulations. External magnetic fields or other environmental factors from the surrounding area could be influencing the measurements. Implementing shielding materials around the micro-coils during experimentation could minimise these external influences and improve the accuracy of the B-field data. By employing a high-sensitivity sensor and incorporating shielding techniques, future experiments could potentially achieve closer agreement between the measured B-field distribution and the simulation predictions.

4.4 Conclusion

In this chapter, the design and fabrication of a micro-coil system capable of independent current control for each micro-coil using AC and DC currents were illustrated. The design utilises MOSFETs within a custom current mirror circuit to achieve a 10-fold current boost, amplifying the input current to 1 A.

The fabrication process of the micro-coils began with gold electroplating on a polyimide substrate, involving the deposition of Ni-Cr and Au-Au seed layers followed by electroplating with 24k gold solution. Control over current density and annealing processes were critical to ensuring uniform and adherent coatings. Despite challenges such as initial non-uniformity and thickness variations across the substrate, optimisation efforts led to the production of consistent electroplated layers. However, challenges persisted, including the need for thicker electroplated layers to meet study requirements, and addressing variations in coating thickness across the substrate. These issues highlight areas for further refinement and optimisation in future fabrication processes.

Furthermore, this chapter explored the feasibility of using copper as a substitute for gold in the fabrication of micro-coils. The investigation was motivated by two key factors (i) similar electrical properties and (ii) manufacturing challenges. Copper offers comparable electrical conductivity to gold, potentially maintaining functionality while reducing costs. Inconsistency in the electroplated gold layer thickness on polyimide substrates hindered precise laser cutting. Therefore, a commercially available prefabricated substrate, constructed with an FR-4 substrate featuring a pre-deposited copper film, was employed: This pre-made substrate provides a more reliable and consistent platform for micro-coil fabrication compared to the previously encountered challenges with electroplating.

Laser parameter optimization was undertaken to fabricate micro-coils on different substrate types using an LPFK laser machine. This involved testing three power levels ranging from 2.5 to 2.7 W, each coupled with specific pulse settings and wavelengths. Results revealed that the lower laser power (2.5 W) resulted in incomplete copper removal, leaving unwanted traces between the micro-coil wires (confirmed through surface roughness measurements and visually by optical and SEM analyses). Higher laser power settings (2.6 W and 2.7 W) achieved complete copper removal, creating clean separation between the coils. However, the highest power setting (2.7 W) caused minor burning of the wires. Laser cutting power of 2.6 W effectively removed the copper layer while minimising damage to the micro-coils.

The electrical properties of micro-coils fabricated using different laser cutting power levels were also investigated. Measurements of impedance, inductance, phase angle, and resistance were conducted across a frequency range of 0 to 550 kHz using an LCR meter showed that the impedance increased with frequency for all power levels, with coils fabricated at 2.7 W exhibiting the highest values. This aligns with the expected behaviour of inductive components. The inductance remained relatively constant across the frequency range at around 5 μH, indicating the ability of the micro-coils to store energy in a magnetic field is not significantly affected by the frequency of the applied voltage. Phase angles increased with frequency for all coils, demonstrating their inductive nature. Minor differences in phase angle were observed between different power levels (e.g., 0.27° at 550 kHz). The resistance increased slightly with frequency for all coils. While the power level affected the overall resistance values, the differences were relatively small (e.g., 1.18 Ω at 550 kHz between 2.7 W and 2.5 W coils).

Furthermore, the influence of varying frequencies (10 Hz, 10 kHz, and 100 kHz) on the magnetic field strength within manufactured micro-coils were measured with a constant current of 100 mA. The results indicate that the magnetic field (B-field) exhibited variability, ranging from 429.26 nT at the coil's centre to 1678.01 nT at a distance of 25 mm from the centre for a frequency of 10 Hz. The maximum recorded B-field intensity reached 2169.71 nT at a distance of 15 mm from the coil centre. For a frequency of 10 kHz, the B-field ranged between 296.58 and 655.60 nT, peaking at 1303.39 nT at a distance of 15 mm. At 100 kHz, the B-field spanned from 803.89 to 515.11 nT, with the highest intensity recorded at 1084.86 nT, located 10 mm away from the coil's centre. In summary, the optimal laser cutting power was identified as 2.6 W and the results demonstrate that the electrical properties of these micro-coils can be influenced by the laser power used during fabrication. Notably, the impedance values were significantly higher than the resistance across all frequencies,

indicating that the micro-coils primarily behave as inductors.

5 Conclusion and future works

In this chapter, the key insights gained from both computational and experimental studies throughout this thesis were summarised. Then potential future research directions to advance the field were discussed. The initial findings are promising and suggest further exploration through *in vitro*, and *in vivo* studies. Finally, the steps necessary to translate these findings into practical applications were outlined.

5.1 Conclusions

Neurostimulation techniques play a critical role in both advancing neuroscience research and developing treatments for neurological disorders. Among these techniques, magnetic neurostimulation offers distinct advantages compared to conventional methods like electrical stimulation. While magnetic neurostimulation offers improved selectivity in targeting brain regions due to its non-invasive nature, achieving high spatial resolution, particularly in the depth of the brain, remains a significant challenge for precise stimulation of sub-regions.

The current research involved designing a spiral circular micro-coil and incorporating it into a system with two such coils for computational studies using two EM modelling software Sim4Life and COMSOL Multiphysics. To simulate the DBS system, a human head model was constructed, representing it as a conductive medium. The micro-coils were positioned on the skull's surface. Additionally, simulations were conducted in free space. The magnetic fields generated by the system were analysed with a current of 100 mA at frequencies between 1 and 3 kHz and a wider range of currents (1 mA to 5 A) and frequencies (5 Hz to 100 kHz). In addition, COMSOL Multiphysics was used to perform heat transfer simulations.

Besides computational studies, the research also involved experimental work to explore the fabrication of micro-coils using different substrate materials and fabrication methods. The first fabrication method employed a two-step process. Initially, a gold layer was deposited on a polyimide substrate using electroplating. Two current levels were tested: 30 mA and 100 mA. Subsequently, precise laser cutting defined the desired coil geometry. Alternatively, for rapid prototyping, commercially available multilayer substrates, consisting of a copper-coated FR-4 base, were directly laser-cut. To achieve precise cuts through the metal layers on the polymer substrates and create the intended spacing between micro-coils, laser cutting was employed with varying laser power levels ranging from 2.5 W to 2.7 W. A stylus

profilometer was used to assess the evenness of the electroplated film and the depth of the laser cuts. Optical and scanning electron microscopy were employed to examine the quality of the laser-cut micro-coils. The electrical (impedance, inductance, phase angle, and resistivity) and magnetic properties of the fabricated micro-coils were also measured.

Simulations revealed that the self-inductance of the coils remained relatively unaffected by the chosen frequencies. These frequencies closely matched the quasi-static solution, resulting in improved design stability – a crucial factor for neurostimulation applications. The simulations further highlighted a dual dependence of the B-field strength: it's strongest near the centre of each coil, and it's maximised between the coils when currents flow in the same direction. Both distance from the centre and opposing current directions lead to a decrease in B-field strength. The study found that using frequencies between 1 and 3 kHz and a stimulation current of 100 mA resulted in average magnetic field values ranging from 0.1 to 0.8 mT. The calculated B-field strength at position (1; x = 3014 µm, y = 4138 µm, z = 0) ranged from 8.41 mT to 42.05 mT, regardless of whether the current directions were the same or reverse. At point (x = 8150 µm, y = 4138 µm, z = 0), the B-field with same current inputs ranged from 4.58 mT (1 A) to 22.92 mT (5 A), while reverse current inputs yielded a significantly weaker range of 0.99 mT (1 A) to 4.95 mT (5 A). This trend held true for all tested currents and frequencies. Position 3 (1.99 mm above the surface) showed similar B-field strengths for both current configurations, ranging from 1.44 mT (1 A) to 7.20 mT (5 A). However, position 4 exhibited a dramatic dependence on current direction. With the same current input, the B-field increased modestly, ranging from 0.31 mT (1 A) to 1.56 mT (5 A). Conversely, the reverse current input resulted in a stronger B-field, ranging from 2.04 mT (1 A) to 10.18 mT (5 A). The study successfully achieved its primary goal of generating a magnetic field strength of approximately 10 mT at a depth of 2 cm. This was accomplished at specific positions on the coil's surface by utilising increased input currents. The research observed a temperature rise across the entire coil surface with increasing applied current ranged from 30.42 °C to 165.38 °C for currents between 1 A and 5 A, regardless of the chosen frequency.

The initial data from the experimental phase revealed that the thin seed layer was insufficient to reliably adhere to the thicker layer subsequently deposited through electroplating and this was addressed by a thermal annealing process a multi-step electroplating using higher current densities (100 mA). The electroplating process yielded two primary challenges. First, the deposited layer measured less than 100 µm, falling short of the minimum requirement for this study. Second, the thickness of the electroplated layer exhibited significant variations

across the substrate, with a maximum difference of about 20 µm between different areas making it challenging to cut the substrate using the laser machine. To address the challenges of achieving the desired micro-coil thickness and uniformity with electroplating, laser parameter optimisation was conducted for fabrication of micro-coils using FR-4 substrates with copper cladding. The experiment revealed that lower laser powers (2.5 W) were insufficient to completely cut through the copper layer on the substrate. In contrast, employing higher power settings (2.6 and 2.7 W) achieved complete removal of the copper from the substrate's upper surface, eliminating any leftover copper and ensuring clear separation between the coils. The application of the highest power setting (2.7 W) led to unintended burning of the wires. The conducted LCR measurements across a frequency range of 0 to 550 kHz at 1 V revealed that the impedance values started at around 1.36 Ω, 0.76 Ω, and 0.90 Ω at 20 Hz, respectively, and increased to approximately 24.10 Ω, 19.44 Ω, and 17.34 Ω at 550 kHz for coils fabricated at 2.7 W, 2.6 W, and 2.5 W, respectively. Across all three laser power settings, the inductance values exhibited a decreasing trend with increasing frequency. Conversely, the phase angles for all micro-coils demonstrated a consistent rise with frequency, ultimately reaching around 80° regardless of the laser power used in fabrication. Additionally, the resistance values displayed a slight upward trend with increasing frequency for all power settings. This observation is consistent with the well-known behaviour of inductive components, such as coils [217-219, 221, 222]. In light of all the collected data, micro-coils fabricated using a laser power of 2.6 W emerged as the optimal choice for further development. Evaluations of the influence of varying frequencies (10 Hz, 10 kHz, and 100 kHz) on the magnetic field strength (B-field density) within fabricated micro-coils at a constant current of 100 mA revealed that the B-field strength within the micro-coils was dependent on the applied frequency. The strongest B-field range (429.26 nT to 1678.01 nT) was observed at the lowest frequency of 10 Hz. Compared to 10 Hz, both 10 kHz and 100 kHz resulted in weaker B-field values. At 10 kHz, the B-field ranged from 296.58 nT to 655.60 nT, and at 100 kHz, it further decreased to a range of 803.89 nT to 515.11 nT. As shown already, the resistance of coils increased with rising frequency. This rise in resistance signifies greater opposition to current flow at higher frequencies. Consequently, the current flowing through the coil decreases. This translates to a corresponding reduction in the magnetic field strength of the coil as the frequency increases. This aligns perfectly with the well-known principle that a weaker current in a coil leads to a generation of a weaker magnetic field [90-92, 164]. This choice of parameters for magnetic fields measurements stemmed from the limitations of the available experimental setups, as the available power supply could only generate a maximum current of 100 mA. Therefore,

the study's initial goal of producing a magnetic field strength of around 10 mT at a 2 cm depth was not met. Further investigation using higher current inputs is necessary to achieve the desired field strength. However, this research is demonstrating the application of laser cutting for micro-coil fabrication. It highlights the significant influence of carefully selected parameters on the final characteristics of the coils and paves the way for future optimisation tailored to specific application needs.

5.2 Future research directions

In the current work, analysis of the COMSOL results suggests minimal variation in response across the employed frequencies. This could be attributed to residual errors arising from the frequency domain iterative solver employed in the simulation [191-194]. For improved computational accuracy, it is recommended to utilise direct solvers and refine the mesh at the boundaries. This refinement will enable a more precise capture of the skin depth effect, a crucial factor in electromagnetic simulations. Popular choices include the FDTD and DIE approaches [229-231]. Besides this, analysing spiral micro-coils, featuring various designs (i.e., triangular, rectangular, and pentagon) will be helpful in reaching a conclusion on most proper designs for DBS neurostimulation applications.

Beyond maximising the B-field, designing optimal coils for magnetic neurostimulation necessitates balancing this goal with minimising heat generation within and around the coils [135]. Therefore, evaluating temperature gradients using both computational modelling and experimental measurements is crucial for optimising coil designs. This combined approach will ensure compliance with established medical safety guidelines regarding heat generation during magnetic neurostimulation [232].

Various actuation methods need to undergo *in vitro* testing in neuronal cells using electrophysiology and calcium imaging. Actuation-induced and spontaneous activity at the network-level needs to be examined in primary cells. Following the biocompatibility confirmation in both *in vitro* and *in vivo* settings, the system needs undergo testing as a therapeutic approach for treating for instance a fragile X syndrome mouse model. The therapeutic effectiveness will be determined by examining alterations in the animal behaviour (e.g., social novelty preference, and social approach) [233-236].

6 References

1. Liu, Q., et al., *Changes in the global burden of depression from 1990 to 2017: Findings from the Global Burden of Disease study.* Journal of Psychiatric Research, 2020. **126**: p. 134-140.
2. Miguel, N., et al., *Neuropsychological functioning of patients with major depression or bipolar disorder comorbid to substance use disorders: A systematic review.* European Neuropsychopharmacology, 2023. **75**: p. 41-58.
3. Chong, H.Y., et al., *Global economic burden of schizophrenia: a systematic review.* Neuropsychiatric Disease and Treatment, 2016. **12**(null): p. 357-373.
4. Vigo, D.V., et al., *Disease burden and government spending on mental, neurological, and substance use disorders, and self-harm: cross-sectional, ecological study of health system response in the Americas.* The Lancet Public Health, 2019. **4**(2): p. e89-e96.
5. A. John Rush , M.D., et al., *Acute and Longer-Term Outcomes in Depressed Outpatients Requiring One or Several Treatment Steps: A STAR*D Report.* American Journal of Psychiatry, 2006. **163**(11): p. 1905-1917.
6. O'Shea, M., *The brain: Milestones of neuroscience.* New Scientist, 2013. **218**(2911): p. ii-iii.
7. Finger, S., *Origins of neuroscience: a history of explorations into brain function*. 2001: Oxford University Press.
8. Finger, S., *Minds behind the brain: A history of the pioneers and their discoveries*. 2000: Oxford University Press.
9. Price, C.J., *The anatomy of language: contributions from functional neuroimaging.* Journal of Anatomy, 2000. **197**(3): p. 335-359.
10. Wiesendanger, M., *Eccles' perspective of the forebrain, its role in skilled movements, and the mind–brain problem.* Progress in Neurobiology, 2006. **78**(3): p. 304-321.
11. Houghton, G., *Introduction to connectionist models in cognitive psychology: Basic structures, processes, and algorithms*, in *Connectionist models in cognitive psychology*. 2004, Psychology Press. p. 11-19.
12. Alexander, G.E., M.R. DeLong, and P.L. Strick, *Parallel organization of functionally segregated circuits linking basal ganglia and cortex.* Annual review of neuroscience, 1986. **9**(1): p. 357-381.
13. Benagiano, V., et al., *The functional anatomy of the cerebrocerebellar circuit: A review and new concepts.* Journal of Comparative Neurology, 2018. **526**(5): p. 769-789.
14. Axmacher, N., et al., *Memory formation by neuronal synchronization.* Brain Research Reviews, 2006. **52**(1): p. 170-182.
15. Marom, S. and G. Shahaf, *Development, learning and memory in large random networks of cortical neurons: lessons beyond anatomy.* Quarterly Reviews of Biophysics, 2002. **35**(1): p. 63-87.
16. Jangwan, N.S., et al., *Brain augmentation and neuroscience technologies: current applications, challenges, ethics and future prospects.* Frontiers in Systems Neuroscience, 2022. **16**.
17. Udupa, K. and R. Chen, *The mechanisms of action of deep brain stimulation and ideas for the future development.* Progress in Neurobiology, 2015. **133**: p. 27-49.
18. Odekerken, V.J.J., et al., *GPi vs STN deep brain stimulation for Parkinson disease.* Neurology, 2016. **86**(8): p. 755-761.
19. José Fidel, B.-C., et al., *The safety and efficacy of thalamic deep brain stimulation in essential tremor: 10 years and beyond.* Journal of Neurology,

Neurosurgery & Psychiatry, 2014. **85**(5): p. 567.
20. Boccard, S.G.J., et al., *Targeting the Affective Component of Chronic Pain: A Case Series of Deep Brain Stimulation of the Anterior Cingulate Cortex.* Neurosurgery, 2014. **74**(6): p. 628-637.
21. Fisher, R., et al., *Electrical stimulation of the anterior nucleus of thalamus for treatment of refractory epilepsy.* Epilepsia, 2010. **51**(5): p. 899-908.
22. Fitzgerald, P.B., *Non-pharmacological biological treatment approaches to difficult-to-treat depression.* The Medical Journal of Australia, 2013. **199**(6): p. S48-S51.
23. Greenberg, B.D., et al., *Deep brain stimulation of the ventral internal capsule/ventral striatum for obsessive-compulsive disorder: worldwide experience.* Molecular Psychiatry, 2010. **15**(1): p. 64-79.
24. Oberman, L.M., S.M. Francis, and S.H. Lisanby, *The use of noninvasive brain stimulation techniques in autism spectrum disorder.* Autism Research, 2024. **17**(1): p. 17-26.
25. Perri, R.L., *Alteration of Hypnotic Phenomena and Hypnotizability with Non-Invasive Brain Stimulation (NIBS): State of the Art and Future Perspectives.* The Routledge International Handbook of Clinical Hypnosis, 2024: p. 347-356.
26. Woods, A.J., et al., *A technical guide to tDCS, and related non-invasive brain stimulation tools.* Clinical Neurophysiology, 2016. **127**(2): p. 1031-1048.
27. Airan, R., *Neuromodulation with nanoparticles.* Science, 2017. **357**(6350): p. 465-465.
28. Lozano, A.M., et al., *Deep brain stimulation: current challenges and future directions.* Nature Reviews Neurology, 2019. **15**(3): p. 148-160.
29. Echternacht, S.R., M.A. Chacon, and J.I. Leckenby, *Central versus peripheral nervous system regeneration: is there an exception for cranial nerves?* Regenerative Medicine, 2021. **16**(6): p. 567-579.
30. Zhang, C., M. Qiu, and H. Fu, *Oligodendrocytes in central nervous system diseases: the effect of cytokine regulation.* Neural Regeneration Research, 9900: p. 10.4103/1673-5374.392854.
31. Perea, G., M. Navarrete, and A. Araque, *Tripartite synapses: astrocytes process and control synaptic information.* Trends in Neurosciences, 2009. **32**(8): p. 421-431.
32. Perea, G. and A. Araque, *Glial calcium signaling and neuron–glia communication.* Cell Calcium, 2005. **38**(3): p. 375-382.
33. Monje, M., *Myelin Plasticity and Nervous System Function.* Annual Review of Neuroscience, 2018. **41**(1): p. 61-76.
34. Du, Y. and C.F. Dreyfus, *Oligodendrocytes as providers of growth factors.* Journal of Neuroscience Research, 2002. **68**(6): p. 647-654.
35. Sapir, L. and S. Tzlil, *Talking over the extracellular matrix: How do cells communicate mechanically?* Seminars in Cell & Developmental Biology, 2017. **71**: p. 99-105.
36. Franze, K., P.A. Janmey, and J. Guck, *Mechanics in Neuronal Development and Repair.* Annual Review of Biomedical Engineering, 2013. **15**(1): p. 227-251.
37. Oakland, R., et al., *The biomechanical response of spinal cord tissue to uniaxial loading.* Proceedings of the Institution of Mechanical Engineers, Part H: Journal of Engineering in Medicine, 2006. **220**(4): p. 489-492.
38. Holtzmann, K., et al., *Brain tissue stiffness is a sensitive marker for acidosis.* Journal of Neuroscience Methods, 2016. **271**: p. 50-54.
39. Lovinger, D.M., *Communication networks in the brain: Neurons, receptors,*

neurotransmitters, and alcohol. Alcohol Research & Health, 2008. **31**: p. 196-214.
40. Bath, K.G., et al., *Variant Brain-Derived Neurotrophic Factor (Val66Met) Alters Adult Olfactory Bulb Neurogenesis and Spontaneous Olfactory Discrimination.* The Journal of Neuroscience, 2008. **28**(10): p. 2383-2393.
41. Hull, K.L., *Human Form, Human Function: Essentials of Anatomy & Physiology*. 2011: Lippincott Williams & Wilkins.
42. Bhadra, N., *2 - Physiological principles of electrical stimulation*, in *Implantable Neuroprostheses for Restoring Function*, K. Kilgore, Editor. 2015, Woodhead Publishing. p. 13-43.
43. Krauss, J.K., et al., *Technology of deep brain stimulation: current status and future directions.* Nat Rev Neurol, 2021. **17**(2): p. 75-87.
44. Andersen, T., et al., *7 - Neural stimulation technologies*, in *Principles and Technologies for Electromagnetic Energy Based Therapies*, P. Prakash and G. Srimathveeravalli, Editors. 2022, Academic Press. p. 235-254.
45. Klooster, D.C.W., et al., *Technical aspects of neurostimulation: Focus on equipment, electric field modeling, and stimulation protocols.* Neuroscience & Biobehavioral Reviews, 2016. **65**: p. 113-141.
46. Lin, C.-W., et al., *Implantable pulsed-radiofrequency micro-stimulation system*. 2011, Google Patents.
47. Chan, C.Y. and C. Nicholson, *Modulation by applied electric fields of Purkinje and stellate cell activity in the isolated turtle cerebellum.* The Journal of Physiology, 1986. **371**(1): p. 89-114.
48. Francis, J.T., B.J. Gluckman, and S.J. Schiff, *Sensitivity of Neurons to Weak Electric Fields.* The Journal of Neuroscience, 2003. **23**(19): p. 7255-7261.
49. Chen, I. and F. Lui, *Neuroanatomy, Neuron Action Potential*. 2023: StatPearls Publishing, Treasure Island (FL).
50. Alberts, B., et al., *Ion channels and the electrical properties of membranes*, in *Molecular Biology of the Cell. 4th edition*. 2002, Garland Science.
51. Shafiee, A., et al., *Appropriate Scaffold Selection for CNS Tissue Engineering.* Avicenna J Med Biotechnol, 2020. **12**(4): p. 203-220.
52. Long, S.B., et al., *Atomic structure of a voltage-dependent K+ channel in a lipid membrane-like environment.* Nature, 2007. **450**(7168): p. 376-382.
53. Wang, Y. and L. Guo, *Nanomaterial-enabled neural stimulation.* Frontiers in Neuroscience, 2016. **10**: p. 69.
54. Fletcher, A., *Action potential: generation and propagation.* Anaesthesia & Intensive Care Medicine, 2019. **20**(4): p. 243-247.
55. Jana, S., *Action Potential*, in *Textbook of Veterinary Physiology*, P.K. Das, et al., Editors. 2023, Springer Nature Singapore: Singapore. p. 37-44.
56. Yost, Spencer C., *Potassium Channels : Basic Aspects, Functional Roles, and Medical Significance.* Anesthesiology, 1999. **90**(4): p. 1186-1203.
57. Kueh, D., et al., *Na+/K+ pump interacts with the h-current to control bursting activity in central pattern generator neurons of leeches.* eLife, 2016. **5**: p. e19322.
58. Schwan, H.P., *Electrical Properties of Tissue and Cell Suspensions* *This work was supported in part by grants from the United States Public Health Service, H-1253(c2-4) and in part by the Office of Naval Research, 119–289*, in *Advances in Biological and Medical Physics*, J.H. Lawrence and C.A. Tobias, Editors. 1957, Elsevier. p. 147-209.
59. Schwan, H.P., *Electrical Properties of Cells: Principles, Some Recent Results, and Some Unresolved Problems*, in *The Biophysical Approach to Excitable Systems: A Volume in Honor of Kenneth S. Cole on His 80th*

Birthday, W.J. Adelman and D.E. Goldman, Editors. 1981, Springer US: Boston, MA. p. 3-24.
60. Gordon, T. and A.W. English, *Strategies to promote peripheral nerve regeneration: electrical stimulation and/or exercise.* European Journal of Neuroscience, 2016. **43**(3): p. 336-350.
61. Yang, Y., et al., *Energy dependence on discharge mode of Izhikevich neuron driven by external stimulus under electromagnetic induction.* Cognitive Neurodynamics, 2021. **15**(2): p. 265-277.
62. McIntyre, C.C. and W.M. Grill, *Extracellular stimulation of central neurons: influence of stimulus waveform and frequency on neuronal output.* Journal of neurophysiology, 2002. **88**(4): p. 1592-1604.
63. Ghasemi-Mobarakeh, L., et al., *Application of conductive polymers, scaffolds and electrical stimulation for nerve tissue engineering.* Journal of Tissue Engineering and Regenerative Medicine, 2011. **5**(4): p. e17-e35.
64. Sun, Y., et al., *Enhanced nerve cell proliferation and differentiation on electrically conductive scaffolds embedded with graphene and carbon nanotubes.* Journal of Biomedical Materials Research Part A, 2021. **109**(2): p. 193-206.
65. Qian, Y., et al., *Advances in electrical and magnetic stimulation on nerve regeneration.* Regenerative Medicine, 2019. **14**(10): p. 969-979.
66. Luan, S., et al., *Neuromodulation: present and emerging methods.* Frontiers in Neuroengineering, 2014. **7**.
67. Wells, J., et al., *Application of infrared light for in vivo neural stimulation.* Journal of Biomedical Optics, 2005. **10**(6): p. 064003.
68. Yizhar, O., et al., *Optogenetics in neural systems.* Neuron, 2011. **71**(1): p. 9-34.
69. Aravanis, A.M., et al., *An optical neural interface: in vivo control of rodent motor cortex with integrated fiberoptic and optogenetic technology.* Journal of Neural Engineering, 2007. **4**(3): p. S143.
70. Knöpfel, T., *Genetically encoded optical indicators for the analysis of neuronal circuits.* Nature Reviews Neuroscience, 2012. **13**(10): p. 687-700.
71. Horton, N.G., et al., *In vivo three-photon microscopy of subcortical structures within an intact mouse brain.* Nature Photonics, 2013. **7**(3): p. 205-209.
72. Bystritsky, A. and A.S. Korb, *A Review of Low-Intensity Transcranial Focused Ultrasound for Clinical Applications.* Current Behavioral Neuroscience Reports, 2015. **2**(2): p. 60-66.
73. Legon, W., et al., *Transcranial focused ultrasound modulates the activity of primary somatosensory cortex in humans.* Nature Neuroscience, 2014. **17**(2): p. 322-329.
74. Bottomley, P.A. and E.R. Andrew, *RF magnetic field penetration, phase shift and power dissipation in biological tissue: implications for NMR imaging.* Physics in Medicine & Biology, 1978. **23**(4): p. 630.
75. Young, J., M.-T. Wang, and I. Brezovich, *Frequency/depth-penetration considerations in hyperthermia by magnetically induced currents.* Electronics Letters, 1980. **10**(16): p. 358-359.
76. Hallett, M., *Transcranial Magnetic Stimulation: A Primer.* Neuron, 2007. **55**(2): p. 187-199.
77. Deng, Z.-D., S.H. Lisanby, and A.V. Peterchev, *Electric field depth–focality tradeoff in transcranial magnetic stimulation: Simulation comparison of 50 coil designs.* Brain Stimulation, 2013. **6**(1): p. 1-13.
78. Errico, C., et al., *Ultrafast ultrasound localization microscopy for deep super-resolution vascular imaging.* Nature, 2015. **527**(7579): p. 499-502.

79. Biju, V., et al., *Semiconductor quantum dots and metal nanoparticles: syntheses, optical properties, and biological applications.* Analytical and Bioanalytical Chemistry, 2008. **391**(7): p. 2469-2495.
80. Pankhurst, Q.A., et al., *Progress in applications of magnetic nanoparticles in biomedicine.* Journal of Physics D: Applied Physics, 2009. **42**(22): p. 224001.
81. Guduru, R., et al., *Magneto-electric Nanoparticles to Enable Field-controlled High-Specificity Drug Delivery to Eradicate Ovarian Cancer Cells.* Scientific Reports, 2013. **3**(1): p. 2953.
82. Lugo, K., et al., *Remote switching of cellular activity and cell signaling using light in conjunction with quantum dots.* Biomedical Optics Express, 2012. **3**(3): p. 447-454.
83. Mannix, R.J., et al., *Nanomagnetic actuation of receptor-mediated signal transduction.* Nature Nanotechnology, 2008. **3**(1): p. 36-40.
84. Justesen, D.R. and A.W. Guy, *Arsène jacques d'Arsonval: A brief history.* Bioelectromagnetics, 1985. **6**(2): p. 111-114.
85. Swinton, A.A.C., *Silvanus Phillips Thompson, D.Sc., LL.D., F.R.S. His Life and Letters.* Nature, 1920. **105**(2641): p. 448-449.
86. Geddes, L.A., *d'Arsonval, physician and inventor.* IEEE Engineering in Medicine and Biology Magazine, 1999. **18**(4): p. 118-122.
87. Lee, S.W., et al., *Implantable microcoils for intracortical magnetic stimulation.* Science Advances, 2016. **2**(12): p. e1600889.
88. Salatino, J.W., et al., *Glial responses to implanted electrodes in the brain.* Nature Biomedical Engineering, 2017. **1**(11): p. 862-877.
89. Lee, S.W., K. Thyagarajan, and S.I. Fried, *Micro-Coil Design Influences the Spatial Extent of Responses to Intracortical Magnetic Stimulation.* IEEE Transactions on Biomedical Engineering, 2019. **66**(6): p. 1680-1694.
90. Park, H.-J., et al., *Activation of the central nervous system induced by micro-magnetic stimulation.* Nature Communications, 2013. **4**(1): p. 2463.
91. Park, H.J., et al., *Computational Study on the Thermal Effects of Implantable Magnetic Stimulation Based on Planar Coils.* IEEE Transactions on Biomedical Engineering, 2016. **63**(1): p. 158-167.
92. Bonmassar, G., et al., *Microscopic magnetic stimulation of neural tissue.* Nature Communications, 2012. **3**(1): p. 921.
93. Ridding, M.C. and J.C. Rothwell, *Is there a future for therapeutic use of transcranial magnetic stimulation?* Nature Reviews Neuroscience, 2007. **8**(7): p. 559-567.
94. Rotundo, S., et al., *Shaping and Focusing Magnetic Field in the Human Body: State-of-the Art and Promising Technologies.* Sensors, 2022. **22**(14): p. 5132.
95. Barker, A.T., R. Jalinous, and I.L. Freeston, *Non-invasive magnetic stimulation of human motor cortex.* The Lancet, 1985. **325**(8437): p. 1106-1107.
96. Edwards, M.J., P. Talelli, and J.C. Rothwell, *Clinical applications of transcranial magnetic stimulation in patients with movement disorders.* The Lancet Neurology, 2008. **7**(9): p. 827-840.
97. Rothwell, J.C., *Techniques and mechanisms of action of transcranial stimulation of the human motor cortex.* Journal of Neuroscience Methods, 1997. **74**(2): p. 113-122.
98. Zangen, A., et al., *Transcranial magnetic stimulation of deep brain regions: evidence for efficacy of the H-Coil.* Clinical Neurophysiology, 2005. **116**(4): p. 775-779.
99. Afuwape, O.F., P. Rastogi, and D.C. Jiles, *Comparison of the Effect of Coil Configuration and the Variability of Anatomical Structure on Transcranial*

Magnetic Stimulation. IEEE Transactions on Magnetics, 2021. **57**(2): p. 1-5.
100. Epstein, C.M. and K.R. Davey, *Iron-Core Coils for Transcranial Magnetic Stimulation.* Journal of Clinical Neurophysiology, 2002. **19**(4): p. 376-381.
101. Lang, N., et al., *Stimulus intensity and coil characteristics influence the efficacy of rTMS to suppress cortical excitability.* Clinical Neurophysiology, 2006. **117**(10): p. 2292-2301.
102. Todd, G., S.C. Flavel, and M.C. Ridding, *Low-intensity repetitive transcranial magnetic stimulation decreases motor cortical excitability in humans.* Journal of Applied Physiology, 2006. **101**(2): p. 500-505.
103. Mills, K.R., N.M. Murray, and C.W. Hess, *Magnetic and electrical transcranial brain stimulation: physiological mechanisms and clinical applications.* Neurosurgery, 1987. **20**(1): p. 164-168.
104. Cretaz, E., A.R. Brunoni, and B. Lafer, *Magnetic Seizure Therapy for Unipolar and Bipolar Depression: A Systematic Review.* Neural Plasticity, 2015. **2015**: p. 521398.
105. Deng, Z.-D., S.H. Lisanby, and A.V. Peterchev, *Coil design considerations for deep transcranial magnetic stimulation.* Clinical Neurophysiology, 2014. **125**(6): p. 1202-1212.
106. Jo, H.J., V. Di Lazzaro, and M.A. Perez, *Effect of coil orientation on motor-evoked potentials in humans with tetraplegia.* The Journal of Physiology, 2018. **596**(20): p. 4909-4921.
107. Kaneko, K., et al., *The effect of current direction induced by transcranial magnetic stimulation on the corticospinal excitability in human brain.* Electroencephalography and Clinical Neurophysiology/Electromyography and Motor Control, 1996. **101**(6): p. 478-482.
108. Nakamura, H., et al., *Direct and indirect activation of human corticospinal neurons by transcranial magnetic and electrical stimulation.* Neuroscience Letters, 1996. **210**(1): p. 45-48.
109. Lazzaro, V., et al., *Comparison of descending volleys evoked by monophasic and biphasic magnetic stimulation of the motor cortex in conscious humans.* Experimental Brain Research, 2001. **141**(1): p. 121-127.
110. Amassian, V.E. and M. Stewart, *Chapter 11 Motor cortical and other cortical interneuronal networks that generate very high frequency waves*, in *Supplements to Clinical Neurophysiology*, W. Paulus, et al., Editors. 2003, Elsevier. p. 119-142.
111. Lo, Y.L., et al., *Systematic Correlation of Transcranial Magnetic Stimulation and Magnetic Resonance Imaging in Cervical Spondylotic Myelopathy.* Spine, 2004. **29**(10): p. 1137-1145.
112. Kammer, T., et al., *Motor thresholds in humans: a transcranial magnetic stimulation study comparing different pulse waveforms, current directions and stimulator types.* Clinical Neurophysiology, 2001. **112**(2): p. 250-258.
113. Sommer, M., et al., *Half sine, monophasic and biphasic transcranial magnetic stimulation of the human motor cortex.* Clinical Neurophysiology, 2006. **117**(4): p. 838-844.
114. Sommer, M., et al., *Neuronal tissue polarization induced by repetitive transcranial magnetic stimulation?* NeuroReport, 2002. **13**(6): p. 809-811.
115. Arai, N., et al., *Comparison between short train, monophasic and biphasic repetitive transcranial magnetic stimulation (rTMS) of the human motor cortex.* Clinical Neurophysiology, 2005. **116**(3): p. 605-613.
116. Huang, Y.-Z., et al., *Theta burst stimulation of the human motor cortex.* Neuron, 2005. **45**(2): p. 201-206.
117. Flitman, S.S., et al., *Linguistic processing during repetitive transcranial*

magnetic stimulation. Neurology, 1998. **50**(1): p. 175-181.
118. Pascual-Leone, A., J.R. Gates, and A. Dhuna, *Induction of speech arrest and counting errors with rapid-rate transcranial magnetic stimulation.* Neurology, 1991. **41**(5): p. 697-702.
119. Hu, Y.-T., et al., *Motor cortex repetitive transcranial magnetic stimulation in major depressive disorder - A preliminary randomized controlled clinical trial.* Journal of Affective Disorders, 2024. **344**: p. 169-175.
120. Tang, N., W. Shu, and H.-n. Wang, *Accelerated transcranial magnetic stimulation for major depressive disorder: A quick path to relief?* WIREs Cognitive Science, 2024. **15**(1): p. e1666.
121. Liu, Z., et al., *Efficacy and safety of repeated transcranial magnetic stimulation combined with escitalopram in the treatment of major depressive disorder: a meta-analysis.* Frontiers in Psychiatry, 2024. **14**.
122. Zhang, M., et al., *Efficacy and safety of intermittent theta burst stimulation on adolescents and young adults with major depressive disorder: A randomized, double blinded, controlled trial.* Journal of Affective Disorders, 2024. **350**: p. 214-221.
123. Berlim, M.T., F. Van den Eynde, and Z. Jeff Daskalakis, *Clinically Meaningful Efficacy and Acceptability of Low-Frequency Repetitive Transcranial Magnetic Stimulation (rTMS) for Treating Primary Major Depression: A Meta-Analysis of Randomized, Double-Blind and Sham-Controlled Trials.* Neuropsychopharmacology, 2013. **38**(4): p. 543-551.
124. Berlim, M.T., et al., *Response, remission and drop-out rates following high-frequency repetitive transcranial magnetic stimulation (rTMS) for treating major depression: a systematic review and meta-analysis of randomized, double-blind and sham-controlled trials.* Psychological Medicine, 2014. **44**(2): p. 225-239.
125. Fitzgerald, P.B., et al., *Transcranial Magnetic Stimulation in the Treatment of Depression: A Double-blind, Placebo-Controlled Trial.* Archives of General Psychiatry, 2003. **60**(10): p. 1002-1008.
126. Caumo, W., et al., *Efficacy of Home-Based Transcranial Direct Current Stimulation Over the Primary Motor Cortex and Dorsolateral Prefrontal Cortex in the Disability Due to Pain in Fibromyalgia: A Factorial Sham-Randomized Clinical Study.* The Journal of Pain, 2024. **25**(2): p. 376-392.
127. Fitzgerald, P.B., *The Emerging Use of Brain Stimulation Treatments for Psychiatric Disorders.* Australian & New Zealand Journal of Psychiatry, 2011. **45**(11): p. 923-938.
128. Saccenti, D., et al., *Novel Approaches for the Treatment of Post-Traumatic Stress Disorder: A Systematic Review of Non-Invasive Brain Stimulation Interventions and Insights from Clinical Trials.* Brain Sciences, 2024. **14**(3): p. 210.
129. Yi, S., et al., *Efficacy of repetitive transcranial magnetic stimulation (rTMS) on negative symptoms and cognitive functioning in schizophrenia: An umbrella review of systematic reviews and meta-analyses.* Psychiatry Research, 2024. **333**: p. 115728.
130. Vinod, P., et al., *Comparative efficacy of repetitive transcranial magnetic stimulation protocols for obsessive-compulsive disorder: A network meta-analysis.* Asian Journal of Psychiatry, 2024. **94**: p. 103962.
131. Blyth, S.H., et al., *rTMS for Co-occurring Psychiatric and Substance Use Disorders: Narrative Review and Future Directions.* Current Addiction Reports, 2024.
132. Naik, A., et al., *Optimal Frequency in Repetitive Transcranial Magnetic*

Stimulation for the Management of Chronic Pain: A Network Meta-Analysis of Randomized Controlled Trials. World Neurosurgery, 2024.
133. Gaugain, G., et al., *Quasi-static approximation error of electric field analysis for transcranial current stimulation.* Journal of Neural Engineering, 2023. **20**(1): p. 016027.
134. Spagnolo, F., et al., *Bilateral Repetitive Transcranial Magnetic Stimulation With the H-Coil in Parkinson's Disease: A Randomized, Sham-Controlled Study.* Front Neurol, 2020. **11**: p. 584713.
135. Wilson, M.T., et al., *The challenges of producing effective small coils for transcranial magnetic stimulation of mice.* Biomedical Physics & Engineering Express, 2018. **4**(3): p. 037002.
136. Ziemann, U., *TMS in cognitive neuroscience: virtual lesion and beyond.* Cortex; a journal devoted to the study of the nervous system and behavior, 2010. **46**(1): p. 124-127.
137. Bolognini, N. and T. Ro, *Transcranial Magnetic Stimulation: Disrupting Neural Activity to Alter and Assess Brain Function.* The Journal of Neuroscience, 2010. **30**(29): p. 9647-9650.
138. Au - Sliwinska, M.W., S. Au - Vitello, and J.T. Au - Devlin, *Transcranial Magnetic Stimulation for Investigating Causal Brain-behavioral Relationships and their Time Course.* JoVE, 2014(89): p. e51735.
139. Carpenter, L.L., et al., *TRANSCRANIAL MAGNETIC STIMULATION (TMS) FOR MAJOR DEPRESSION: A MULTISITE, NATURALISTIC, OBSERVATIONAL STUDY OF ACUTE TREATMENT OUTCOMES IN CLINICAL PRACTICE.* Depression and Anxiety, 2012. **29**(7): p. 587-596.
140. McClintock, S.M., et al., *Consensus recommendations for the clinical application of repetitive transcranial magnetic stimulation (rTMS) in the treatment of depression.* The Journal of clinical psychiatry, 2017. **79**(1): p. 3651.
141. Rossi, S., et al., *Safety and recommendations for TMS use in healthy subjects and patient populations, with updates on training, ethical and regulatory issues: Expert Guidelines.* Clinical Neurophysiology, 2021. **132**(1): p. 269-306.
142. Lu, X., et al., *Magnetic nanomaterials-mediated neuromodulation.* WIREs Nanomedicine and Nanobiotechnology, 2023. **15**(4): p. e1890.
143. Kozielski, K.L., et al., *Nonresonant powering of injectable nanoelectrodes enables wireless deep brain stimulation in freely moving mice.* Science Advances, 2021. **7**(3): p. eabc4189.
144. Wang, G., et al., *Revaluation of magnetic properties of Magneto.* Nature Neuroscience, 2020. **23**(9): p. 1047-1050.
145. Huang, H., et al., *Remote control of ion channels and neurons through magnetic-field heating of nanoparticles.* Nature Nanotechnology, 2010. **5**(8): p. 602-606.
146. Roet, M., et al., *Progress in neuromodulation of the brain: A role for magnetic nanoparticles?* Progress in Neurobiology, 2019. **177**: p. 1-14.
147. Christiansen, M.G., A.W. Senko, and P. Anikeeva, *Magnetic Strategies for Nervous System Control.* Annual Review of Neuroscience, 2019. **42**(1): p. 271-293.
148. Yang, X., et al., *Nanotechnology Enables Novel Modalities for Neuromodulation.* Advanced Materials, 2021. **33**(52): p. 2103208.
149. Pan, T., et al., *Fabrication and modeling of silicon-embedded high-Q inductors.* Journal of Micromechanics and Microengineering, 2005. **15**: p. 849-854.

150. Wang, M., et al., *Design and Fabrication of Integrated Power Inductor Based on Silicon Molding Technology.* 2007 IEEE Power Electronics Specialists Conference, 2007: p. 1612-1618.
151. Wang, M., K.D.T. Ngo, and H. Xie, *SU-8 enhanced high power density MEMS inductors.* 2008 34th Annual Conference of IEEE Industrial Electronics, 2008: p. 2672-2676.
152. Klein, M.J.K., et al., *Process for the fabrication of hollow core solenoidal microcoils in borosilicate glass.* Journal of Micromechanics and Microengineering, 2008. **18**(7): p. 075002.
153. Zhuo, C. and C. Baixin. *TSV inductor optimization and its design implication*. in *2017 China Semiconductor Technology International Conference (CSTIC)*. 2017.
154. Siegel, A.C., et al., *Microsolidics: Fabrication of Three-Dimensional Metallic Microstructures in Poly(dimethylsiloxane).* Advanced Materials, 2007. **19**(5): p. 727-733.
155. Fang, D.-M., et al., *Surface micromachined three-dimentional solenoid-type inductor*, in *4M 2006 - Second International Conference on Multi-Material Micro Manufacture*, W. Menz, S. Dimov, and B. Fillon, Editors. 2006, Elsevier: Oxford. p. 103-106.
156. Jun-Bo, Y., et al., *CMOS-compatible surface-micromachined suspended-spiral inductors for multi-GHz silicon RF ICs.* IEEE Electron Device Letters, 2002. **23**(10): p. 591-593.
157. Yong-Jun, K. and M.G. Allen, *Surface micromachined solenoid inductors for high frequency applications.* IEEE Transactions on Components, Packaging, and Manufacturing Technology: Part C, 1998. **21**(1): p. 26-33.
158. Matsumoto, Y., et al., *Cylindrical coils created with 3D X-ray lithography and metallization.* Microsystem Technologies, 2008. **14**(9): p. 1373-1379.
159. Stanley, S.A., et al., *Radio-Wave Heating of Iron Oxide Nanoparticles Can Regulate Plasma Glucose in Mice.* Science, 2012. **336**(6081): p. 604-608.
160. Nair, M., et al., *Externally controlled on-demand release of anti-HIV drug using magneto-electric nanoparticles as carriers.* Nature Communications, 2013. **4**(1): p. 1707.
161. Guduru, R., et al., *Magnetoelectric 'spin' on stimulating the brain.* Nanomedicine, 2015. **10**(13): p. 2051-2061.
162. Ma, J., et al., *Model electrical activity of neuron under electric field.* Nonlinear Dynamics, 2019. **95**(2): p. 1585-1598.
163. Moya Gómez, A., et al., *Electromagnetic Field as a Treatment for Cerebral Ischemic Stroke.* Frontiers in Molecular Biosciences, 2021. **8**.
164. Sangster, A.J., *Fundamentals of Electromagnetic Radiation*, in *Compact Slot Array Antennas for Wireless Communications*, A.J. Sangster, Editor. 2019, Springer International Publishing: Cham. p. 35-56.
165. Fukao, S. and K. Hamazu, *Electromagnetic Waves*, in *Radar for Meteorological and Atmospheric Observations*, S. Fukao and K. Hamazu, Editors. 2014, Springer Japan: Tokyo. p. 7-31.
166. Eom, H.J., *Maxwell's Equations*, in *Primary Theory of Electromagnetics*, H.J. Eom, Editor. 2013, Springer Netherlands: Dordrecht. p. 113-128.
167. Plonsey, R. and D.B. Heppner, *Considerations of quasi-stationarity in electrophysiological systems.* The bulletin of mathematical biophysics, 1967. **29**(4): p. 657-664.
168. Efthimiadis, K.G., T. Samaras, and K.S. Polyzoidis, *Magnetic stimulation of the spine: the role of tissues and their modelling.* Physics in Medicine & Biology, 2010. **55**(9): p. 2541.

169. Nieminen, J.O., L.M. Koponen, and R.J. Ilmoniemi, *Experimental Characterization of the Electric Field Distribution Induced by TMS Devices.* Brain Stimulation, 2015. **8**(3): p. 582-589.
170. Ida, N., *The Static Magnetic Field*, in *Engineering Electromagnetics*, N. Ida, Editor. 2015, Springer International Publishing: Cham. p. 383-426.
171. Balsara, D.S. and D.S. Spicer, *A Staggered Mesh Algorithm Using High Order Godunov Fluxes to Ensure Solenoidal Magnetic Fields in Magnetohydrodynamic Simulations.* Journal of Computational Physics, 1999. **149**(2): p. 270-292.
172. Barbieri, S., M. Cavinato, and M. Giliberti, *An educational path for the magnetic vector potential and its physical implications.* European Journal of Physics, 2013. **34**(5): p. 1209.
173. Jackson, J.D., *From Lorenz to Coulomb and other explicit gauge transformations.* American Journal of Physics, 2002. **70**(9): p. 917-928.
174. Whites, K.W., *1 - Magnetostatics*, in *The Electrical Engineering Handbook*, W.-K. Chen, Editor. 2005, Academic Press: Burlington. p. 479-497.
175. Maugin, G.A., *The thermomechanics of nonlinear irreversible behaviours*. Vol. 27. 1999: World scientific.
176. Tenorio, G., B. Herkenhoff, and M. Hassanalian, *Penguin Huddling and Bioinspired Martian Habitats: Analytical and Experimental Studies*, in *AIAA AVIATION 2021 FORUM*.
177. !!! INVALID CITATION !!! [182].
178. !!! INVALID CITATION !!! [183-186].
179. Basham, E., et al., *Magnetic Stimulation of Neural Tissue: Techniques and System Design*, in *Implantable Neural Prostheses 1: Devices and Applications*, E. Greenbaum and D. Zhou, Editors. 2009, Springer US: New York, NY. p. 293-351.
180. Braun, P., et al., *Coil Efficiency for Inductive Peripheral Nerve Stimulation.* IEEE Transactions on Neural Systems and Rehabilitation Engineering, 2022. **30**: p. 2137-2145.
181. Das, R., F. Moradi, and H. Heidari, *Biointegrated and Wirelessly Powered Implantable Brain Devices: A Review.* IEEE Trans Biomed Circuits Syst, 2020. **14**(2): p. 343-358.
182. Dayan, E., et al., *Noninvasive brain stimulation: from physiology to network dynamics and back.* Nature Neuroscience, 2013. **16**(7): p. 838-844.
183. Deer, T.R., et al., *The Appropriate Use of Neurostimulation: Avoidance and Treatment of Complications of Neurostimulation Therapies for the Treatment of Chronic Pain.* Neuromodulation: Technology at the Neural Interface, 2014. **17**(6): p. 571-598.
184. Rossi, S., et al., *Safety, ethical considerations, and application guidelines for the use of transcranial magnetic stimulation in clinical practice and research.* Clin Neurophysiol, 2009. **120**(12): p. 2008-2039.
185. Korcak, L.L. and D.F. Kavanagh. *Thermal Accelerated Aging Methods for Magnet Wire: A Review*. in *2018 International Conference on Diagnostics in Electrical Engineering (Diagnostika)*. 2018.
186. Klein, M.M., et al., *Transcranial magnetic stimulation of the brain: guidelines for pain treatment research.* Pain, 2015. **156**(9): p. 1601-1614.
187. !!! INVALID CITATION !!! [187, 190].
188. Zohdi, T.I., *Simulation of coupled microscale multiphysical-fields in particulate-doped dielectrics with staggered adaptive FDTD.* Computer Methods in Applied Mechanics and Engineering, 2010. **199**(49): p. 3250-3269.

189. Tsai, Y.-Y., *TMS coil design.* Bachelor thesis. Worchester Polytechnic Institute, 2011.
190. !!! INVALID CITATION !!! [87, 91, 100, 135].
191. Feriani, A., F. Perotti, and V. Simoncini, *Iterative system solvers for the frequency analysis of linear mechanical systems.* Computer Methods in Applied Mechanics and Engineering, 2000. **190**(13): p. 1719-1739.
192. Johnson, S.G. and J.D. Joannopoulos, *Block-iterative frequency-domain methods for Maxwell's equations in a planewave basis.* Optics Express, 2001. **8**(3): p. 173-190.
193. Pflaum, C. and Z. Rahimi, *An iterative solver for the finite-difference frequency-domain (FDFD) method for the simulation of materials with negative permittivity.* Numerical Linear Algebra with Applications, 2011. **18**(4): p. 653-670.
194. Notaros, B.M., *Higher Order Frequency-Domain Computational Electromagnetics.* IEEE Transactions on Antennas and Propagation, 2008. **56**(8): p. 2251-2276.
195. Mochrie, S. and C. De Grandi, *Magnetic Fields and Ampere's Law*, in *Introductory Physics for the Life Sciences*. 2023, Springer International Publishing: Cham. p. 763-791.
196. Walton, F., et al., *Cleanroom strategies for micro- and nano-fabricating flexible implantable neural electronics.* Philosophical Transactions of the Royal Society A: Mathematical, Physical and Engineering Sciences, 2022. **380**(2228): p. 20210009.
197. Xu, T., et al., *3D MEMS In-Chip Solenoid Inductor With High Inductance Density for Power MEMS Device.* IEEE Electron Device Letters, 2019. **40**(11): p. 1816-1819.
198. Liu, X., et al., *MEMS micro-coils for magnetic neurostimulation.* Biosensors and Bioelectronics, 2023. **227**: p. 115143.
199. Nelson, B.J. and L. Dong, *Nanorobotics*, in *Springer Handbook of Nanotechnology*, B. Bhushan, Editor. 2010, Springer Berlin Heidelberg: Berlin, Heidelberg. p. 1633-1659.
200. Rogers, J.A., et al., *Using microcontact printing to fabricate microcoils on capillaries for high resolution proton nuclear magnetic resonance on nanoliter volumes.* Applied physics letters, 1997. **70**(18): p. 2464-2466.
201. Sarreal, R.R. and P. Bhatti, *Characterization and Miniaturization of Silver-Nanoparticle Microcoil via Aerosol Jet Printing Techniques for Micromagnetic Cochlear Stimulation.* Sensors, 2020. **20**(21): p. 6087.
202. Ohring, M., *Chapter 3 - Thin-Film Evaporation Processes*, in *Materials Science of Thin Films (Second Edition)*, M. Ohring, Editor. 2002, Academic Press: San Diego. p. 95-144.
203. Kerdcharoen, T. and C. Wongchoosuk, *11 - Carbon nanotube and metal oxide hybrid materials for gas sensing*, in *Semiconductor Gas Sensors*, R. Jaaniso and O.K. Tan, Editors. 2013, Woodhead Publishing. p. 386-407.
204. Kubono, A., Y. Minagawa, and T. Ito, *In situ study on layer-by-layer growth in vapor deposition of linear long-chain molecules using a quartz crystal microbalance.* Journal of Applied Physics, 2013. **114**(18).
205. Satpathy, B., et al., *A comprehensive review of various non-cyanide electroplating baths for the production of silver and gold coatings.* International Materials Reviews, 2023. **68**(7): p. 825-861.
206. Choudhury, D., J.R. Macdonald, and A.K. Kar, *Ultrafast laser inscription: perspectives on future integrated applications.* Laser & Photonics Reviews, 2014. **8**(6): p. 827-846.

207. McMahon, P., et al., *Aspects of laser micromachining for sensor prototyping*. SPIE Smart Materials, Nano- and Micro-Smart Systems. Vol. 6415. 2006: SPIE.
208. Wurz, M.C., et al., *Fabrication of a Micro Coil for Magnetooptical Data Storage.* IEEE Transactions on Magnetics, 2006. **42**(10): p. 2468-2470.
209. Jolic, K.I., et al., *Fabrication of three-dimensional inductor coil using excimer laser micromachining.* Journal of Micromechanics and Microengineering, 2003. **13**(5): p. 782.
210. Mishra, S. and V. Yadava, *Laser Beam MicroMachining (LBMM) – A review.* Optics and Lasers in Engineering, 2015. **73**: p. 89-122.
211. Atsushiba, H., et al., *Adhesion and Interfacial Structure of Metal Film Electrolessly Deposited on Si Using Au Nanoparticles As Catalysts.* ECS Meeting Abstracts, 2014. **MA2014-01**(9): p. 524.
212. Yamada, N., et al., *Effect of Epitaxial Growth of Gold Nanoparticles on Silicon Substrates on Adhesion of Electrolessly Deposited Metal Films.* ECS Meeting Abstracts, 2015. **MA2015-02**(47): p. 1900.
213. Fujita, T., et al., *Seedlayer-less gold electroplating on silicon surface for MEMS applications.* Sensors and Actuators A: Physical, 2007. **135**(1): p. 50-57.
214. Cao, Q., et al., *The importance of coil conductivity and eddy current effects in the analysis of electromagnetic forming process.* High Voltage, 2022. **7**(2): p. 390-404.
215. Stuchly, M.A. and K.P. Esselle, *Factors affecting neural stimulation with magnetic fields.* Bioelectromagnetics, 1992. **13**(S1): p. 191-204.
216. Matula, R.A., *Electrical resistivity of copper, gold, palladium, and silver.* Journal of Physical and Chemical Reference Data, 1979. **8**(4): p. 1147-1298.
217. Traficante, D.D., *Impedance: What it is, and why it must be matched.* Concepts in Magnetic Resonance, 1989. **1**(2): p. 73-92.
218. Yang, Z., W. Liu, and E. Basham, *Inductor Modeling in Wireless Links for Implantable Electronics.* IEEE Transactions on Magnetics, 2007. **43**(10): p. 3851-3860.
219. Rutkove, S.B., *Electrical impedance myography: Background, current state, and future directions.* Muscle & Nerve, 2009. **40**(6): p. 936-946.
220. Rawlins, J.C., *CHAPTER 9 - RL Circuit Analysis*, in *Basic AC Circuits (Second Edition)*, J.C. Rawlins, Editor. 2000, Newnes: Burlington. p. 303-334.
221. Koltunowicz, T.N., *Inductive type properties of FeCoZr–CaF2 and FeCoZr–PZT nanocomposites.* Journal of Materials Science: Materials in Electronics, 2015. **26**(9): p. 6450-6457.
222. Ju, L., et al., *Weak epsilon-negative silver nanowires/polyimide metacomposites with extremely low losses.* Composites Part A: Applied Science and Manufacturing, 2022. **153**: p. 106755.
223. Kumar, A. and P.A. Bottomley, *Optimized quadrature surface coil designs.* Magnetic Resonance Materials in Physics, Biology and Medicine, 2007. **21**(1): p. 41.
224. Siebert, R., J. Schneider, and E. Beyer, *Laser Cutting and Mechanical Cutting of Electrical Steels and its Effect on the Magnetic Properties.* IEEE Transactions on Magnetics, 2014. **50**(4): p. 1-4.
225. Xi, N. and C.R. Sullivan. *An improved calculation of proximity-effect loss in high-frequency windings of round conductors*. in *IEEE 34th Annual Conference on Power Electronics Specialist, 2003. PESC '03.* 2003.
226. Wheeler, H.A., *Formulas for the Skin Effect.* Proceedings of the IRE, 1942.

30(9): p. 412-424.
227. Kennelly, A.E. and H.A. Affel, *Skin-Effect Resistance Measurements of Conductors, at Radio-Frequencies up to 100,000 Cycles per Second.* Proceedings of the Institute of Radio Engineers, 1916. **4**(6): p. 523-574.
228. Cockcroft, J.D. and E. Rutherford, *Skin effect in rectangular conductors at high frequencies.* Proceedings of the Royal Society of London. Series A, Containing Papers of a Mathematical and Physical Character, 1929. **122**(790): p. 533-542.
229. Teixeira, F.L., et al., *Finite-difference time-domain methods.* Nature Reviews Methods Primers, 2023. **3**(1): p. 75.
230. Warren, C., et al., *Comparison of time-domain finite-difference, finite-integration, and integral-equation methods for dipole radiation in half-space environments.* Progress In Electromagnetics Research M, 2017. **57**: p. 175-183.
231. Rabina, J., S. Monkola, and T. Rossi, *Efficient time integration of Maxwell's equations with generalized finite differences.* SIAM Journal on Scientific Computing, 2015. **37**(6): p. B834-B854.
232. Park, H.-J., et al., *Planar coil-based contact-mode magnetic stimulation: synaptic responses in hippocampal slices and thermal considerations.* Scientific Reports, 2018. **8**(1): p. 13423.
233. Stosiek, C., et al., *In vivo two-photon calcium imaging of neuronal networks.* Proceedings of the National Academy of Sciences, 2003. **100**(12): p. 7319-7324.
234. Rais, M., et al., *Functional consequences of postnatal interventions in a mouse model of Fragile X syndrome.* Neurobiology of Disease, 2022. **162**: p. 105577.
235. Chadwick, W., et al., *A novel combination treatment for fragile X syndrome predicted using computational methods.* Brain Communications, 2024. **6**(1).
236. Ye, H., et al., *Cellular mechanisms underlying carry-over effects after magnetic stimulation.* Scientific Reports, 2024. **14**(1): p. 5167.